Faculty of Physics and Astronomy

University of Heidelberg

Diploma thesis
in Physics

submitted by
Joachim Hahn
born in Heidelberg, Germany

Heidelberg
February 2010

Modelling the Inverse Compton Emission from Pulsar Wind Nebulae

This diploma thesis has been carried out by
Joachim Hahn
at the Max-Planck Institut für Kernphysik

under the supervision of
Prof. Werner Hofmann

Abstract

In recent years, Cherenkov telescopes like H.E.S.S. have identified Pulsar Wind Nebulae (PWNe) at energies between 100 GeV and 100 TeV as one of the main source populations emitting gamma-rays at these energies. PWNe consist of electrons and positrons emitted by pulsars which radiatively cool down by undergoing synchrotron radiation and inverse Compton scattering. In the case of inverse Compton scattering, the resulting photons show energies up to hundreds of TeV and are therefore making PWNe visible in the mentioned energy range.
The first part of this work is dedicated to a model describing the spectral and spatial distribution of the gamma-ray emission from PWNe. Its application to the PWN created by the Geminga pulsar shows an agreement with measured flux values obtained by the Milagro and EGRET experiments. The modelled spatial extension coincides with Milagro observations. The aim of the second part is to verify previously derived analytical results concerning the spectral evolution of electrons due to inverse Compton scattering with a Monte-Carlo simulation using the exact Klein-Nishina cross section. Analytically expected spectral shapes have been qualitatively reproduced for both a burst-like and a stationary injection scenario assuming mono-energetic or blackbody distributed target photons.

Kurzfassung

In den letzten Jahren haben Tscherenkow-Teleskope, wie zum Beispiel H.E.S.S., Pulsar Wind Nebel (PWN) in einem spektralen Bereich zwischen 100 GeV und 100 TeV als eine der Hauptpopulationen an Gammastrahlungsquellen identifiziert. PWN setzen sich aus von Pulsaren ausgestoßenen Elektronen und Positronen zusammen, die durch Strahlungsprozesse wie Synchrotronstrahlung und inverse Comptonstreuung abkühlen. Die dabei frei werdenden Photonen weisen im Fall von inverser Comptonstreuung Energien von bis zu mehreren hundert TeV auf und machen so PWN im genannten Energiebereich sichtbar.
Der erste Teil dieser Arbeit widmet sich einem Modell zur Beschreibung der räumlichen und spektralen Verteilung der Gammastrahlungsemission von PWN. Seine Anwendung auf den vom Geminga-Pulsar erzeugten PWN zeigt eine Übereinstimmung mit von den EGRET- und Milagro- Experimenten gemessenen Flußwerten. Die modellierte Ausdehnung deckt sich mit von Milagro angestellten Beobachtungen. Das Ziel des zweiten Teils ist es, bereits vorhandene analytische Ergebnisse für die spektrale Entwicklung von Elektronen durch inverse Comptonstreuung mit einer Monte-Carlo-Simulation zu verifizieren, welche den exakten Klein-Nishina Wirkungsquerschnitt benutzt. Analytisch erwartete Formen der Spektren wurden unter der Annahme einer explosionsartigen und einer stationären Elektroneninjektion qualitativ reproduziert, sowohl für monoenergetische als auch schwarzkörperverteilte Ziel-Photonen.

Contents

Preface

For centuries, humans have been puzzled by the impressive sight of the night sky, trying to unveil its mysteries by observing it with the bare eye. They could not know that behind the obvious - the sky as it is seen in the optical light - the universe appears in another light.
Over the past hundred years, new types of telescopes widened the observable spectral range, down to energies that correspond to radio emission and up the X-ray energy band and even higher.
But despite the many technological advances and amazing discoveries achieved since the first days of astronomy many questions remain open, such as: what is the origin of cosmic rays? How are they accelerated? Where do highly energetic gamma-rays come from?
In order to investigate these interesting questions, a new type of telescope - the Cerenkov telescope - was invented in the late 20th century. Observing the Cerenkov emission caused by cosmic rays impinging on earth's atmosphere allows scientists to look at the universe in a very high energetic gamma-ray light in search of cosmic accelerators.
During the last decade, new Cerenkov telescopes like H.E.S.S. (the High Energy Stereoscopic System) have greatly extended the number of known very-high-energy gamma-ray sources.
Many of them turn out to be Pulsar wind nebulae (PWNe).
These objects show a rich diversity of spectral and spatial morphologies in their gamma-ray emission and it is desirable to develop models that could help to understand the nature of pulsar wind nebulae and their variety in appearance.

In this work, a simple model is presented with which the spectral and spatial properties of the gamma-ray emission from single PWNe may be described. It is a diffusion model and neglects other transport mechanisms.
The cooling of the cosmic ray electrons is assumed to be of radiative nature, namely inverse compton and synchrotron radiation originating in the interaction of the electrons with ambient photon fields and the interstellar magnetic field, respectively.
The model developed in this work will be applied to the nearby PWN created by the Geminga pulsar.

Furthermore, the dominating radiation process conducted by electrons causing the VHE gamma-ray emission from PWN, the inverse Compton scattering, has been investigated with a Monte-Carlo simulation. This simulation and its

results are presented in this work.
The aim is to confirm analytical considerations for that process at electron energies extending up to hundreds of TeV where inverse Compton scattering occurs in the Klein-Nishina regime. In this regime, the scattering is a discrete rather than a continuous process, complicating its analytical treatment.

This work is structured in the following way:

- Chapter one gives a physical overview over pulsars and PWNe. Additionally, the for this work most relevant radiation processes in which cosmic ray electrons are involved are discussed.
- The second chapter presents the model describing the very high energetic gamma-ray emission from PWNe.
- Chapter three is dedicated to the Monte-Carlo simulation of the inverse Compton scattering process.
- Finally, chapter four gives a conclusion and an outlook.

1 Theoretical Basics

Pulsars and PWNe as well as the most relevant radiation processes of electrons with energies between 10 GeV and 100 TeV will be the topic of this chapter.

It is structured as follows:

- Section 1.1 will present pulsars and pulsar wind nebulae.
- The dominant radiation mechanisms electrons at these energies are involved in while traversing space will be discussed in section 1.2.

1.1 Pulsars And Their Nebulae

Pulsars

Pulsars are rapidly rotating, magnetized neutron stars. It is well understood that pulsars are possible remains of supernova explosions. From the conservation of the magnetic flux before and after the supernova, enormous magnetic field strengths between 10^9 G and 10^{13} G are to be expected at the pulsar's surface. Since pulsars show rotational periods between $\sim$ 1 ms and $\sim$ 10 s, it follows that extreme electrical fields are induced at the pulsar's surface, pulling at charges in the pulsar's surface material with forces that are greatly exceeding the pulsar's attractive forces on these charges. As a result, the pulsar's surroundings are filled with charged particles constituting a plasma in which electric charges can flow. This environment is called the pulsar's magnetosphere, since its physics is mainly determined by the magnetic field.
Figure 1.1 gives an overview of the situation.

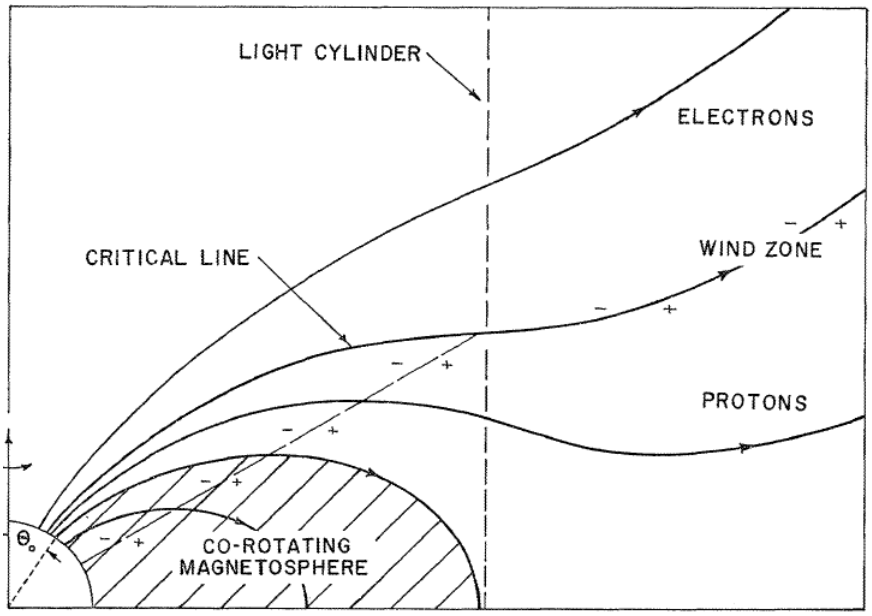

Figure 1.1: Sketch of the pulsars co-rotating magnetosphere. (Taken from Goldreich and Julian [14])

Except for few locations in the the magnetosphere, which will be discussed in the next paragraph, the electric field is perpendicular to the magnetic field ($\mathbf{E} \cdot \mathbf{B} = 0$) due to screening from space charges, compensating the electric field component tangential to the magnetic field direction. Thus, the magnetic field lines are equipotentials in these regions, and one can imagine the charges to

slide along them. The magnetic field co-rotates with the pulsar, and because the charges are attached to the magnetic field lines, they also co-rotate. This leads to a limiting condition of the spatial extension of the pulsar's magnetosphere: At a certain distance to the pulsar, the co-rotating charges would reach the speed of light. This is the maximal distance co-rotating charges may have to the pulsar, and the corresponding surface of revolution is called the *light cylinder*. It is located at a distance $r_L = c/\Omega$, where c is the speed of light and Ω is the angular velocity of the pulsar. For a pulsar with a rotational period of 10 ms, the radius of its light cylinder would be $r_L \sim 500$ km.
It is believed that there are regions in the pulsar magnetosphere, where $\mathbf{E} \cdot \mathbf{B} \neq 0$ and thus $E_\parallel \neq 0$. As a result, charges are accelerated while moving along the field lines. These charges emit gamma radiation by inverse Compton (IC), synchrotron and curvature radiation, which either leaves the pulsar's magnetosphere and can be observed as pulsed gamma-ray emission with energies up to $\lesssim 25$ GeV or gets absorbed by the strong magnetic field undergoing e^+/e^- pair production. The secondary electrons produced in that way get accelerated themselves and repeat that procedure. Thus, a pair cascade is formed at these locations in the pulsar's magnetosphere. It is under debate where those regions are located. They are suspected to be either at the pulsar's polar caps or near the light cylinder, both leading to different theories. Recent Fermi measurements seem to indicate that the emission region is located several pulsar radii away from the pulsar surface (see Abdo et al. [2]).

The relativistic electron cascade eventually leaves the magnetosphere by streaming along open magnetic field lines, i.e. field lines that cross the light cylinder, creating a relativistic wind outside the pulsar's magnetosphere.

Pulsar Wind Nebulae

After the supernova explosion, the pulsar is surrounded by slow moving, unshocked supernova ejecta. Relativistic electrons that are produced in the pulsar's magnetosphere stream into the surrounding medium, forming a *pulsar wind nebula* (PWN). The relativistic electrons constituting the PWN are highly over-pressured with respect to the surrounding ejecta and as a result, a shock is formed. This shock is called the PWN forward shock. The PWN's expansion at that evolutionary stage is given by [7]

$$\begin{aligned} R_{PWN} &\approx 1.5 \dot{E}_0^{1/5} E_{SN}^{3/10} M_{ej}^{-1/2} t^{6/5} \\ &= 1.1\text{pc} \left(\frac{\dot{E}_0}{10^{38}\text{erg s}^{-1}} \right)^{1/5} \left(\frac{E_{SN}}{10^{51}\text{erg}} \right)^{3/10} \left(\frac{M_{ej}}{M_\odot} \right)^{-1/2} \left(\frac{t}{10^3\text{a}} \right)^{6/5}, \end{aligned}$$

where $\dot{E}_0$ is the initial spin down power of the pulsar, E_{SN} is the energy output of the supernova, M_{ej} is the mass of the supernova ejecta and t is the passed

time. As one can see, the expansion velocity increases with time $\dot{R}_{PWN} \propto t^{1/5}$.

At the same time, the supernova remnant (SNR) expands supersonically into the ISM, causing a SNR forward shock that sweeps up interstellar medium in its wake. If the pressure of this shocked material eventually exceeds the thermal pressure of the SNR forward shock, the ambient material is getting compressed and heated and pushes back on the shock. As a result, a reverse shock behind the SNR forward shock is formed, separated from the latter by a contact discontinuity. In time, the reverse shock moves inwards and heats the cool supernova ejecta.

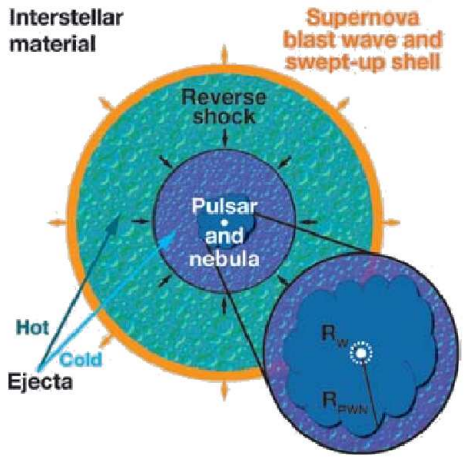

Figure 1.2: Sketch of a PWN within a SNR (taken from Gaensler and Slane [11]).

Typically a few thousand years after the supernova explosion, the reverse shock collides with the PWN forward shock compressing and heating up the PWN, prompting it to expand in return. This interaction leads to an oscillatory behaviour of the PWN on a time scale of several thousand years. Due to these oscillations, material is mixed up within the PWN and instabilities cause the creation of filamentary structures resulting in a complex interior of the PWN.
After several oscillations, the reverberations fade and the PWN once more expands, but the reverse shock has previously heated up the material surrounding the PWN in an extent that the electron outflow is no longer supersonic. Thus, no shock is driven to the ejecta (see Gaensler [11]).
The pulsar wind inflates a bubble that is confined by the interstellar matter swept up by the SN forward shock. This confinement imposes the PWN expansion speed at its boundary to match the speed of the slower moving SNR.
For $\dot{R}_{PWN}$, the speed at which the PWN expands, usually holds $\dot{R}_{PWN} \ll c$,

where c is the speed of light. Relativistic particles with velocities $v \sim c$ are continuously injected into the PWN by the pulsar, building up pressure at the nebula since it expands too slowly. At a characteristic radius R_s away from the pulsar, this ram pressure caused by the relativistic wind streaming out of the pulsar's magnetosphere equals the magnetic and particle pressure inside the PWN and a shock transition at R_s is built up. This shock is called *termination shock*.
The situation is outlined in figure 1.3

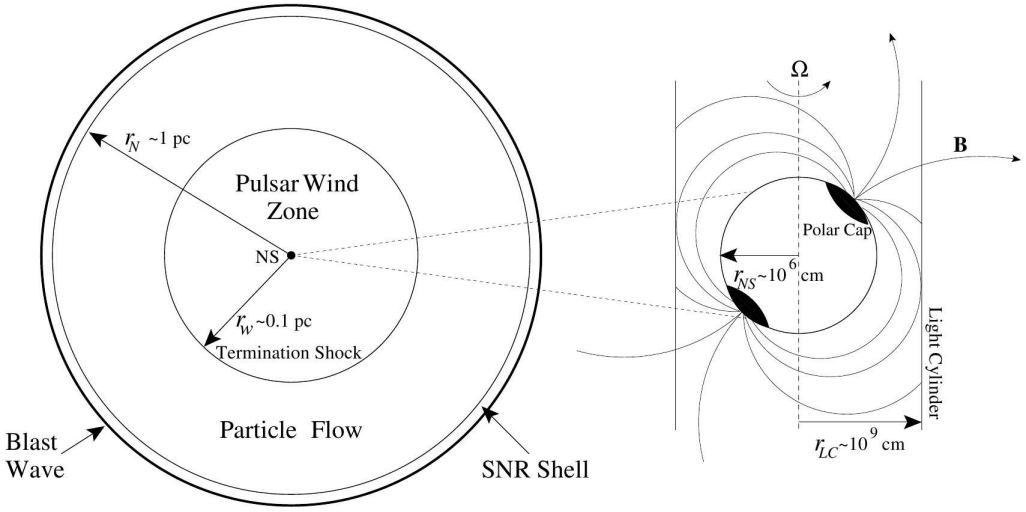

Figure 1.3: Sketch of a composite SNR featuring the termination shock (taken from Slane [22]).

The distance to the center, where the termination shock is formed is given by

$$R_s = \sqrt{\dot{E}/(4\pi\omega c P_{PWN})} \sim 0.1\text{pc}, \tag{1.1}$$

where $\dot{E}$ is the pulsar's spin-down luminosity, ω is the equivalent filling factor of an isotropic wind and P_{PWN} is the pressure in the shocked PWN.
At the termination shock, electrons get accelerated and reach Lorentz factors of $\gamma > 10^5$. This is the origin of the highly relativistic electrons investigated in the PWN-model devised in this work.

The described pulsar-PWN complex is able to produce very high energy (VHE, energy within an interval [10 GeV, 100 TeV]) gamma radiation by different mechanisms originating at different locations of the object, see figure 1.4.
Firstly, as discussed earlier, electrons located within the pulsar's light cylinder

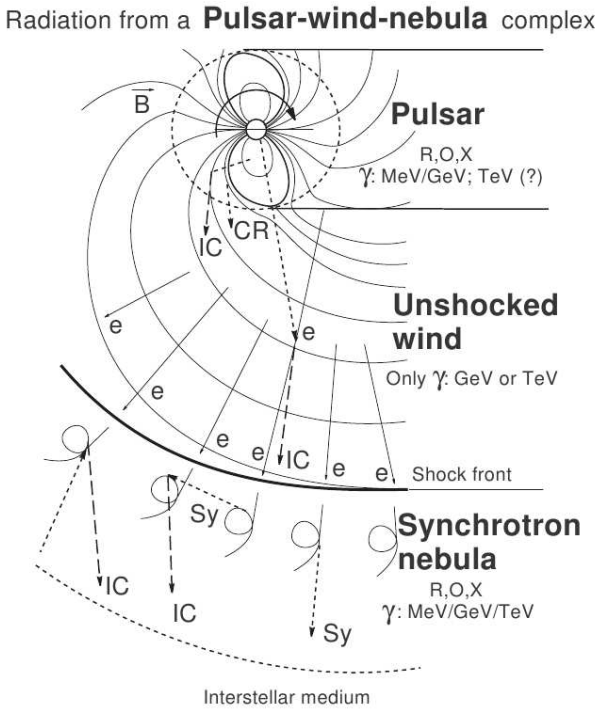

Figure 1.4: Gamma ray emission and radiation mechanisms of electrons from the different regions of a PWN. R, O and X denote for emission in the radio, optical or X-ray range (taken from Aharonian and Bogovalov [4]).

emit gamma-rays due to inverse Compton, synchrotron and curvature radiation, which will be discussed in the next section. However, VHE gamma radiation from this location experiences a spectral exponential cut-off with typical cut-off energies $\sim$1-3 GeV since higher energy photons are absorbed by the pulsar's enormous magnetic fields.
The region between the pulsar's light cylinder and the termination shock is filled with relativistic, unshocked electron outflow from the pulsar. Since the curvature of the pulsar's magnetic field in this region lines decreases, the curvature radiation intensity drops. Furthermore, the magnetic field is frozen into the relativistic plasma of ejected electrons, so that that they move together with the magnetic field, resulting in a decrease in synchrotron radiation. Inverse Compton radiation, however, occurs with the radiation fields present in that region. Still, because of the low intensity of synchrotron and curvature radiation, this region shows a decreased luminosity in VHE gamma light.
Beyond the termination shock highly accelerated electrons emit synchrotron and inverse Compton radiation. This region contributes the largest part to the VHE gamma emission from PWNe.

1.2 Pulsar Wind Nebula Electrons: Radiation Processes

Highly relativistic electrons traversing the interstellar medium (ISM) undergo various radiation processes during their lifetime, emitting photons covering a wide spectral range. The ISM is believed to be a dilute, partially ionized gas embedded in a magnetic field and a radiation field. Depending on the ISM's component the electrons react with, one distinguishes the following radiation processes:

- bremsstrahlung: the electron is accelerated in the electrostatic field of ions and the nuclei of atoms populating the ISM
- synchrotron radiation: the electron emits a photon while being deflected in its trajectory by cosmic magnetic fields
- inverse Compton scattering: the electron scatters with a photon from the ambient radiation field increasing this photon's energy

Even though these processes seem to differ profoundly from each other, they are in fact special cases of one superordinate process, namely inverse Compton scattering:

- Bremsstrahlung corresponds to inverse Compton scattering with the virtual photons of the Coulomb field of the ion and nucleus
- Synchrotron radiation can be regarded as inverse Compton scattering with the virtual photons of the local magnetic field.

Thus, all three processes can be formally treated in a uniform way. In the following, this treatment will be roughly outlined.
Additional to the radiation mechanisms mentioned above, electrons undergo other radiative processes, such as ionizing the atoms of the ISM. However, in general only the mentioned processes play a major role at the high electron energies $E>10$ GeV that are assumed in this work.

1.2.1 Inverse Compton Scattering

Inverse Compton scattering occurs when a high energy electron traverses a photon field. Energy is transferred from the electron to the photon, which will be called *target photon* throughout this work.
In the following, the derivation of the total energy loss rate of electrons and the emitted photon spectrum per electron due to inverse Compton scattering will be roughly derived, based on the work of Blumenthal and Gould [6], since these quantities are of central importance to this work.

Figure 1.5 shows the electron-photon collision in two different frames: The lab frame K and the electron's rest frame K'.

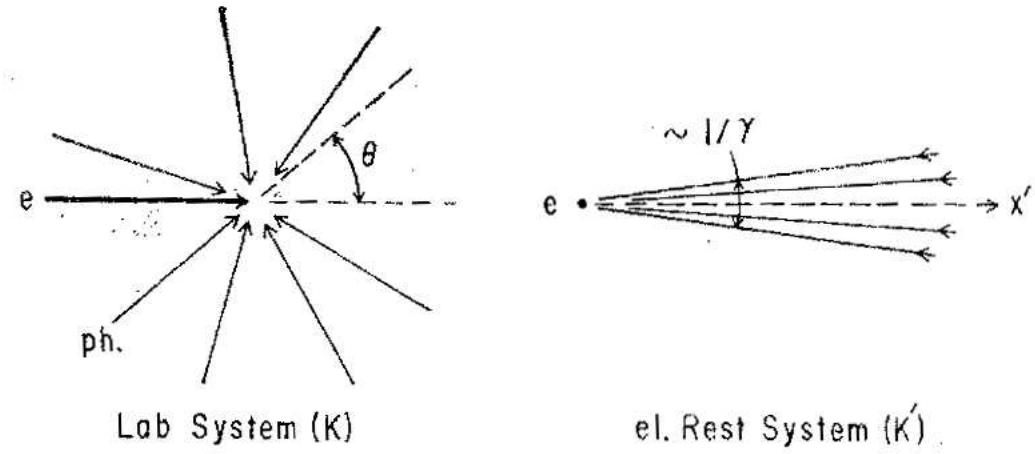

Figure 1.5: Inverse Compton scattering in the lab frame and the electron's rest frame (adapted from Blumenthal and Gould [6]).

In the lab frame K the highly relativistic electron possesses an energy of $E = \gamma mc^2$, where γ is the electron's Lorentz factor, m the electron's rest mass and c the speed of light. In its rest frame the electron's energy is $E' = mc^2$. The photon energy before scattering is denoted by ϵ in K and ϵ' in K'. Analogously, the photon energy after scattering is called ϵ_1 in K and ϵ_1' in K'. The angle between the initial photon's direction and the x axis (compare to Figure 1.5) is θ in K respectively θ' in K'. After the scattering the photon moves, with respect to the x axis, at an angle of θ_1 in K and θ_1' in K'.

Let v be the electron's velocity. Then the relations between the photons in the different rest frames are given by the Doppler shift formulas (see, for instance [15]),

$$\begin{aligned} \epsilon' &= \epsilon\gamma(1-\beta\cos\theta), & (1.2)\\ \epsilon_1 &= \epsilon_1'\gamma[1+\beta\cos(\pi-\theta_1')] \\ &\approx \epsilon_1'\gamma(1-\cos\theta_1'), & (1.3) \end{aligned}$$

with the ratio $\beta = v/c \to 1$ in the highly relativistic limit.
In the electron's rest frame the initial electron energy ϵ and the electron energy after scattering ϵ_1' are related in the following way [6]:

$$\epsilon_1' = \frac{\epsilon'}{1+(\epsilon'/mc^2)(1-\cos\theta_1')}. \quad (1.4)$$

One can investigate two extreme cases:

- $\epsilon' \ll mc^2$, i.e. in the electron's rest frame, the target photon's energy is much smaller than the electron's rest energy. This is the *Thomson limit*.
- $\epsilon' \gg mc^2$, i.e. in the electron's rest frame, the target photon's energy is much larger than the electron's rest energy. This is the *Klein-Nishina limit*.

Following Rybicki and Lightman [21], the angles θ and θ_1' are characteristically of order $\pi/2$.

IC-Scattering In The Thomson Limit: Photon Energy After Scattering

Firstly the typical photon energies after inverse Compton scattering will be discussed.
In the Thomson limit relation $\epsilon' \ll mc^2$ holds. Introducing this assumption in equation (1.4) leads to $\epsilon_1' \approx \epsilon'$. From this relation and equations (1.2) and (1.3) it follows that

$$\epsilon_1 \propto \gamma\epsilon_1' \approx \gamma\epsilon' \propto \gamma^2\epsilon. \quad (1.5)$$

Thus, inverse Compton scattering in the Thomson limit increases a target photon's energy by the large factor of about γ^2.
An electron with, for instance, an energy of 500 GeV (this corresponds to a Lorentz factor of about $\gamma \approx 10^6$) scatters a target photon of, say 5×10^{-4} eV (this is a representative energy of a CMB-photon) to typical energies in the order of magnitude of 100 MeVs.
Still, the resulting photon energy is much smaller than the electron energy. Therefore in the Thomson limit, electrons lose only small fractions of their initial energies due to inverse Compton scattering.

IC-Scattering In The Thomson Limit: The Electron's Total Energy Loss Rate

For this work, the total energy loss rate of electrons undergoing inverse Compton scattering in the Thomson limit it of high importance. Like before, the following derivation is adapted from Rybicki and Lightman [21] as well as from Blumenthal and Gould [6].
If $n(p)$ is the photon phase space distribution which is a Lorentz invariant (see, for instance [15]) and $\rho\, d\epsilon$ the density of photons within an energy interval $[\epsilon, \epsilon + d\epsilon]$, then

$$\rho\, d\epsilon = n\, d^3p. \tag{1.6}$$

It is known that under Lorentz transformation d^3p transforms like ϵ, which is why d^3p/ϵ is a Lorentz invariant. Using this in equation (1.6), it results that also $\rho\, d\epsilon/\epsilon$ is a Lorentz invariant:

$$\frac{\rho\, d\epsilon}{\epsilon} = \frac{\rho'\, d\epsilon'}{\epsilon'}. \tag{1.7}$$

In the electron's rest frame, the scattered photons correspond to a total emitted power of [21]

$$\frac{dE_1'}{dt'} = \int c\sigma\epsilon_1'\rho'\, d\epsilon', \tag{1.8}$$

where c is the speed of light and σ is the cross section of this process. In the general case, the total cross section of this process σ is obtained from the exact Klein-Nishina formula [6]

$$\frac{\sigma_{exact}}{d\Omega_1' d\epsilon_1'} = \frac{1}{2} r_0^2 \left(\frac{\epsilon_1'}{\epsilon'}\right)^2 \left(\frac{\epsilon'}{\epsilon_1'} + \frac{\epsilon_1'}{\epsilon'} - \sin^2\theta_1'\right) \delta\left(\epsilon_1' - \frac{\epsilon'}{1 + (\epsilon'/mc^2)(1 - \cos\theta_1')}\right), \tag{1.9}$$

where r_0 is the classical electron radius. In the Thomson limit, where $\epsilon' \approx \epsilon_1'$(see equation (1.4)) and $\epsilon'/mc^2 \ll 1$, integrating the Klein-Nishina formula yields the total Thomson cross section $\sigma_T = (8\pi/3)r_0^2$.
Furthermore, in the lab frame the photon energy before scattering is negligible compared to its energy after the process (compare to equation (1.5)). Thus, the emitted photon power in K equals the electron's total energy loss rate dE_e/dt:

$$\frac{dE_1}{dt} = -\frac{dE_e}{dt} \tag{1.10}$$

Because under Lorentz transformation the energy transforms like $dE_1 = \gamma dE_1'$, such as the time interval $dt = \gamma dt'$, the emitted photon power (1.8) is a Lorentz invariant. It follows that

$$-\frac{dE_e}{dt} = \frac{dE_1}{dt} = \frac{dE_1'}{dt'} = c\sigma_T \int \epsilon_1'\rho'\, d\epsilon'. \tag{1.11}$$

In the Thomson limit it holds $\epsilon_1' \approx \epsilon'$. Because of that and using the Lorentz invariance of $\rho\, d\epsilon/\epsilon$ as well as relation (1.2), the electron's energy loss rate is given by

$$-\frac{dE_e}{dt} = c\sigma_T \int \epsilon'^2 \frac{\rho'\, d\epsilon'}{\epsilon'} = c\sigma_T\gamma^2 \int (1 - \cos\theta)^2 \epsilon\rho\, d\epsilon. \tag{1.12}$$

Assuming the photon field to be isotropic, averaging over angles gives $\langle(1-\cos\theta)^2\rangle = 4/3$. This fact, together with the photon field's energy density $w_{ph} = \int \epsilon\rho \, d\epsilon$ yields the important final result for the total energy loss rate:

$$\frac{dE_e}{dt} = -\frac{4}{3}\sigma_T c w_{ph}\gamma^2 = -\frac{4}{3}\frac{\sigma_T c w_{ph}}{(mc^2)^2}E_e^2. \tag{1.13}$$

As one can see, the total electron energy loss rate is proportional to the squared electron's energy.

The Inverse Compton Photon Spectrum Per Electron

Another important quantity for this work is the photon spectrum emitted by a single electron while undergoing inverse Compton scattering. The following derivation is again based on the work by Blumenthal and Gould [6]. In the following discussion, no assumptions about a scattering regime are being made. Thus, the result is universally valid and not confined to a specific scattering regime.
Figure 1.6 shows a sketch of the inverse compton scattering process in the electron's rest frame K'.

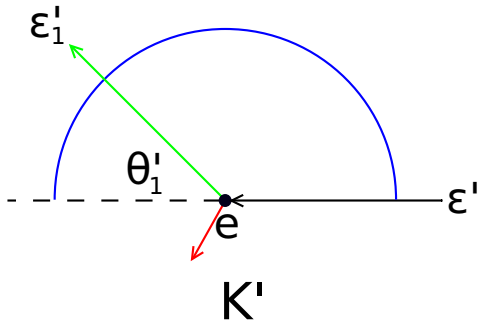

Figure 1.6: Sketch of the IC scattering process (adapted from Blumenthal and Gould [6]).

In the frame K', the distribution of scattered photons emitted by a single electron within a time interval dt into a solid angle $d\Omega'$ and a scattering energy interval $d\epsilon_1'$ for incident photons out of an energy interval $d\epsilon'$ is given by [6]

$$\frac{dN_{IC}}{d\epsilon_1' d\Omega_1' dt' d\epsilon'} = \big(\rho(\epsilon)(\epsilon'/2\epsilon^2\gamma)S(\epsilon';\epsilon/2\gamma,2\gamma\epsilon)d\epsilon\big)\, c\cdot\left(\frac{d\sigma}{d\Omega_1' d\epsilon_1'}\right), \tag{1.14}$$

where the last term is the exact differential Klein-Nishina cross section, $\rho(\epsilon)$ is the spectral target photon density of the radiation field and a step function S has been introduced

$$S(z;a,b) = \begin{cases} 1 & a < z < b \\ 0 & \text{else.} \end{cases} \tag{1.15}$$

In this model gray-body distributions

$$\rho(\epsilon) = \frac{15 w_{ph}}{\pi^4 (kT)^4} \frac{\epsilon^2}{\exp\left[\epsilon/kT\right] - 1}, \tag{1.16}$$

where k is the Boltzmann constant and T is the radiation field's temperature, for the different radiation fields are assumed. To obtain the emitted photon spectrum from a single electron, one has to change coordinates to the lab frame and to integrate over the opening angle as well as the target radiation field energy:

$$\frac{dN_{IC}}{d\epsilon_1 dt} = \iint\limits_{(\epsilon', \Omega_1')} \frac{dN}{d\epsilon_1' d\Omega_1' dt' d\epsilon'} \frac{dt'}{dt} \frac{d\epsilon' d\Omega_1' d\epsilon_1'}{d\epsilon_1}.$$

The result describes the emitted photon spectrum by a single electron due to inverse compton with a target photon of energy ϵ:

$$\frac{dN_{IC,\epsilon}}{d\epsilon_1 dt} = \frac{2\pi r_0^2 c}{\gamma^2} \frac{\rho(\epsilon) d\epsilon}{\epsilon} \left[2q \ln q + (1+2q)(1-q) + \frac{1}{2} \frac{(\Gamma q)^2}{1+\Gamma q} (1-q) \right], \tag{1.17}$$

with the quantities $\Gamma = 4\epsilon\gamma/m_e c^2$ and $q = E/(\Gamma \times (E_e - \epsilon_1))$. Γ is a parameter that determines the domain of the radiation process: For $\Gamma \ll 1$ the scattering occurs in the Thomson-limit whereas $\Gamma \gg 1$ indicates that the inverse compton process takes place in the extreme-Klein-Nishina regime.
The upscattered photon must posses at least the energy it had before the process, $\epsilon_1 \geq \epsilon$. The uppermost energy that may be obtained is the incident electron's energy, so that $\epsilon_1 \leq E_\mathrm{e}$. In general, the energetic boundaries for the emitted photon are [6]

$$\epsilon \leq \epsilon_1 \leq E_\mathrm{e} \big[\Gamma/(1+\Gamma) \big], \tag{1.18}$$

changing with the regime of the radiation process.
The emissivity (1.17) corresponds to the number of emitted photons with energies $[\epsilon_1, \epsilon_1 + d\epsilon_1]$ due to scattering with a target photon of energy ϵ.
To obtain the number of photons emitted into $[\epsilon_1, \epsilon_1 + d\epsilon_1]$ due to scattering with target photons of all energies, expression (1.17) has to be integrated over the target photon energy:

$$\frac{dN_{IC}}{d\epsilon_1 dt} = \int d\epsilon \, \frac{dN_{IC,\epsilon}}{d\epsilon_1 dt}. \tag{1.19}$$

IC-Scattering In The Klein-Nishina Limit

In the Klein-Nishina limit, where relation $\epsilon' \gg mc^2$ holds, the electron loses a substantial fraction of its initial energy in the scattering process. The discontinuous character of inverse Compton scattering in the Klein-Nishina regime will be considered in the fourth chapter of this work.
However, since the emitted inverse Compton photon spectrum per electron (1.17)

is valid also in the Klein-Nishina limit, the total energy loss of the electron in this regime may be obtained by performing the integration

$$-\frac{dE_e}{dt} = \int \epsilon_1 \left(\frac{dN}{dt d\epsilon_1}\right) d\epsilon_1, \tag{1.20}$$

assuming that the initial photon's energy is negligible compared to its energy after scattering.
In the case of the target photon field being spectrally distributed like a black-body

$$\rho = [\pi^2(\hbar c)^3]^{-1} \frac{\epsilon^2}{\exp[\epsilon/kT] - 1}, \tag{1.21}$$

and assuming $\Gamma \gg 1$, Blumenthal and Gould [6] derived an analytical solution of integral (1.20):

$$-\frac{dE_e}{dt} = \frac{\sigma_T (mckT)^2}{16\hbar} \left(\ln \frac{4E_e kT}{(mc^2)^2} - \frac{5}{6} - C_E - C_l\right), \tag{1.22}$$

with the constants $C_E = 0.5772$ and $C_l = 0.57$.
Hence, in the Klein-Nishina limit the energy loss rate only increases in a logarithmic manner with the electron energy, other than in the Thomson limit, where the energy loss rate it proportional to E_e^2.

1.2.2 Synchrotron Radiation

Magnetic fields accelerate moving electrons, who in turn radiate away photons. If the electrons move at relativistic speeds, this radiation is called synchrotron radiation.
It follows a derivation of the total electron energy loss rate and the emitted photon spectrum by a single electron. This derivation is again based on the considerations made by Blumenthal and Gould [6].

The geometry of the scattering is displayed in figure 1.7.

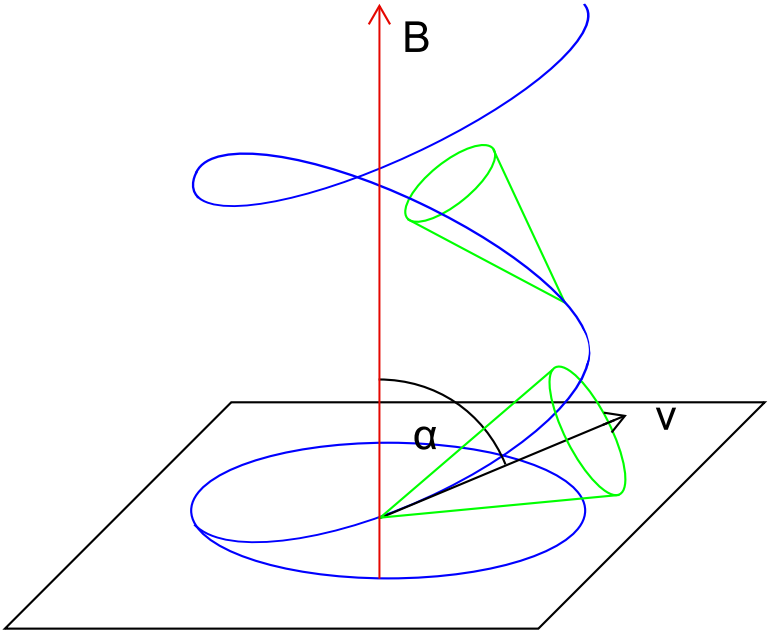

Figure 1.7: A relativistic electron spiraling along the magnetic field, emitting synchrotron radiation (adapted from Rybicki and Lightman [21]).

An electron spirals along a magnetic field line. The angle between the field and the electron's velocity is called the pitch angle α. Due to the electron's relativistic velocity, the emitted radiation is confined to a narrow cone of angular width $\sim \gamma^{-1}$ around the electron's direction of motion.

Synchrotron Radiation: Photon Energy After Scattering

As mentioned before, synchrotron radiation can be understood as inverse Compton scattering of the electron with the virtual photons of the magnetic field. In the electron's frame K' these virtual photons are typically of energy $\hbar\omega_c'$, where $\omega_c' = \gamma\omega_c \sim \gamma eB/m$ is the cyclotron frequency. From the electron's point of view,

this is the characteristic frequency with which the magnetic field varies. Since K' in this case is not an inertial system, one chooses an inertial frame of reference L', in which the electron moves at non relativistic velocity.
If the relation

$$\gamma\hbar\omega_c \ll mc^2 \tag{1.23}$$

holds, i.e. if in L' the virtual quantum's energy is much smaller than the electron's energy, the scattering corresponds to inverse Compton scattering in the Thomson regime. Requirement (1.23) holds for all but extremely high electron energies, which are not subject of this work. Hence, for the scattered virtual photon energy holds $\epsilon_s \approx \hbar\omega'$ (like in the case of Thomson IC-scattering, where $\epsilon_1' \approx \epsilon'$). Analogously to the derivation of relation (1.5) one can use this fact in equation (1.4). Then it follows for the synchrotron photon in the lab frame that

$$\epsilon_s \propto \epsilon_s' = \hbar\omega' \propto \hbar\gamma^2 eB/m. \tag{1.24}$$

An electron with, for example, 5 TeV would typically emit a photon with energy in the order of magnitude of 1 eV. The same electron undergoing inverse Compton scattering would emit a photon with an energy in the order of tens of GeV (compare to equation 1.5). This demonstrates that, while being an efficient cooling mechanism for high energetic electrons (this will be discussed in the next paragraph), synchrotron radiation does not contribute VHE gamma-ray emission.

Synchrotron Radiation: The Electron's Total Energy Loss Rate

The total electron energy loss rate due to synchrotron radiation is derived analogously to the total inverse Compton electron energy loss rate (1.13) in the Thomson limit.
The photon field energy density is replaced by the magnetic field density $U_B = B^2/8\pi$. The assumption of an isotropic target photon field in equation (1.13) corresponds in this case to a isotropic pitch angle distribution. Thus, the averaging of over random scattering angles $(1-\cos\theta)^2$ is replaced by the averaging over random direction of electrons in respect to the field, leading to the same value $\langle(1-\cos\alpha)^2\rangle = 4/3$. The result for the electron's total energy loss rate due to synchrotron scattering is

$$\frac{dE_e}{dt} = -\frac{4}{3}\sigma_T c U_B \gamma^2 = -\frac{4}{3}\frac{\sigma_T c U_B}{(mc^2)^2}E_e^2 \tag{1.25}$$

which is identical to the loss rate for inverse Compton scattering in the Thomson limit (1.13) except that the photon field energy density w_{ph} is replaced by the magnetic field energy density U_B.

Synchrotron Radiation: The Photon Spectrum Per Electron

The discussion of the other important quantity, the emitted photon spectrum by a single electron due to synchrotron radiation, is complex and goes beyond the scope of this short introduction to radiative processes of electrons. Hence, only the result of the emitted synchrotron power per frequency for an electron with arbitrary pitch angle will be presented [6]:

$$P(\nu) = \frac{\sqrt{3}e^3 B \sin\alpha}{mc^2}\left(\frac{\nu}{\nu_c}\right)\int\limits_{(\nu/\nu_c)}^{\infty} K_{\frac{5}{3}}(\zeta)d\zeta, \tag{1.26}$$

where a critical frequency $\nu_B = 3eB\gamma^2/(4\pi mc^2)$ is defined.

Ghisellini et al. [12] found for the synchrotron emissivity, i.e. the energy emitted by one electron into a frequency interval dν per unit time dt:

$$\frac{dE_{Sy}}{d\nu dt} \equiv \epsilon(\nu,\gamma) \simeq \frac{4\pi\sqrt{3}e^2\nu_B}{c}x^2\left[K_{4/3}(x)K_{1/3}(x) - \frac{3}{5}x\big(K^2_{4/3}(x) - K^2_{1/3}(x)\big)\right], \tag{1.27}$$

where dE_{Sy} is the emitted energy, ν is the photons' frequency, γ the Lorentz-factor of the radiating electron, and e the electron's charge. The quantity x is the ratio $\nu/3\gamma^2\nu_B$ and K_{i} are the modified Bessel functions of order i.
$\epsilon(\nu,\gamma)$ is the synchrotron emission integrated over a pitch angle distribution that is assumed to be isotropic and is valid for electron energies corresponding to $\gamma \gtrsim 2$.
Using $E_{Sy} = E\,N(E)$ and $E = h\nu$, it follows for the synchrotron photon spectrum emitted by a single electron

$$\frac{dN_{\mathrm{Sy}}}{dEdt} = \frac{\epsilon(\nu,\gamma)}{hE}. \tag{1.28}$$

In this work, equation (1.28) will be used as photon spectrum emitted by a single electron due to synchrotron radiation.

1.2.3 Bremsstrahlung

If electrons pass through the Coulomb fields of the ISM's ions and atom's nuclei, they get accelerated and emit photons in the process. This radiation mechanism is called Bremsstrahlung.
Compared to inverse Compton scattering and synchrotron radiation, Bremsstrahlung plays only a minor role for electrons at very high energies. This is because the total electron energy loss rate is only linearily proportional to the electron energy ($(dE/dt)_{Brems} \propto nE_e$, where n is the target number density [6]) whereas the loss rate due to synchrotron and inverse Compton scattering shows a quadratic electron energy dependence (compare to equations (1.13) and (1.25)). Usually the target density n is too small to compensate for this difference in energy dependence. Therefore, Bremsstrahlung is neglected in this work. Still, it is a fundamental radiative mechanism of electrons and will therefore be discussed briefly, following considerations by Rybicki and Lightman [21].

Figure 1.8 displays the geometry of the Bremsstrahlung scattering process.

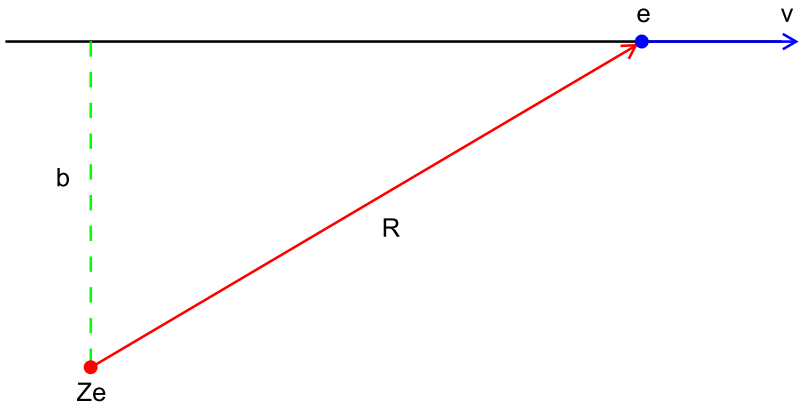

Figure 1.8: Geometry of the Bremsstrahlung scattering process (adapted from Rybicki and Lightman [21]).

An electron moves by a charged ion or nucleus with velocity v and an impact parameter b. The following discussion holds for relativistic Bremsstrahlung, where the electron's velocity $v \rightarrow c$ is close to the speed of light.
As already mentioned, Bremsstrahlung can be regarded as a special case of inverse Compton scattering. Transforming into the electron's rest frame, the ion seems to move towards the electron at a relativistic speed. In that case, the ion's Coulomb field is transformed into an electromagnetic pulse radiated into a solid angle $\Omega \propto \gamma^{-1}$ centered on the electron's position (see, for example [21]). This virtual quantum conducts inverse Compton scattering with the electron and results as radiation in the lab frame.

In the electron's rest frame K' the spectrum of incident virtual photons is [21]

$$\frac{dW'}{dA'd\omega'}(\text{erg cm}^{-2}\text{Hz}^{-1}) = \frac{(Ze)^2}{\pi^2 b'^2 c}\left(\frac{b'\omega'}{\gamma c}\right)^2 K_1^2\left(\frac{b'\omega'}{\gamma c}\right), \tag{1.29}$$

where K_1 is the modified Bessel function of order one. In order to determine the scattered radiation, one has to use the exact Klein-Nishina cross section. However, in the low frequency limit where the virtual photon's energy in the electron rest frame K' is much smaller than the electron energy, $\hbar\omega' \lesssim mc^2$, the scattering occurs in the Thomson limit. Thus, the Thomson cross section σ_T may be used instead. The scattered radiation in the electron's rest frame is then given by [21]

$$\frac{dW'}{d\omega'} = \sigma_T \frac{dW'}{dA'd\omega'}. \tag{1.30}$$

This quantity needs to be transformed into the lab frame K. Since frequency and energy transform similar under Lorentz transformation, the quotient (1.30) is a Lorentz invariant. The same holds for the impact parameter, as it is perpendicular to the moving direction. The symmetry of the scattering leads to an averaged relation $\omega = \gamma\omega'$ [21]. It follows for the emission in the lab frame

$$\frac{dW}{d\omega} = \frac{8Z^2e^6}{3\pi b^2 c^5 m^2}\left(\frac{b\omega}{\gamma^2 c}\right)^2 K_1^2\left(\frac{b\omega}{\gamma^2 c}\right), \tag{1.31}$$

which is the emitted energy per unit frequency resulting from a Bremsstrahlung scattering event of one electron at impact parameter b with one ion of charge Ze.

Looking at a density n_e of electrons traversing a plasma of density n_i, the flux of electrons incident on a ion in the ultra-relativistic limit is $n_e \cdot c$ with respect to the differential area $2\pi b db$. Then the integration

$$\frac{dW}{d\omega dV dt} = n_e n_i 2\pi c \int_{b_{min}}^{\infty} \frac{dW(b)}{d\omega} b\, db, \tag{1.32}$$

corresponds to the total emitted energy per time, space and frequency from an ensemble of electrons traversing a plasma [21]. The lower limit of the impact parameter is limited by the uncertainty principle, $b_{min} \propto h/mc$. Integral (1.32) can be evaluated [21] and results in

$$\frac{dW}{d\omega dV dt} \approx \frac{16Z^2e^6 n_e n_i}{3c^4 m^2} \ln\left(\frac{0.68\gamma^2 c}{\omega b_{min}}\right). \tag{1.33}$$

If the scattering does not occur in the low frequency limit, i.e. $\hbar\omega > mc^2$, it does not correspond to IC-scattering in the Thomson regime and the full Klein-Nishina cross section has to be used.

2 A Gamma-Ray Emission Model For Pulsar Wind Nebulae

In this chapter I present a simple model to describe the gamma-ray emission from single pulsar wind nebulae (PWNe). The model contains electron propagation by diffusion (other propagation mechanisms are neglected) and cooling by inverse Compton scattering and synchrotron radiation. The diffusion is assumed to be energy dependent, meaning that higher energetic electrons diffuse faster than their lower energetic counterparts. Two pulsar scenarios are considered:

- a burst-like injection scenario, where the pulsar releases its rotational energy instantly in the form of electron-positron pairs and
- a continuous injection scenario, in which the pulsar releases these pairs over time with a time dependent luminosity.

In order to model the gamma-ray emission from single PWNe, the following steps are performed:

- Calculation of the electron density (in this and the following chapters both electrons and positrons will be simply adressed as electrons) caused by the pulsar at any point in space and time by solving the diffusion equation. Section 2.1 is dedicated to that problem.
- Calculation of the gamma-ray flux by performing a line-of-sight integration through the pulsar wind nebula. This is necessary since, assuming the nebula to be optically thin, the observed gamma-ray flux from the object is a superposition of gamma-rays emitted by all space elements in the observing direction. Section 2.2 discusses that calculation.

This procedure is done for both cases, the continuous injection scenario and the burst-like injection scenario. In every section, the treatment of the two scenarios is discussed separately.
The chapter closes with the application of the model on the nearby Geminga PWN, presented in section 2.3. The obtained angular profile of the gamma-ray emission will be adapted to the angular resolution of the H.E.S.S. experiment. The H.E.S.S. experiment is an array consisting of four Cerenkov telescopes located in the Khomas highlands in Namibia. It observes the sky at energies between 100 GeV and 100 TeV with an energy resolution of about 20%. The angular resolution of H.E.S.S. is between 0.05 and 0.2 degrees, depending on the

observational direction and the energy of the gamma-ray emission. For further details see [3].

2.1 The Electron Density

The first step towards a model for the gamma-ray emission from single pulsars is to know the electron density at every energy, time and location in the PWN. How this is achieved will be the topic of this section.

2.1.1 The Diffusion Equation

The temporal and spatial evolution of the electron density $N(E, \mathbf{r}, t)$ is described by the diffusion equation [5]:

$$\frac{\partial N}{\partial t} - D\Delta N + \frac{\partial}{\partial E}(\dot{E}N) = Q(E, \mathbf{r}, t), \tag{2.1}$$

where $D = D(E)$ is the diffusion coefficient and $\dot{E} = \dot{E}(E)$ is the energy loss rate.

The first term represents the change of the electron density in $[E, E+dE]$ with time, whereas the second term describes the spatial diffusion of the particles. In general, the diffusion coefficient can depend on the energy of the particles, their position and the time, i.e. $D = D(E, r, t)$. However, in this model D is restricted to depend only on the electron energy E. This simplification allows for a (semi)analytical solution which, as a result, is spherically symmetric.
The third term $\partial(\dot{E}N)/\partial E$ describes the electron's energy loss. It can be seen as the electron's motion in energy space, which can be understood by the following considerations:
$N(E, \mathbf{r}, t)\ dE\ d^3\mathbf{r}$ is the number of electrons in volume $d^3\mathbf{r}$ and within the energy interval $[E, E + dE]$.
Within the time interval $[t, t+dt]$, $N(E, \mathbf{r}, t)dE/dt\ d^3\mathbf{r} = N(E, \mathbf{r}, t)\dot{E}(E)\ d^3\mathbf{r}$ electrons enter the energy interval and $N(E + dE, \mathbf{r}, t)\dot{E}(E + dE)\ d^3\mathbf{r}$ electrons are leaving it per unit time due to energy losses. The last term can be linearized in dE and series expansion yields

$$N(E + dE, \mathbf{r}, t)\dot{E}(E + dE)\ d^3\mathbf{r} \approx$$
$$N(E, \mathbf{r}, t)\dot{E}(E)\ d^3\mathbf{r} + N(E, \mathbf{r}, t)\frac{\partial \dot{E}(E)}{\partial E}\ dE\ d^3\mathbf{r} + \frac{\partial N(E, \mathbf{r}, t)}{\partial E}\dot{E}(E)\ dE\ d^3\mathbf{r} + O((dE)^2)$$

leading to

$$N(E, \mathbf{r}, t)\dot{E}(E)\ d^3\mathbf{r} - N(E+dE, \mathbf{r}, t)\dot{E}(E+dE)\ d^3\mathbf{r} \approx -\frac{\partial}{\partial E}(N(E, \mathbf{r}, t)\dot{E}(E))\ dE\ d^3\mathbf{r}, \tag{2.2}$$

which shows that the change of electrons within the intervals [E, $E + dE$] and [$\mathbf{r}^3$, $\mathbf{r}^3 + d^3\mathbf{r}$] is indeed given by the third term in equation (2.1).

As was shown in chapter two, the total electron energy loss rate for synchrotron radiation and inverse Compton scattering in the Thomson limit is

$$\dot{E}(E) \propto -E^2. \tag{2.3}$$

As a simplification, this loss rate is used in this model. At higher energies , however, this assumption is only a approximation and limits the validity of this model in the deep Klein-Nishina regime.
The term on the right-hand side in equation (2.1) describes the intensity of the cosmic electron source. $Q(E, \mathbf{r}, t)\ dE\ d^3\mathbf{r}$ is the number of electrons injected into $[E, E + dE]$ and $[\mathbf{r}, \mathbf{r} + d^3\mathbf{r}]$ within the time dt.
In the strict sense one should also include two additional terms, as pointed out by Ginzburg and Syrovatskii [13]:

- a term that allows for catastrophic energy losses, as well as
- one that describes statistical fluctuations in the energetic processes electrons are involved in.

Catastrophic energy losses cause the electron to lose that much energy that it is instantly knocked out of the energy interval of interest. In a manner of speaking it gets lost as far as the diffusion model is concerned. The term describing this kind of losses is as follows:

$$-pN = -\frac{1}{T}N = -nv\sigma N,$$

where p is the probability per unit time for that process to occur, T the mean lifetime for such an event, n the medium's particle density, v the particle's velocity and σ the cross section of the process.
However, since energy losses in the Thomson limit are assumed, electrons in this model lose only a small fraction of their original energy (see section 1.2.1). Thus, catastrophic events are ruled out under that assumption.
The second term that was mentioned would allow for statistical fluctuations in the energetic processes the electrons are involved in:

$$\frac{1}{2}\frac{\partial^2}{\partial E^2}(d \cdot N),$$

where $d = d(E) = \frac{d}{dt}\langle(\Delta E^2)\rangle$ the mean square of the energy change per unit time. The fluctuations in cooling processes are small so they do not have to be accounted for.

2.1.2 Solving The Diffusion Equation

It is possible to solve the differential equation using Green's Calculus, as it was shown by Ginzburg and Syrovatskii [13] and will be presented in the following. The Green function solves the following equation:

$$\frac{\partial G}{\partial t} - D\Delta G + \frac{\partial}{\partial E}(\dot{E}G) = \delta(E - E_0)\delta(\mathbf{r} - \mathbf{r}_0)\delta(t - t_0), \tag{2.4}$$

i.e. where $Q(E, \mathbf{r}, t) = \delta(E - E_0)\delta(\mathbf{r} - \mathbf{r}_0)\delta(t - t_0)$ which is a point-like source in energy, space and time.
Introducing the variables $t' = t - \tau$ and λ, with

$$\tau \equiv \tau(E, E_0) = \int_{E_0}^{E} \frac{dE'}{\dot{E}(E')} \tag{2.5}$$

and

$$\lambda \equiv \lambda(E, E_0) = \int_{E_0}^{E} \frac{D(E')}{\dot{E}(E')} dE', \tag{2.6}$$

the diffusion equation transforms into a differential equation of the thermal conductivity type [23]. The solution to this is

$$G(E, \mathbf{r}, t; E_0, \mathbf{r}_0, t_0) = \frac{1}{|\dot{E}(E)|(4\pi\lambda)^{3/2}} \exp\left[-\frac{(\mathbf{r} - \mathbf{r}_0)^2}{4\lambda}\right] \delta(t - t_0 - \tau). \tag{2.7}$$

The time t' represents the mean time needed for the electron to be cooled down from E_0 to E, λ is the mean square of the distance the electron traverses while being cooled down to E.
Using the Green function yields the solution of equation (2.1):

$$N(E, \mathbf{r}, t) = \iiint_{-\infty}^{+\infty} d^3\mathbf{r}_0 \int dE_0 \int_0^t dt_0 \, Q(E_0, \mathbf{r}_0, t_0) G(E, \mathbf{r}, t; E_0, \mathbf{r}_0, t_0). \tag{2.8}$$

This solution puts no constraint on the source term

$$Q(E_0, \mathbf{r}_0, t_0) = Q'(E_0) f(\mathbf{r}_0) g(t_0). \tag{2.9}$$

The functions f and g reflect the spatial and temporal characteristics of the electron source.

I investigated two scenarios:

- burst-like injection, where the object releases its rotational energy instantly, and
- continuous injection, where the object's electron luminosity decreases steadily with time.

At first I will present the model in the burst-like scenario, after that I will display my findings for the case of continuous injection. In both cases the source is assumed to be point-like, leading to a delta-distributed source function in space ($f(\mathbf{r}_0) = \delta(\mathbf{r}_0)$). This assumption is justified for the following reason: The high energy electrons emitting the VHE gamma radiation are generated at the PWN's termination shock (see section 1.1), which typically is of an extension of ~ 0.1 pc. This is very small compared to the PWN's dimension as obtained by this model, usually larger than 10 pc.

Furthermore, the following assumptions were made:

- $Q'(E) = Q_0 E^{-\alpha} e^{-E/E_{cut}}$, i.e. an injected power-law with exponential cut-off at E_{cut} as proposed by e.g. Kobayashi [17],
- $\dot{E}(E) = \dot{E}(E)_{Synchrotron} + \dot{E}(E)_{IC} = -bE^2$ where $b = \frac{4\sigma_T c}{3(m_e c^2)^2}(U_B + w_{CMB} + w_{IR} + w_{OPT})$. This is the combined total electron energy loss rate due to synchrotron radiation and inverse Compton scattering in the Thomson limit (see chapter two). The coefficient b is a function of the energy densities of the magnetic field (U_B), the CMB (w_{CMB}), the infrared field caused by cosmic dust reflection (W_{IR}) and the optical field produced by stars (w_{OPT}) [6].
- $D(E) = D_0(1 + E/E^*)^\delta$ which allows for a smooth transition of energy dependent diffusion from high towards low energies. This is adapted from the work of Atoyan et al. [5].

Furthermore, the normalization constant $Q_0 = E_g(\int_{E_{min}}^{E_{cut}} dE\ E \cdot E^{-\alpha})^{-1}$ (where E_g is the total energy output in electrons of the pulsar) and the Thomson cross section σ_T are used.
The constant D_0 can be obtained with the assumption $D(10\ \text{GeV}) = 10^{28}\text{cm}^2\text{s}^{-1}$ [5].
The energy $E^* = 3$ GeV as well as the quantities E_{cut}, δ and α (the spectral index), are free parameters in my model.

At this point it is important to mention that the total value and the energy dependency of the diffusion coefficient at very high energies is highly uncertain. It can be estimated by using the ratios of secondary to primary nuclei (B/C) as they were observed by Voyager [18] and HEAO-3-C2 [9]. These estimations are in good agreement with energy dependencies of $D(E) \propto E^0$ at energies $E < 5$ GeV and $D(E) \propto E^{0.6}$ at energies $E > 5$ GeV and a normalization of $D_0 \sim 10^{28}\text{cm}^2\text{s}^{-1}$ [17]. However, the B/C measurements extend only up to tens of GeV and it is not clear if the the energy dependency changes again in the VHE range. Balloon-borne emulsion chamber experiments indicate that δ changes from 0.6 to 0.3 between tens of GeV and 1 TeV [10]. However, this change of δ at higher energies is not included in this model.

Burst-Like Injection Scenario

In the case of burst-like injection the pulsar releases its rotational energy instantly. Hence, the source term resembles a delta-distribution in time:

$$Q(E, \mathbf{r}, t) = Q_0 E^{-\alpha} e^{-E/E_{cut}} \delta(\mathbf{r}) \delta(t) \tag{2.10}$$

By introducing (2.10) into equation (2.8) one obtains

$$N(E, r, t) = Q_0 \left(\frac{E}{1 - Ebt} \right)^{-\alpha} \exp \left[-\frac{E}{E_{cut}(1 - Ebt)} \right] \times \frac{1}{(1 - Ebt)^2 [4\pi\lambda(E, t)]^{3/2}} \exp \left[-\frac{\mathbf{r}^2}{4\lambda(E, t)} \right]. \tag{2.11}$$

This solution is, as already mentioned, spherically symmetric and a Gaussian in r, which is to be expected of a diffusion equation. Its

- spatial properties are determined by the quantity $\lambda(E, t)$. It is the only component of solution (2.11) that is connected to the diffusion coefficient $D(E)$ (compare to equation (2.6)). In this model it is computed numerically as the analytical result is very inconvenient.
  Assuming the special case of $\delta = 0$, i.e. for energy independent diffusion, $D(E) = D_0$ so that

$$\begin{aligned} \sqrt{\lambda(E, t)} &= \left[\int_{E_0}^{E} dE' \, \frac{D(E')}{\dot{E}(E')} \right]^{\frac{1}{2}} \\ &= \left[-\frac{D_0}{b} \int_{E/(1-Ebt)}^{E} \frac{dE'}{E'^2} \right]^{\frac{1}{2}} \\ &= \sqrt{D_0 t}. \end{aligned}$$

  which is, apart from a factor $\sqrt{2}$, the familiar diffusion length for ordinary diffusion.
  Thus, the quantity $\lambda(E, t)$ can be regarded as squared diffusion length for energy-dependent diffusion.

- energetic properties are strongly determined by the energy loss rate $\dot{E}$:
  In the case of burst-like injection, all electrons of the initial population get cooled down for the same amount of time. Therefore, a maximum electron energy, which is determined by the cooling time (in this case the object's age), is expected, as can be understood by the following derivation.
  Because

$$\frac{dE}{dt} = -bE^2 \tag{2.12}$$

it follows

$$\begin{aligned} \int_{t_0 \equiv 0}^{t} dt' &= -\frac{1}{b} \int_{E(t_0)\equiv E_0}^{E(t)} \frac{dE'}{E'^2} \\ t &= \frac{1}{b}\left(\frac{1}{E(t)} - \frac{1}{E_0}\right) \end{aligned} \tag{2.13}$$

which means that an electron with initial Energy E_0 is cooled down to E within the time t. The electron's initial injection energy E_0 is assumed to be much larger than its energy E after being cooled for a time period of t_{age}. As a result the expression simplifies to $t \approx [bE(t)]^{-1}$, so that there is a maximum electron energy for a given cooling time (in this case the object's age t_{age}):

$$E_{max} = \frac{1}{b\, t_{age}} \quad . \tag{2.14}$$

Because of that,

$$N(E, \mathbf{r}, t) = \begin{cases} \text{equation (2.11)} & \text{for} \quad E < E_{max} \\ 0 & \text{otherwise} \quad . \end{cases} \tag{2.15}$$

Hence, the energy loss rate (2.3) causes a spectral cut-off at E_{max} under the assumption of a burst-like injection scenario. In the continuous injection scenario, however, a very different spectral behaviour is observed.

Figure 2.1 shows the electron flux per unit solid angle

$$J(E,r,t) = \frac{c}{4\pi} N(E,r,t) \tag{2.16}$$

assuming the electron's velocity to be the speed of light and for a given source distance r to the observer. Different dependencies of the diffusion on the energy are implemented by different values of δ.

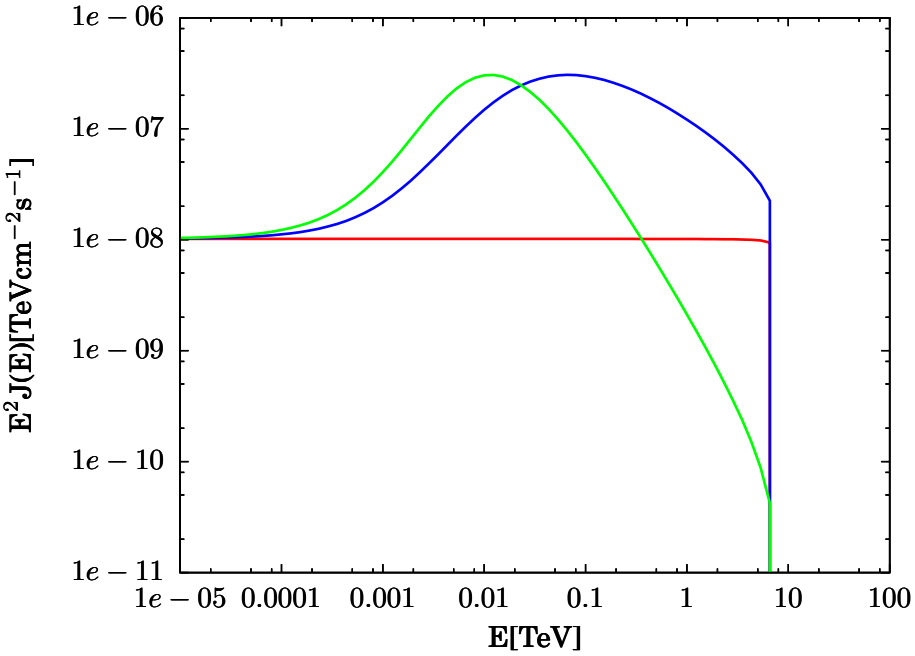

Figure 2.1: Electron flux in the burst-like injection scenario as a function of energy for different values of δ. Red: $\delta = 0$, blue: $\delta = 0.5$, green: $\delta = 1$. $t = 2.5 \times 10^4$ a, $r = 100$ pc, $\alpha = 2$, $E_g = 10^{48}$ erg.

Energy-dependent diffusion ($D = D(E)$) can have a important impact on the electrons' spectral shape. This is because the speed of diffusion, in this model, increases with the electrons' energy.
This can be understood considering an observer at a distance r to the source. For the time an electron needs to traverse this distance one finds that $t(E,r) \propto r^2/D(E)$. In the case of energy-independent diffusion it is $t(E,r) = t(r)$, which means that electrons of all energies reach the observer at the same mean time. Consequently, except for the cut-off, the observer sees the original injection spectrum, namely a power law with a spectral index of 2 (red line in figure 2.1).

Assuming $D = D(E) = D_0(1 + E/E^*)^\delta$, higher energy electrons reach the observer faster than the ones with lower energies, resulting in a general excess

of electrons with $E \gtrsim E^*$. Another consequence is a softening of the injection spectrum towards E_{max} because the bulk of the fastest electrons has already passed the observer, as well as a hardening for $E \simeq E^*$, because compared to energy-independent diffusion, the increased diffusion coefficient leads to an earlier arrival of electrons close to E^*. This in turn leads to a rise in the observer's spectrum at these energies (blue and green lines in figure 2.1). At lower energies the energy dependence is negligible so that the spectra for different δ converge.

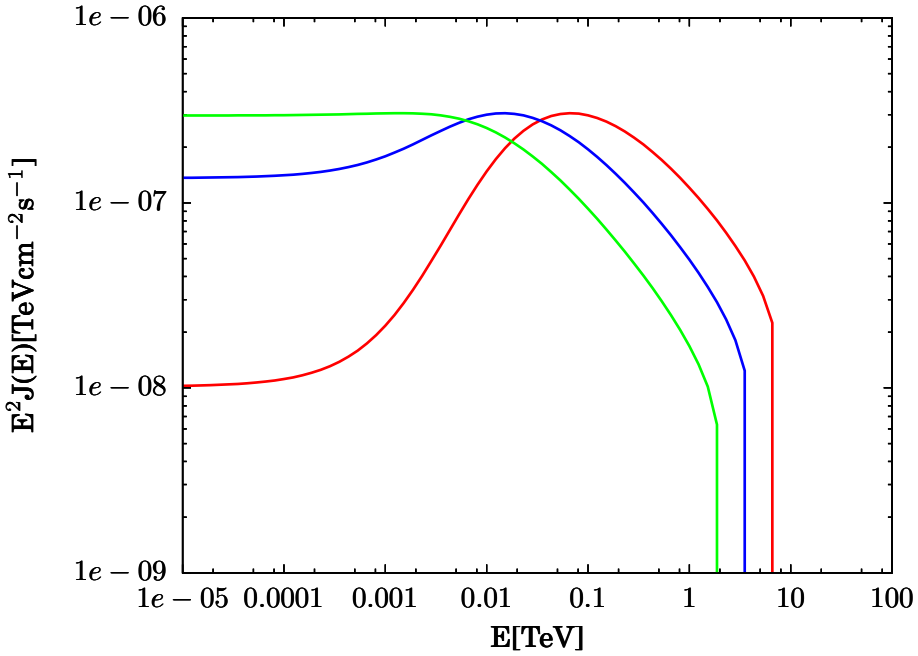

Figure 2.2: Electron flux in the burst-like injection scenario as a function of energy for different ages of the object. Red: 2.5×10^4 a, blue: 5×10^4 a, green: 10^5 a. $r = 100$ pc, $\delta = 0.5$, $\alpha = 2$, $E_g = 10^{48}$ erg.

Figure 2.2 demonstrates that with increasing time the fraction of high energy electrons decreases due to overtaking the observer while the fraction of lower energetic electrons rises. Both effects lead to a softening of the spectrum between E^* and E_{max} as time passes. Additionally, E_{max} decreases with time, as it is expected from equation (2.14).

Figure 2.3 shows $\sqrt{\lambda}$, the electrons' mean travelled distance, as a function of energy. Figure 2.4 displays the radial behaviour of $N(E, r, t)$.
The mean travelled distance λ has a very strong functional dependence on E and since $N(E, r, t)$ is a Gaussian with $\sigma = \sqrt{2\lambda}$ (see equation (2.11)) it is clear that the PWN's dimension varies with the energy, as well as with δ. This can

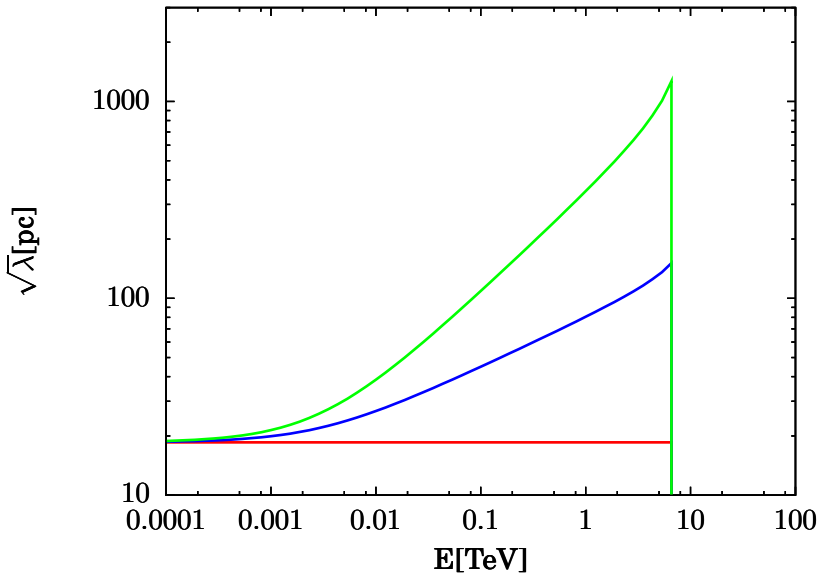

Figure 2.3: The electrons' mean travelled distance λ as a function of E for different values of δ. Red: $\delta = 0$, blue: $\delta = 0.5$, green: $\delta = 1$. $t = 2.5 \times 10^4$ a, $\alpha = 2$, $E_g = 10^{48}$ erg.

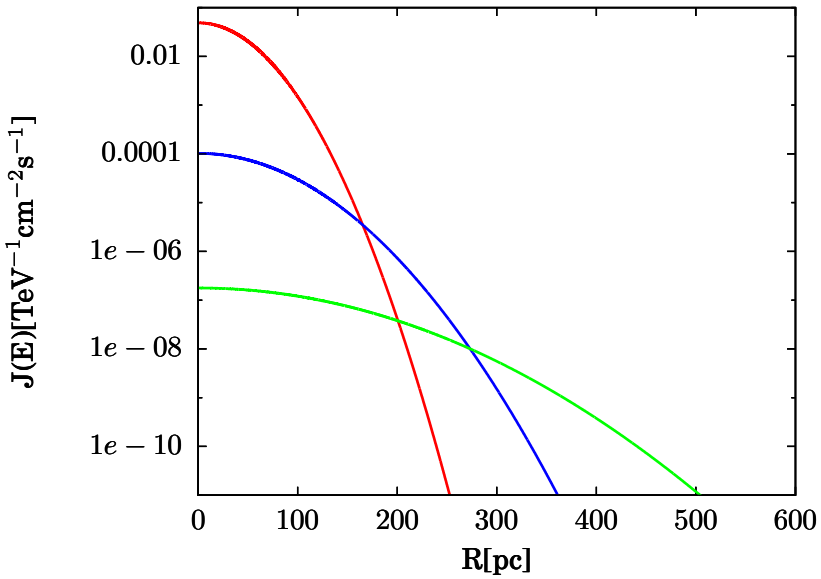

Figure 2.4: Electron flux in the burst-like injection scenario as a function of distance for different electron energies. Red: 0.01 TeV, blue: 0.1 TeV, green: 1 TeV. The object is 25000 years old, $\delta = 0.5$, $\alpha = 2$, $E_g = 10^{48}$ erg.

be seen in figures 2.3 and 2.4.

In a burst-like scenario the PWN at several TeV would be very extended. For instance, the distance where $N(E, r, t)$ has dropped to $N(E, 0, t)/\mathrm{e}$ for 1 TeV would be 320pc using the same parameters as in figure 2.4. Assuming the object to be 1kpc away, the angular radius at 1 TeV would be 17.74 degrees. Comparing that to the 5 degrees field of view in diameter of the H.E.S.S. experiment shows, that gamma rays produced by that object would not be visible with H.E.S.S.

The situation is quite different for continuous injection, where very high energy electrons are located in close proximity to the source. This will be presented in the next section.

Continuous Injection Scenario

In the case of continuous injection, the source term is not a delta-distribution in time, but a decreasing function of time. This is a more realistic scenario since it is impossible for the pulsar to release its rotational energy in one instance. As a consequence, one integration in (2.8) remains. Mathematically, in this case the integrational variable may be chosen (either E_0 or t_0) because the delta function's argument in this case is a function of the energy E_0 as well as the time t_0. The integration is chosen to be over time, and the solution of equation (2.1) is:

$$N(E,r,t) = \int_0^t dt_0\, Q(t_0)\left(\frac{E}{1-Eb(t-t_0)}\right)^{-\alpha} \exp\left[-\frac{E}{E_{cut}(1-Eb(t-t_0))}\right] \times \frac{1}{(1-Eb(t-t_0))^2[4\pi\lambda(E,t,t_0)]^{3/2}} \exp\left[-\frac{\mathbf{r}^2}{4\lambda(E,t,t_0)}\right]. \tag{2.17}$$

Again it is assumed that $Q(E,t_0) = Q_0(t_0)E^{-\alpha}e^{-E/E_{cut}}$, but in this case the source term is time-dependent and a spectral particle emission per time rather than a density. Because of this it follows for the pulsar's luminosity $L(t)$ (the total emitted energy per time) that

$$\int dE\; E\, Q(E,t) = L(t), \tag{2.18}$$

and consequently

$$Q_0(t) = L(t)\left(\int dE E^{-(\alpha-1)}e^{-E/E_{cut}}\right)^{-1}. \tag{2.19}$$

Assuming magnetic dipol braking, $L(t)$ it is given by

$$L(t) = \frac{L_0}{(1+\frac{t}{\tau^*})^{\frac{\kappa+1}{\kappa-1}}}, \tag{2.20}$$

where τ^* is the characteristic timescale in which the pulsar spins down and κ is the magnetic braking index, which is assumed to be $\kappa = 2$.

Because $\int_0^\infty dtL(t) = E_g$ it follows for $L(0) \equiv L_0$:

$$L_0 = E_g\left(\int_0^\infty dt\; (1+\frac{t}{\tau^*})^{-2}\right)^{-1} \tag{2.21}$$

$$= \frac{E_g}{\tau^*}. \tag{2.22}$$

Furthermore, $\int_0^{\tau^*} dtL(t) = \frac{1}{2}E_g$, which means that half of the pulsar's energy is released within τ^*. The characteristic spin-down timescale τ^* is typically believed to be between 100 and 1000 years. Thus, pulsars behave quite burst-like, even in the case of continuous injection.

One can see that in equation (2.17), compared to equation (2.11), the time t is replaced by $(t - t_0)$, which reflects the pulsar's past. While in the case of burst-like injection the solution is a spectrum of equally old electrons, in the scenario of continuous injection the solution is a superposition of spectra with ages $(t - t_0)$. This means, according to equation (2.14), that there is an abundance of high energy electrons, unlike in a burst-like scenario. The smaller $(t-t_0)$, the higher is the maximum electron energy. This leads to the conclusion that in this model very high energy electrons are also very young electrons. Alternatively one could say that very high energy electrons are cooled down very rapidly and do not survive for long, so electrons of that energy have to be of recent origin.

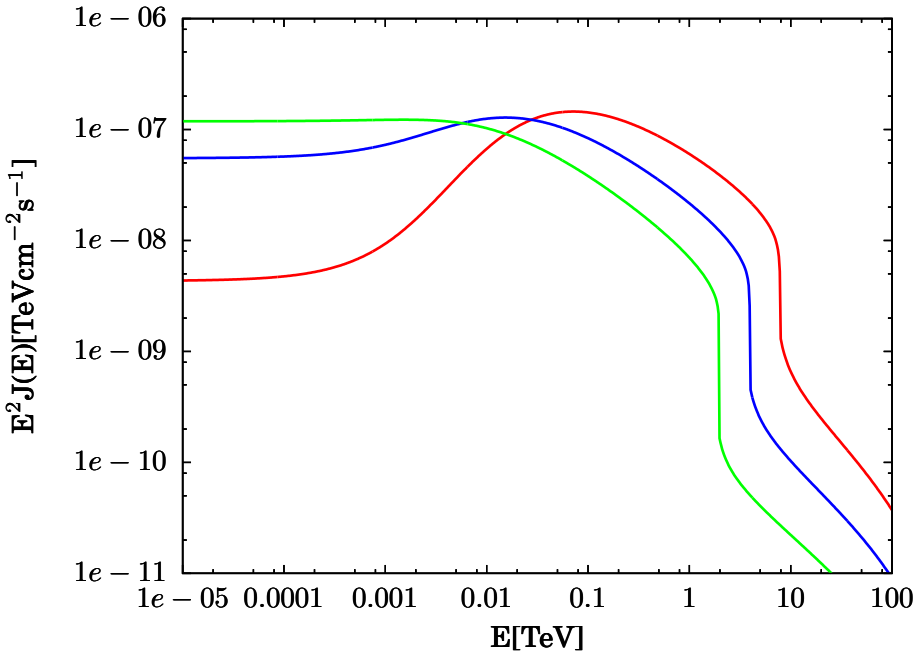

Figure 2.5: Electron flux in the continuous injection scenario as a function of energy for different ages of the object. Red: 2.5×10^4 a, blue: 5×10^4 a, green: 10^5 a. $\delta = 0.5$, $\alpha = 2$, $E_g = 10^{48}$ erg, $\tau^* = 250$ a, $r = 100$ pc.

This effect is visible in figures 2.5 and 2.6 which show the electron flux in the continuous injection scenario for different ages of the object (figure 2.5) and

different energy dependencies of the diffusion (i.e. different values of δ, see figure 2.6). There no longer is a sharp cut-off but a step at $E = E_{max}$. The height of the step (the amplitude of the drop in the flux) increases with the age of the object, since the pulsar's luminosity decreases over time.
Since the majority of the electrons with $E < E_{max}$ is ejected in the first few hundred years of the pulsar's life, the time dependency of the injection plays only a minor role for $E < E_{max}$, provided the age of the object is much bigger than its characteristic spin-down time, and the spectrum is similar to that in the burst-like injection case. Electrons with $E > E_{max}$, on the other hand, are of exclusively recent origin, which is why there is a strong dependency on the temporal evolution of the luminosity. As a result, their intensity decreases with time just like the luminosity does.

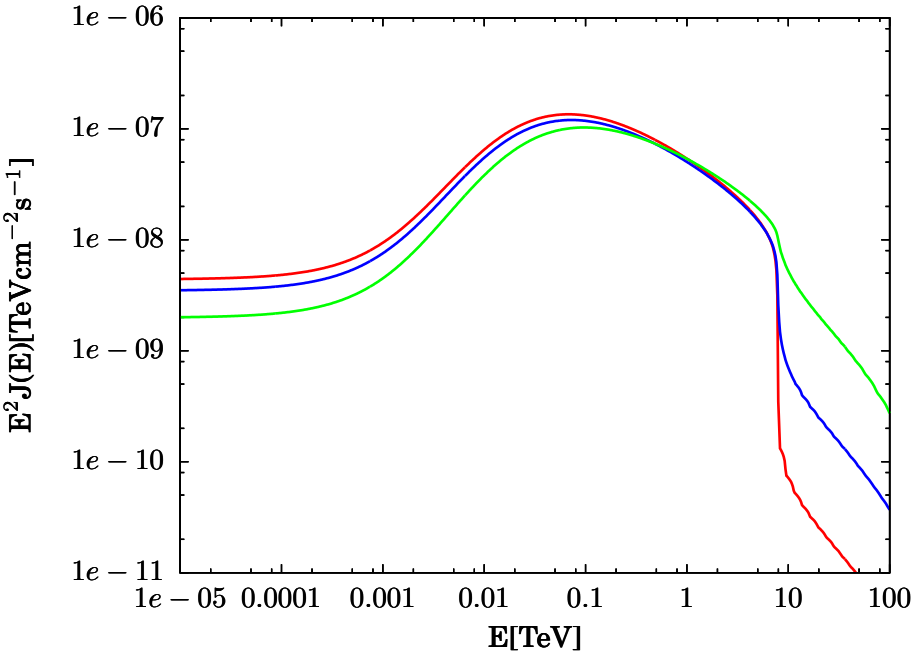

Figure 2.6: Electron flux in the continuous injection scenario as a function of energy for different values of τ^*. Red: $\tau^* = 25$ a, blue: $\tau^* = 250$ a, green: $\tau^* = 2500$ a. $\delta = 0.5$, $\alpha = 2$, $E_g = 10^{48}$ erg, the age is 25000 a, $r = 100$ pc.

Figure 2.6 shows that the step height also depends on τ^*. This is a direct result of equation 2.20. With decreasing spin-down time the step gets higher until finally in the limit $\tau^* \to 0$ it becomes a cut-off and the burst-like scenario is obtained.
The opposite case leads to a increasingly shallow step eventually resulting in the stationary injection scenario where $L(t) = L_0 = \text{const}$.

As mentioned before, the solution for continuous injection is a superposition

of spectra of different ages.

This fact strongly influences the radial behaviour of the electron flux in the case of continuous injection, which is shown in figure 2.7.

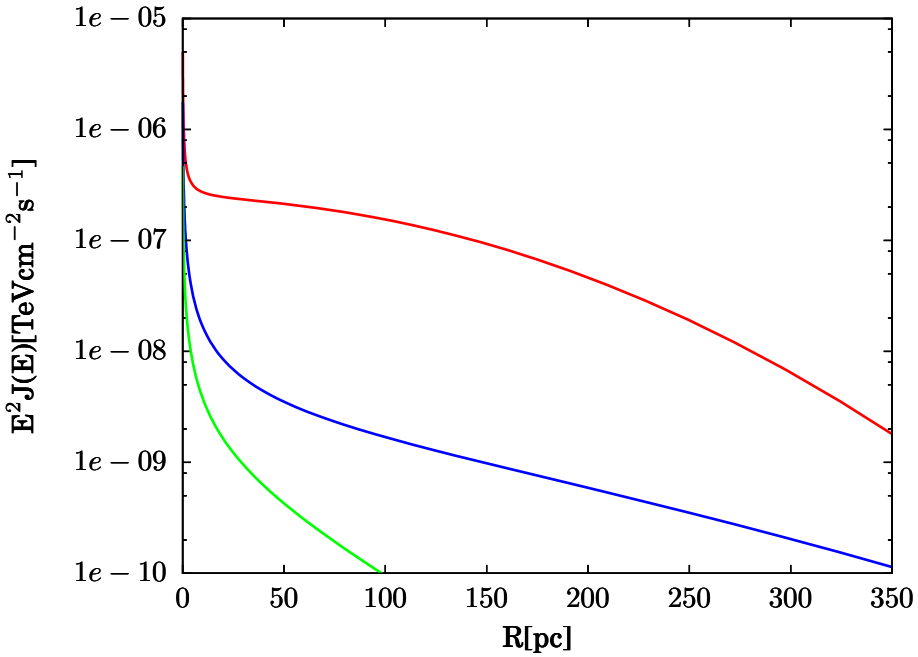

Figure 2.7: Electron flux in the continuous injection scenario as a function of distance for different energies. Red: $E = 1$ TeV, blue: $E = 10$ TeV, green: $E = 100$ TeV. The object is 25000 years old, $\delta = 0.5$, $\alpha = 2$, $E_g = 10^{48}$ erg, $\tau^* = 250$ a.

The radial distribution of the electron flux is shown for three different energies. While the fluxes for 10 TeV and 100 TeV show a very narrow radial distribution, the flux of electrons with an energy of 1 TeV shows quite extended, gauss-like radial characteristics with a superimposed peak at small radii.
This different behaviour can be understood as follows:
While electron energies of 10 TeV and 100 TeV are above the step in the electron spectrum, an electron energy of 1 TeV is below E_{max} (compare to figure 2.6).
As already discussed, the flux at energies $E < E_{max}$ is mainly constituted of electrons that have been ejected in the early times of the pulsar's existence. These electrons diffused for a time that is approximately the object's age. Thus, the situation is quite similar to that in the burst-like injection scenario, where the electron's diffusion time equals the pulsar's age because all electrons have been ejected simultaneously at the pulsar's birth. In the burst like injection scenario it follows that the electrons are radially gauss-like distributed, and such

a component is observed in the continuous injection scenario for the electron flux at energies $E < E_{max}$ (red line in figure 2.7).
At energies $E > E_{max}$, the gauss-like component is not present. This is because the electrons ejected in the early time of the pulsar's life at that energies have already been cooled down.
The flux at that energies exclusively consists of electrons ejected at later times. These electrons cause a narrow radial distribution, since they do not have enough time to travel large distances. The more recent the electron injection, the smaller the travelled distance. Because the pulsar injects continuously, this leads to a pile up of electron density (and thus of electron flux) at the electron source. Additionally, the higher energetic the electrons, the more rapid the radiative cooling. As a consequence, the maximum travelled distance decreases with higher electron energies, since their lifetime (i.e. their travelling time) decreases and the radial distribution narrows.
This behaviour can be observed in figure 2.7 for energies 10 TeV and 100 TeV as well as in form of the peak for electrons with energy 1 TeV.

In summary, in the continuous injection scenario the radial width of the electron distribution decreases with increasing energy, which is opposite to the behaviour in the burst-like injection case.

2.2 The Gamma Flux

The main goal of this work is to describe the gamma ray emission from single PWNe. So far, the electron density - emitted by the pulsar, cooled by synchrotron and inverse Compton losses and propagated by energy dependent diffusion - has been obtained for the two different injection scenarios (burst-like injection and continuous injection). The next section explains, how from this the gamma ray flux, as seen by an observer, is derived.

2.2.1 The General Idea

As it was discussed in chapter two, high energetic electrons are able to undergo radiation mechanisms by which they emit gamma radiation. In this model, only synchrotron and inverse Compton radiation are considered, since only these radiation mechanism contribute significantly to the VHE energy spectrum.
Also in chapter two, the photon spectra emitted by a single electron for synchrotron and inverse Compton radiation ($(dN_{\mathrm{Sy}}/dEdt)$ and $(dN_{IC}/dEdt)$, see equations (1.19) and (1.28)) have been derived.
If one electron emits a spectrum $(dN_{\gamma}^{total}/dEdt) = (dN_{\mathrm{Sy}}/dEdt) + (dN_{IC}/dEdt)$, then a density of electrons $N(E_e, r, t)$ causes a *volume emissivity* of $(dN_{\gamma}/dEdVdt) = \int dE_e \, (dN_{\gamma}^{total}/dEdt) \cdot N(E_e, r, t)$.
This holds for every place in the PWN. Now, if an external observer looks at the PWN, what he sees is a superposition of gamma ray emission out of the infinitesimal volumes that are located along the observational direction (the PWN is treated to be optically thin). The geometry of that problem is shown in figure 2.8.

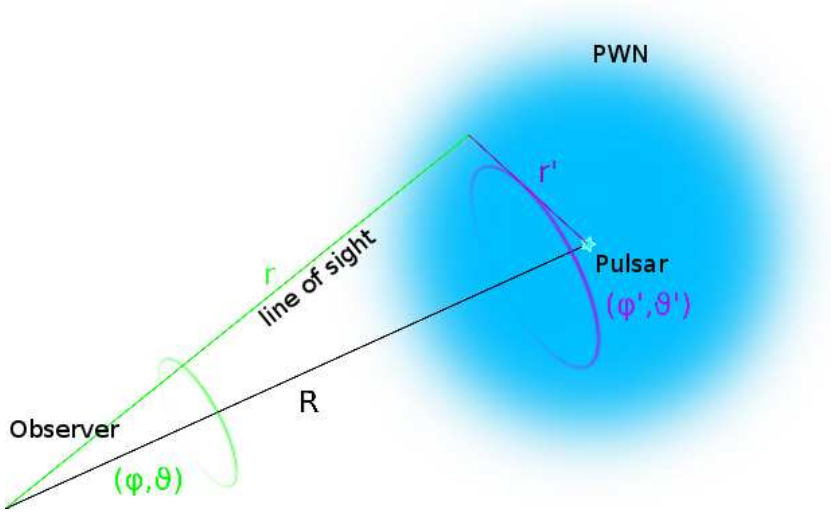

Figure 2.8: Geometrical sketch of the problem

Furthermore, since the observed gamma ray flux drops with distance r to the emitter as $\propto r^{-2}$, the emission out of a volumes at distance r has to be weighted with that factor.
Mathematically, this is accomplished by a line of sight integration, i.e. in this case an integration of $(dN_\gamma/dEdVdt)$ over the observer's line of sight:

$$\frac{dN_\gamma}{dEdAd\Omega dt} = \int_0^\infty dr\ r^2 \left[r^{-2}\ \frac{dN_\gamma}{dEdVdt} \right], \tag{2.23}$$

which is a spectral gamma photon flux per solid angle. Note that r^2 cancelles out because of the weighting.
The complete expression is

$$\begin{aligned}
\frac{dN_\gamma}{dEdAd\Omega dt} &= \int_0^\infty dr \frac{dN_\gamma}{dEdVdt} \\
&= \int_0^\infty dr \int dE_e\ \frac{dN_\gamma^{total}}{dEdt} \cdot N(E_e, \mathbf{r}, t) \\
&= \int_0^\infty dr \int dE_e \left[N(E_e, \mathbf{r}, t) \frac{dN_{\mathrm{Sy}}}{dEdt} + \sum_{i=1}^{3} N(E_e, \mathbf{r}, t) \frac{dN_{IC,i}}{dEdt} \right] \\
&= \int_0^\infty dr \int dE_e \left[N(E_e, \mathbf{r}, t) \frac{dN_{\mathrm{Sy}}}{dEdt} + \sum_{i=1}^{3} \int d\epsilon_i N(E_e, \mathbf{r}, t) \frac{dN_{IC,\epsilon_i}}{dEdt} \right],
\end{aligned} \tag{2.24}$$

where the index i indicates the three different target photon fields (the CMB, the ambient infrared and the ambient optical photon field).
Since the expressions $(dN_\mathrm{i}/dEdt)$ are no functions of the spatial coordinate, the integrals may be swapped:

$$\begin{aligned}
\frac{dN_\gamma}{dEdAd\Omega dt} = \int_{E_{e,min}}^{E_{e,max}} dE_e \Bigg[\frac{dN_{\mathrm{Sy}}}{dEdt} \left(\int_0^\infty dr N(E_e, \mathbf{r}, t) \right) \\
+ \sum_{i=1}^{3} \int d\epsilon_i \frac{dN_{IC,\epsilon_i}}{dEdt} \left(\int_0^\infty dr N(E_e, \mathbf{r}, t) \right) \Bigg].
\end{aligned} \tag{2.25}$$

As one can see, the line-of-sight integral

$$L(E_e, \mathbf{r}, t) \equiv \int_0^\infty dr N(E_e, \mathbf{r}, t) \tag{2.26}$$

can be calculated separately. The advantage in using L is that the folding with the terms $(dN_{\mathrm{i}}/dEdt)$ only has to be performed once and not in every integrational point along the line of sight.
The important expression L will be discussed in the following.

2.2.2 The Electron Line Of Sight Integral

In this model I made the approximation

$$L(E,\mathbf{r},t) \approx \int\limits_{\max(0,R-5\sqrt{\lambda})}^{R+5\sqrt{\lambda}} drN(E,\mathbf{r},t) \tag{2.27}$$

to speed up the program. The observer's distance to the object is given by R. As a result, electrons in the Gaussian's tail directed perpendicular to the line of sight get somewhat overestimated compared to those located in the tail directed parallel to the observational direction. The effect decreases with increasing the integrational radius and for $5\sqrt{\lambda}$ it is negligible, since $N(E,5\sqrt{\lambda},t)/N(E,0,t) = 0.19\%$.

Looking at figure 2.8 points out that the problem is symmetric regarding rotation, so the electron density is not a function of $\varphi = \varphi'$.
Since $\mathbf{r}'$ (see figure 2.8) is a vector based on the position of the source and the electron density function in this frame is a spherical Gaussian centered on it, the electron density at $\mathbf{r}'$ is only a function of its length, $N(E,\mathbf{r}',t) = N(E,r',t)$. The integration is over r, so for every integration point in space the electron density $N(E,r,t) = N(E,r'(r,R,\vartheta),t)$ has to be calculated, using

$$r'(r,R,\vartheta) = \sqrt{r^2 - 2rR\cos\vartheta + R^2}. \tag{2.28}$$

Performing this line-of sight integral and introducing it in (2.25) results, as already mentioned, in a gamma flux per unit solid angle.
In order to get an integrated flux over the observational angle, i.e. a gamma-ray flux out of a solid angle element $\Delta\Omega$, it is necessary to integrate L over ϑ and φ

$$M(E_e,R,\vartheta_{max},t) \equiv \int\limits_0^{2\pi} d\varphi \int\limits_0^{\vartheta_{max}} d\vartheta \sin\vartheta L(E_e,R,\vartheta,t) \tag{2.29}$$

and to introduce this quantity into (2.25) instead of the line-of-sight integral L.

In the following, the properties of L in the burst-like and continuous injection scenario will be discussed.

Burst-Like Injection Scenario

The line-of-sight integral inherits the features of the electron densities it is calculated from. These features are the deformation of the spectrum compared to the injection spectrum due to energy dependent diffusion as well as a cut-off energy in the case of a burst-like scenario.
On the other hand, new attributes are expected: The geometry of the problem now is no longer spherical but rotational symmetric (compare to figure 2.8). Additional features arise due to the fact that the line integral L is the result of an integration weighted with r^{-2} of electron densities at different distances to the source.

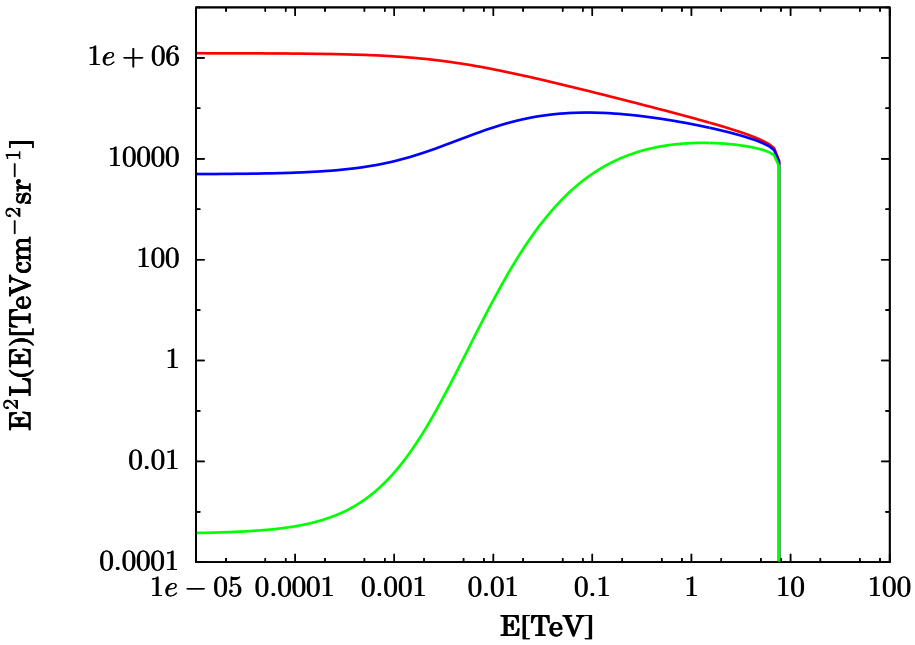

Figure 2.9: Line-of-sight integral in the burst-like injection scenario as a function of energy for different angles. Red: 0 degrees, blue: 5 degrees, green: 10 degrees. The object is 25000 years old, $\delta = 0.5$, $\alpha = 2$, $E_g = 10^{48}$ erg, $r = 1$ kpc.

The spectrum of the line-of sight integral L for different observational angles (the angle between the source and the line-of-sight) is shown in figure 2.9. The spectra differ strongly at lower energies. This is a consequence of energy dependent diffusion: The electrons diffuse at different velocities depending on their energies. The red line is obtained integrating directly through the source. For $E \lesssim E^*$ ($E^* = 3$ GeV is the normalization energy in the diffusion coefficient, see section 2.1.2) the injection spectrum is obtained because the energy dependence of the diffusion is negligible. At higher energies, electrons diffuse faster than

their low energy counterparts and leave the line of sight more rapidly, leading to a drop in the high-energy electron abundance.
Looking not directly at the center of the object but at an offset to it, the spectrum appears quite different (green and blue lines in figure 2.9). There is a drop in column density at lower energies increasing with the angle θ. This is because integrating at an angle next to the center means integrating over electron densities far away from the source. At low energies electrons diffuse slower, and therefore the bulk of those electrons has not reached these remote locations yet, in contrary to their higher energy counterparts who arrive there at a much earlier time and thus show a greater abundance in the spectrum.

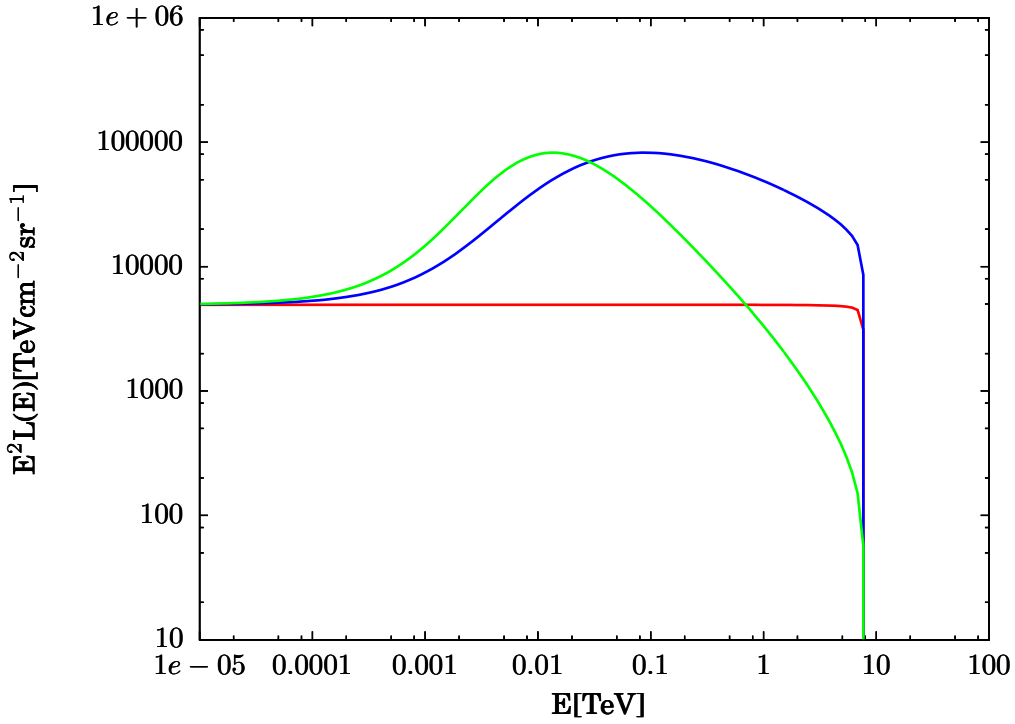

Figure 2.10: Line-of-sight integral in the burst-like injection scenario as a function of angle for different values of δ. Red: $\delta = 0$, blue: $\delta = 0.5$, green: $\delta = 1$. The object is 25000 years old, the angle is 5 degrees, $\alpha = 2$, $E_g = 10^{48}$ erg, $r = 1$ kpc.

Figure 2.10 shows the effect on the spectrum with varying the energy dependence in $D(E)$. It shows a great similarity to figure 2.1 and as a matter of fact, both plots can be explained in a similar way. For energy independent diffusion, which is represented by the red line in figure 2.10, electrons of all possible energies traverse the same mean distance within a given time. Because of that, the spectrum is not subject to the distorting effects of energy dependent diffusion

and thus the spectral shape of the injection spectrum is preserved. In the case of energy dependent diffusion (blue an green lines in figure 2.10), for electrons near the cut-off energy the maximum of the temporal electron density evolution at the integrational points is already over, or in other words, the majority of those electrons has already passed beyond the integrational points. As a result, the electron column density drops at energies near E_{max} This is not yet the case for lower energy electrons and thus, there is a rise in the spectrum until it reaches a maximum at a position depending on the value of δ,which divides the two described energy regimes. For energies $E \lesssim E^*$ the energy dependence becomes negligible and the curves converge.

In the derivation of the electron density (see section 2.1.2), the point of origin was at the source position and the solution of the diffusion equation (i.e. the electron density) was spherically symmetric.
Now the PWN is observed from outside, and thus the spherical symmetry is broken (compare to figure 2.8). The problem is now of rotational symmetry.
Additionally, the line-of-sight integral L is not simply a Gaussian in the distance to the center, but rather
$\propto \int dr \exp -[(r^2 - 2rR\cos\vartheta + R^2)/4\lambda] \propto \exp -[(R\sin\vartheta)^2/4\lambda]$. This means, that the line-of-sight integral has a Gaussian shape in the quantity $R\sin\vartheta$. The geometry of that problem is shown in figure 2.11.

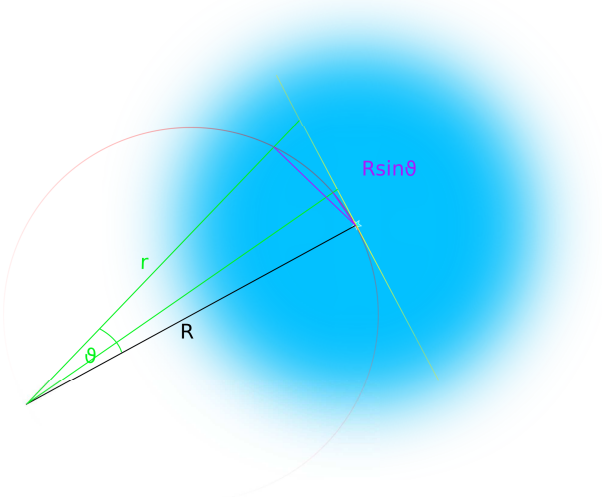

Figure 2.11: Geometrical sketch of the problem. The coordinate $R\sin\vartheta$ is shown as a red circle.

Therefore, regarding the distance to the source R as a fixed parameter and varying the observational angle ϑ, L is a Gaussian along the blue circle in figure 2.11.

Since the interest is in the angular distribution of L, plotting it against ϑ shows a Gaussian only for small angles and a deviation of that shape for bigger angles. In figure 2.12, L (colored lines) is plotted against ϑ together with Gaussians in θ(black lines) and one can see that the difference plays a role for large angles depending on the electrons' energies.
Consequently, the deviation from a Gaussian in the observational angle grows more pronounced with greater distances to the object.

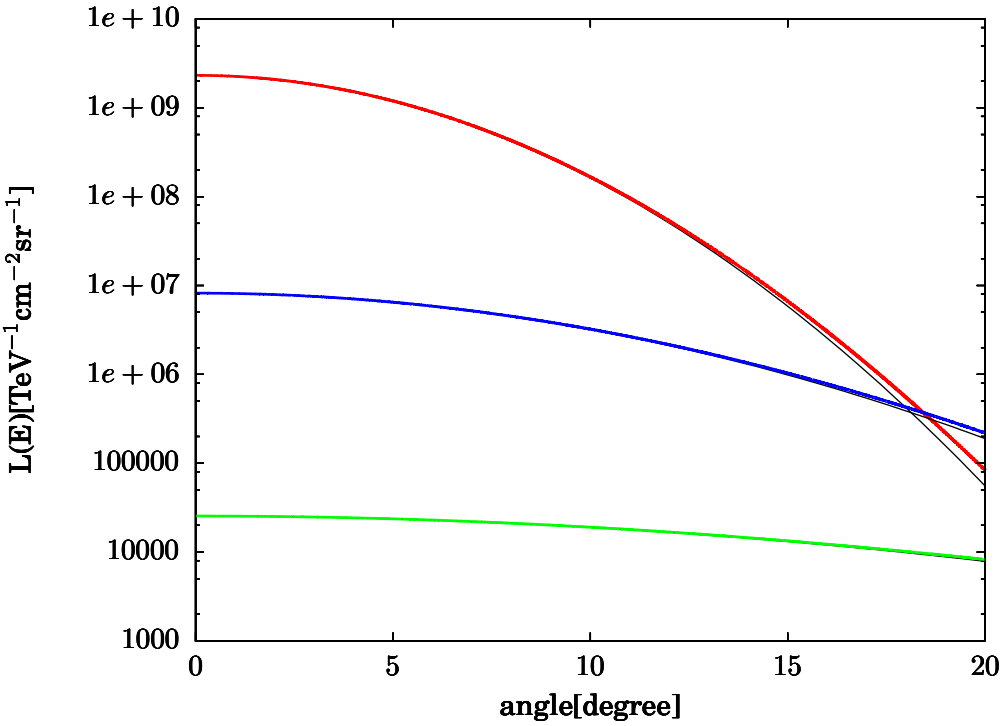

Figure 2.12: Line-of-sight integral in the burst-like injection scenario as a function of angle for different electron energies. Red: 0.01 TeV, blue: 0.1 TeV, green: 1 TeV. The black curves are Gaussians. The object is 25000 years old, $\delta = 0.5$, $\alpha = 2$, $E_g = 10^{48}$ erg, $r = 1$ kpc.

The colored curves in figure 2.12 become broader with increasing energy. This is because the higher the energy of the electrons is, the wider the Gaussians are that describe the according electron densities over which the integration is performed. As a result, the object appears increasingly large with the electrons' energy, much like in figure 2.4. Given the parameters in figure 2.12, the angular distance where the line-of-sight-integral has dropped to $L(R, t, \vartheta = 0, E)/\mathrm{e}$ would be 18.47 degrees. Since L inherits the electron densities' properties, a very different behaviour is expected for the continuous injection scenario.

Continuous-Injection scenario

Again, electrons in the continuous injection scenario show a quite different spectral and spatial behaviour than in the burst-like injection scenario. Figure 2.13 shows the spectrum of the line-of-sight integral.

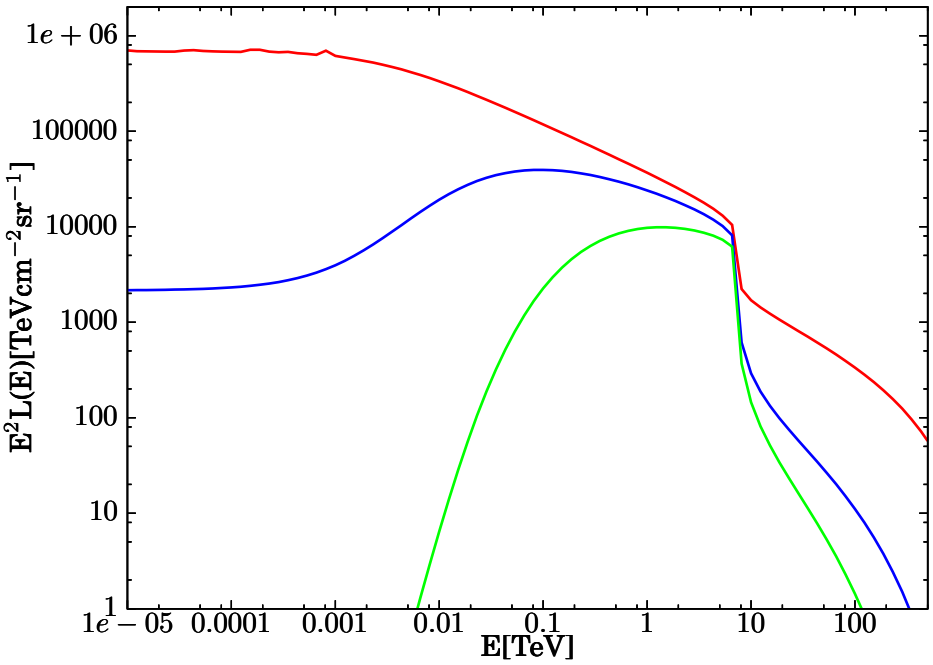

Figure 2.13: Line-of-sight integral in the continuous injection scenario as a function of energy at different angles. Red: 0 degrees, blue: 5 degrees, green: 10 degrees. The object is 25000 years old, $\tau^* =$ 250 a, $\delta = 0.5$, $\alpha = 2$, $E_g = 10^{48}$ erg, $r = 1$ kpc.

The spectrum exhibits a step above the maximal cut-off energy rather than a cut-off, as in the case of burst-like injection.
The shape of the spectrum above E_{max} varies with the observational angle. This is because these high-energy electrons are closely distributed around the source due to their rapid radiative cooling. With higher electron energies, this distribution gets sharper. Thus, integration along a line-of-sight next to the center misses these high energetic electrons which are very narrowly localized around the source and as a result, increasing the observational angle causes a drop at the highest energies in the spectrum.
The behaviour at $E < E_{\mathrm{max}}$ is analogue to the one in the burst-like scenario since the contribution to the integral by continuous injection in this energy range is negligible. The spectral properties in this energy range are determined by the big majority of electrons, namely those ejected by the pulsar in the first few hundred years of its life which is, assuming the parameters used in fig-

ure 2.13, almost instantaneous compared to the timescale of the object's age. Additionally, the electron densities get weighted in the integral with r^{-2}, leading to a much larger contribution of electrons located near the observer to the line-of sight integral L while on the other hand recently ejected electrons are located at the source distance R, which is usually in the kiloparsec range. Furthermore, because of the sharp localisation at the source the integration over those electrons is only over a very small radial interval, resulting in a further decrease of the contribution to the integral due to recently ejected electrons. Hence, the temporal evolution of the object for the object's spectral properties in this energy range is of low importance.

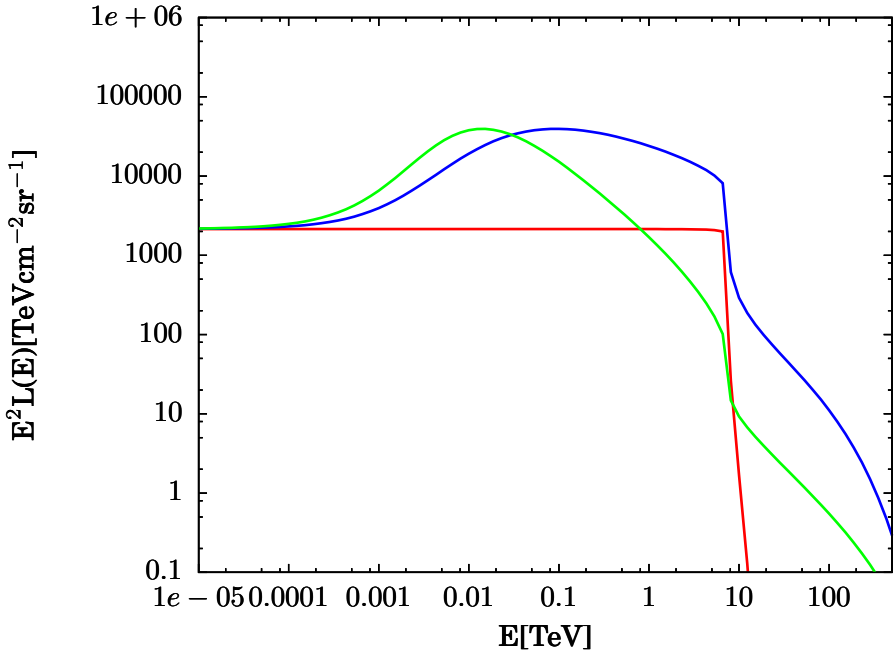

Figure 2.14: Line-of-sight integral in the continuous injection scenario for different values of δ. Red: $\delta = 0$, blue: $\delta = 0.5$, green: $\delta = 1$. The object is 25000 years old, $\tau^* = 250$ a, $\delta = 0.5$, $\alpha = 2$, $E_g = 10^{48}$ erg, $r = 1$ kpc.

Figure 2.14 shows the energy spectrum of the line of sight integral for different energy dependencies of the diffusion coefficient at an observational angle of 5 degrees. Because the temporal evolution plays only a minor role for energies below the cut off, the spectral behaviour at these energies can be explained just like in the burst-like injection case.
Because of continuous injection there are electrons at $E > E_{\max}$ and their spectrum also shows a strong dependence on the parameters δ. For energy independent diffusion i.e. $\delta = 0$ (red line in figure 2.14), electrons at high energies

don't diffuse faster and do not reach the integrational points to a large extent. This changes with increasing energy dependence of the diffusion (green and blue lines in figure 2.14) and there is a significant electron population at that energies who's spectral index decreases with an increasing value of δ.

Looking at the angular characteristics of the line-of-sight integral in the continuous injection scenario (figure 2.15) reveals a very different picture compared to the burst-like case.

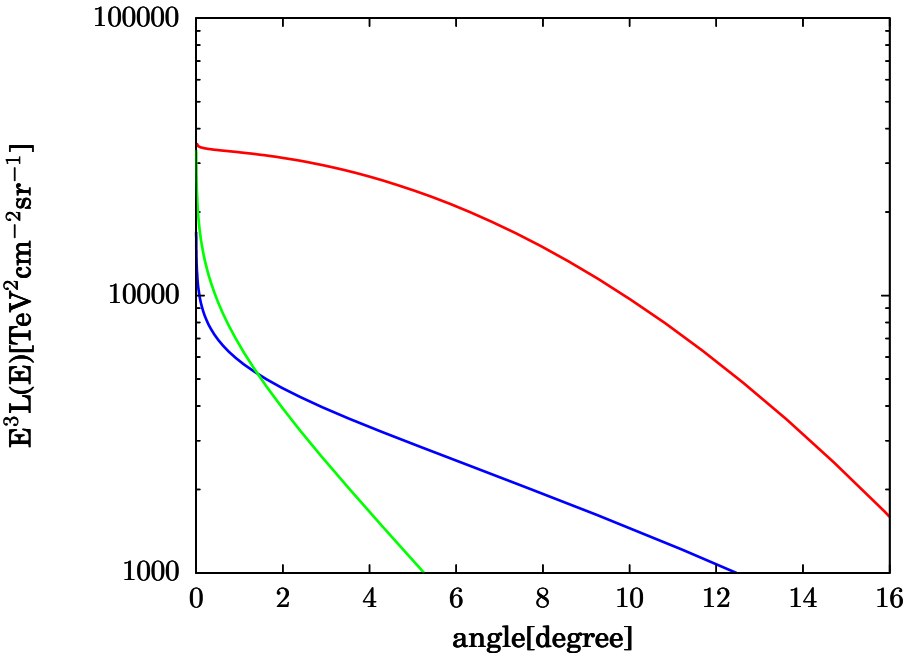

Figure 2.15: Line-of-sight integral in the continuous injection scenario as a function of angle for different electron energies. Red: 1 TeV, blue: 10 TeV, green: 100 TeV. The object is 25000 years old, $\tau^* = 250$ a, $\delta = 0.5$, $\alpha = 2$, $E_g = 10^{48}$ erg, $r = 1$ kpc.

First of all, there are electrons at energies above the cut-off energy of the burst like case (green and blue lines in figure 2.15). These electrons in terms of angular distribution behave in an opposite way to what is expected in general for the burst-like injection.
Their angular width decreases with increasing energy. This is because electrons at these energies are cooled down rapidly so that they have to be of recent origin and thus do not reach large travel distances. Because the cooling rate is increasing with the square of the electrons' energies, this trend increases with higher energies resulting in ever sharper peaks centered at the source.
However, the line-of-sight integral over electrons with energies below the cut-

off energy shows very different properties. Because the electron population at these energies consists mainly of the bulk of electrons ejected at the early stages of the pulsar's evolution, the dominant feature in its angular distribution is a Gaussian shape, just like for burst-like injection. Additionally and just like expected, there is a superimposed peak centered at the source caused by young electrons, just like in figure 2.7. This peak, however, is diminutive compared to the one in figure 2.7. The reasons for that are again the weighting of electron density with r^{-2} and the small spatial extension of the electron population recently ejected by the pulsar.
In the framework of this model, the assumption of continuous injection is required in order to explain observed features of Pulsar Wind Nebulae such as an angular radius that has the order of magnitude of 0.1 degrees or the appearance of these objects at energies $\gtrsim$ 10 TeV at all.

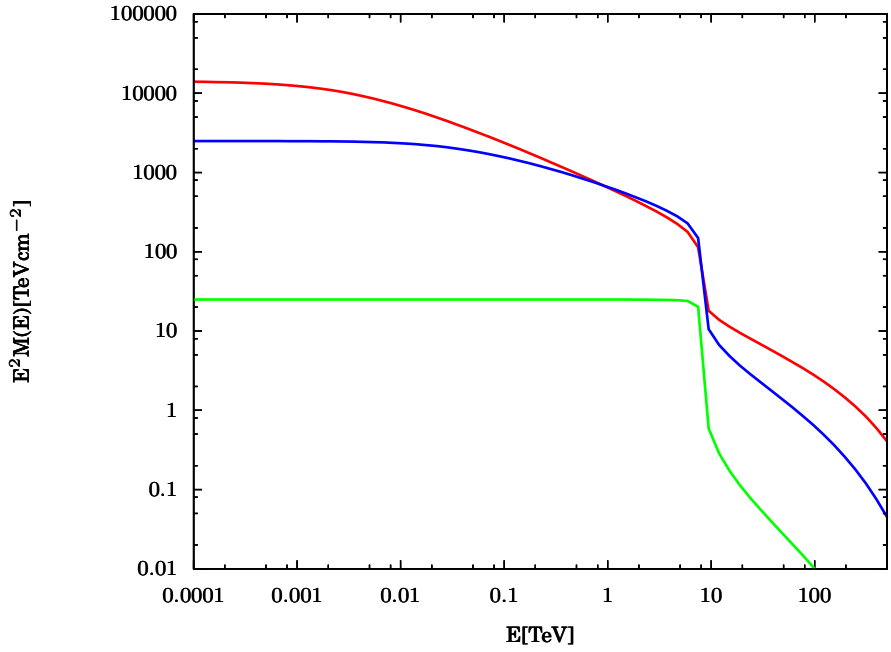

Figure 2.16: Line-of-sight integral in the continuous injection scenario integrated over an opening angle of 5 degrees as a function of energy for different object distances. Red: 100 pc, blue: 1 kpc, green: 10 kpc. The object is 25000 years old, $\tau^* = 250$ a, $\delta = 0.5$, $\alpha = 2$, $E_g = 10^{48}$ erg.

To get a total spectral gamma-ray flux rather than an angular one, it is necessary to integrate over a solid angle. The result is shown in figure 2.16. As one can see, the spectra differ much for different distances to the source. This is because at close distance to the object, it is impossible to see the whole nebula at

energies $E \lesssim E_{max}$ since the more energetic and hence faster diffusing electrons have diffused out of the field of view to a larger extend than it is the case for electrons at lower energies or those above the cut-off energy. The consequence is a drop in the spectrum at $E \lesssim E_{max}$, which can be seen with the red line in figure 2.16. Increasing the source distance reduces this effect until almost all electrons are in the field of view and as a result, the original injection spectrum, except for electrons with $E \gtrsim E_{max}$, is obtained (green line). Thus, the integrational angle has a large impact on the spectral properties of the emitted gamma rays.
Another property of the solid angle integral is that the weighing with $\propto r^{-2}$ is visible in the normalization. Comparing the blue and green lines in figure 2.16 shows that increasing the distance to the source by the order of one magnitude reduces the normalization by two orders of magnitude as it is expected.

2.2.3 From Electrons To Gammas

At this point, the electron density at every location in the PWN has been derived and from that the line-of-sight integral L (see equation (2.26)).
As final result the gamma-ray flux, as seen by an observer at a distance R to the electron source, is desired. To that end, one final step has to be made, namely the folding of L with the emissivities $(dN_i/dEdt)$ as it was shown in equation (2.25):

$$\frac{dN_\gamma}{dEdAd\Omega dt} = \int_{E_{e,min}}^{E_{e,max}} dE_e \left[\frac{dN_{\mathrm{Sy}}}{dEdt} L(E_e, R, \vartheta, t) + \sum_{i=1}^{3} \int d\epsilon_i \frac{dN_{IC,\epsilon_i}}{dEdt} L(E_e, R, \vartheta, t) \right]. \tag{2.30}$$

The result is, as already mentioned, a gamma-ray flux per solid angle. In order to get the gamma-ray flux emitted out of an solid angle element $\Delta\Omega$, the integral M (see equation (2.29)) instead of L has to be inserted in integration (2.30).

The four integrands in integration (2.30) account for synchrotron radiation and inverse Compton scattering with the three different target photon fields (the CMB, the ambient infrared and the ambient optical photon field) respectively. In this model, they are integrated separately.

In the following, the components of integration (2.30) will be discussed and their results will be presented.

IC-Radiation

According to equation (2.30), the gamma-ray flux due to inverse Compton scattering is given by

$$\Phi_{IC}(E) \equiv \frac{dN_\gamma^{IC}}{dEdAd\Omega dt} = \int_{E_{e,min}}^{E_{e,max}} dE_e \sum_{i=1}^{3} \int d\epsilon_i \frac{dN_{IC,\epsilon_i}}{dEdt} L(E_e, R, \vartheta, t). \tag{2.31}$$

The emissivity $(dN_{IC,\epsilon_i}/dEdt)$ has been derived in chapter two (see equation (1.17)). At this point it is important to mention that this emissivity is valid for the Thomson as well as the Klein-Nishina regime. However, this is not the case for the total electron energy loss rate due to inverse Compton radiation that is assumed in this model, which is only valid in the Thomson regime. To generalize the loss rate so that it is also correct in the Klein-Nishina regime could be a topic of future work. This will be discussed in chapter four.

If the scattering electrons are distributed according to a power law with a spectral index of α, an analytical result can be obtained. In this case the gamma-ray spectrum again is a power law with spectral index $\gamma = (\alpha + 1)/2$ for energies $E \lesssim E_{IC,max}$, where $E_{IC,max}$ is the upper end of the IC-spectrum which is determined by the maximal energy of scattering electrons. Beyond that the spectrum describes a drop similar to an exponential cut-off.
Since in this model the electrons producing inverse-compton radiation are not distributed in a power-law manner, the integral has to be calculated numerically.
The result of the integration is plotted in figure 2.17.

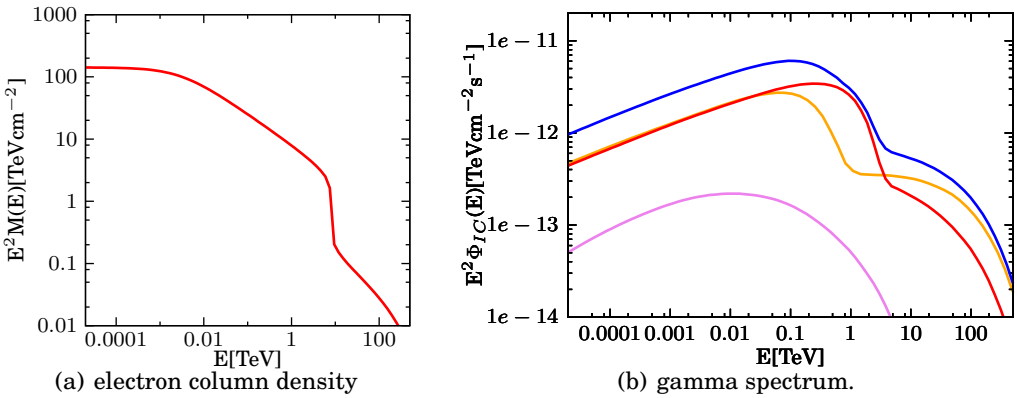

(a) electron column density

(b) gamma spectrum.

Figure 2.17: Line-of-sight integral integrated over an opening angle of 0.5 degrees and resulting IC gamma spectrum. The object is 25000 years old, $\tau^* = 250$ a, $\delta = 0.5$, $\alpha = 2$, $E_g = 10^{48}$ erg, $r = 1$ kpc.

The left panel shows the column density of the electrons within a opening angle of 0.5 degrees. On the right the inverse-compton spectrum is shown. The blue line is the total gamma-flux produced by inverse compton scattering with the three considered radiation fields: the cosmic microwave background (CMB), the infrared field produced by reflection of starlight on dust particles and the photon field in the optical range which has its origin in the light emitted by stars of the spectral classes G-K.
Additionally the single contributions of IC-radiation by each of the photon fields is displayed. The orange line in figure 2.17 shows the contribution to the spectrum by the CMB, the red line is the infrared part and finally the violet one is the IC-spectrum of interaction with the optical field.

Photons within a certain energy interval [E', $E' + dE'$] are produced by electrons of higher energy. The photon density at that energy is thus the superposition of gamma-rays emitted into dE' by all the electrons above that energy. Therefore, the gamma-ray spectrum shows a superposition of the electrons' spectral features with $E_{\mathrm{el}} > E$.
The inverse compton spectra show a power-law behaviour at lower energies followed by a step-like feature after which they drop down exponentially. The step-like feature is caused by the step in the electron spectrum above which there are only recently ejected electrons. Below the step in the gamma-ray spectrum there is a $E^2\Phi \propto E^{0.25}$ spectral behaviour which is corresponding to a spectral index of the gamma-rays of $\gamma = 1.75$. This part of the spectrum is caused by the electrons $E \lesssim E_{max}$, where their spectrum resembles a power law with a spectral index of $\alpha = 2.5$. Hence, the analytical expectations for the corresponding interval in the gamma-ray spectrum are fulfilled since $\gamma = (\alpha + 1)/2 = 1.75$, as already mentioned.
The spectral position of the step in the gamma spectra varies with the target photons' energy. Lower energy photon fields lead to a lower position of the step. This is because for a given electron energy the domain of the scattering is determined by the energy of the target photon (see section 1.2.1). For a lower energy photon field, electrons enter the Klein-Nishina regime at higher energies and vice versa. Because in the Klein-Nishina limit the electrons lose a great fraction of their energy to the target photon, the photons' energies become increasingly similar to the electrons' energies while approaching the Klein-Nishina limit. As a result the features in the injected electron spectrum and the gamma spectrum increasingly coincide in their spectral position while approaching the Klein-Nishina limit. For that reason the step in the inverse Compton spectrum due to scattering with the ambient infrared target photon field is closer to the one in the electron spectrum than it is the case for the step in the inverse Compton spectrum obtained by scattering with CMB-photons. The superposition of the spectrally different located steps leads to a more complex structure of the total inverse Compton spectrum compared to the electron spectrum, where there is only one step at energy E_{max}.

Also the angular behaviour of the gamma-ray flux is determined by the electron column density. Figure 2.18 shows the angular distribution of the inverse-Compton gamma-ray flux.

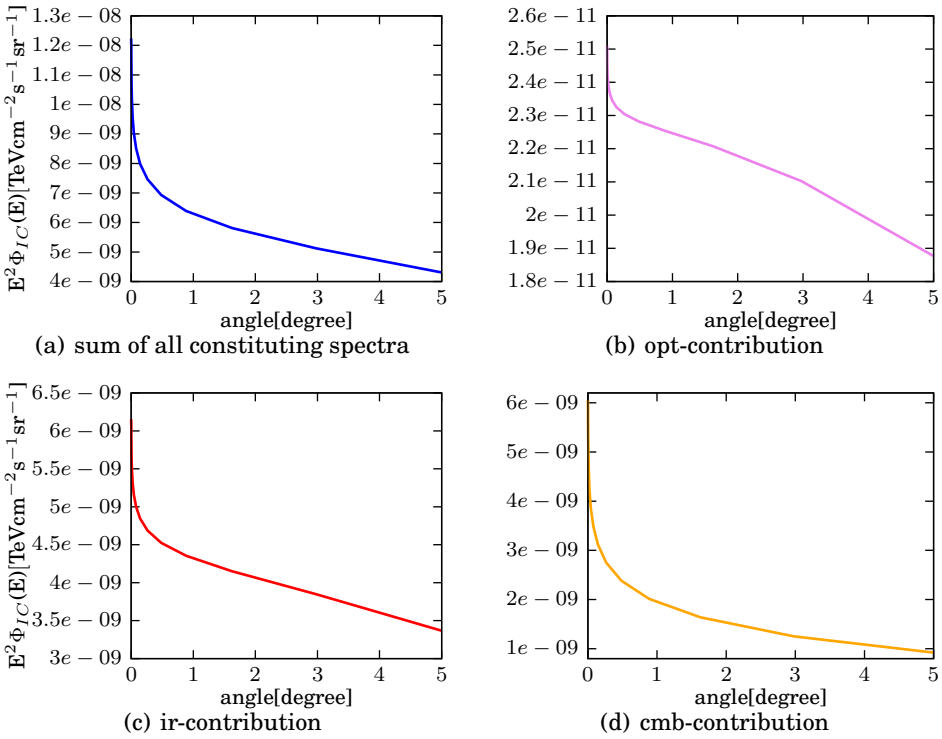

Figure 2.18: Gamma-ray emission due to inverse Compton scattering as a function of angle. The object is 25000 years old, $E = 1$ TeV, $\tau^* = 250$ a, $\delta = 0.5$, $\alpha = 2$, $E_g = 10^{48}$ erg, $r = 1$ kpc.

Panel (a) in figure 2.18 shows the total gamma-ray flux, i.e. the sum of emission from all three assumed radiation fields. Panels (b)-(d) show the single contributions from inverse Compton scattering with the different radiation fields. One can see that their angular shapes differ. This is because the gamma-ray flux at a given energy, as already pointed out, inherits the features of electron column densities above that energy. Since an energy of 1 TeV in the gamma-ray spectrum for scattering with CMB-photons is well above the step-like feature in that spectrum and photons in this spectral range are originated by electrons that are themselves above the step-like feature in the electron spectrum, the angular properties of the gamma-ray flux at 1 TeV are similar to those of their "parent" electrons: the gamma ray flux is peaked at the source. The same holds for the infrared and optical target field contributions, although one can see that there is a strong Gauss-like shape for the emission by the optical field caused by electrons with a spectral position that is not above the step in the electron

spectrum. A faint Gauss-like component in the angular distribution may be observed in the infra-red contribution as well.
Altogether it can be said that the spectral and angular properties of the IC-gamma-ray flux show a more complex behaviour than the ones for the electron column density. On the one hand, this is because the photon flux is a composition of three different contributions and on the other hand because the gamma-ray flux for each contributing radiation field at a given energy resembles the integrated electron features, weighted with the Klein-Nishina cross section.

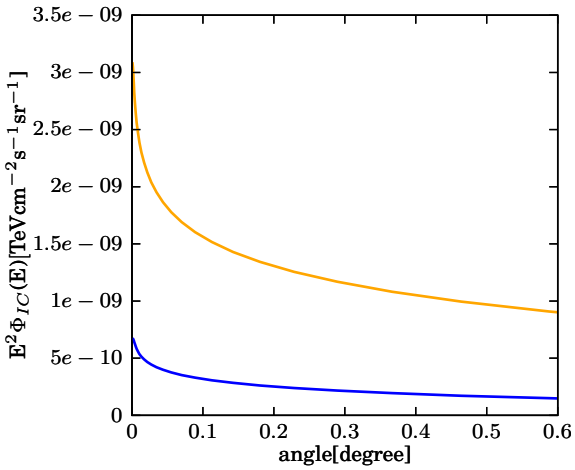

Figure 2.19: Gamma-ray emission as a function of angle, sum of all constituting spectra. Orange: $E_\gamma = 100$ TeV, blue: $E_\gamma = 10$ TeV. The object is 25000 years old, $\tau^* = 250$ a, $\delta = 0.5$, $\alpha = 2$, $E_g = 10^{48}$ erg, $r = 1$ kpc.

Figure 2.21 displays the angular distribution of the total inverse Compton gamma-ray flux at different energies. With increasing energy the peak at the source gets more pronounced. This is the same behaviour as for the electron column density. However, in general the peak in the gamma-ray spectrum has a different, more narrow shape since it is a integration over electron densities starting at the photon's energy up to the highest electron energies. This means it is an integration over increasingly steep angular electron distributions.
The angular distance, where the flux has dropped to $1/e$ of the value at the source for the shown model object is around 0.1 degrees for photons in the energy range of interest.

Synchrotron Radiation

Looking at equation (2.30) points out that the photon flux due to synchrotron radiation is given by

$$\Phi_{synch}(E) \equiv \frac{dN_\gamma^{synch}}{dEdAd\Omega dt} = \int_{E_{e,min}}^{E_{e,max}} dE_e \frac{dN_{synch}}{dEdt} L(E_e, R, \vartheta, t). \tag{2.32}$$

For the emissivity $(dN_{synch}/dEdt)$ expression (1.27) is used (see chapter two). Performing integration (2.32) yields the synchrotron flux per solid angle. Replacing L (see equation (2.26)) by M (see equation (2.29)) in the integration leads to the synchrotron emission out of an solid angle element $\Delta\Omega$. This is plotted in figure 2.20.

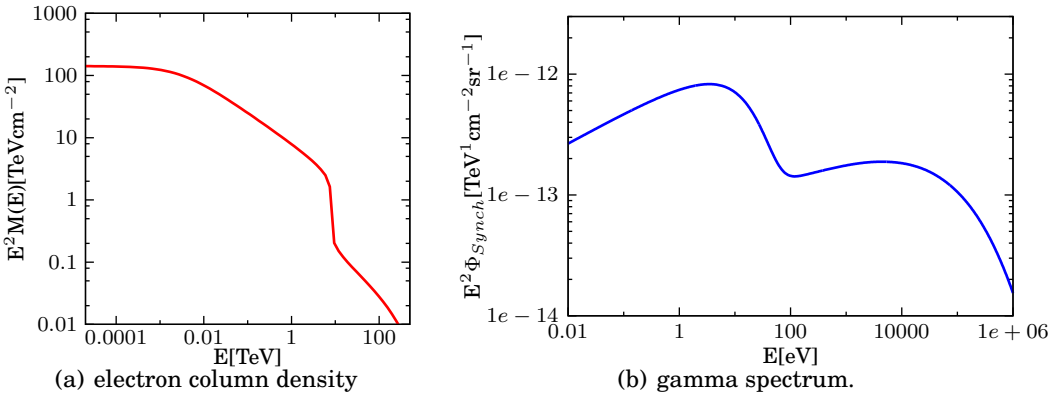

(a) electron column density (b) gamma spectrum.

Figure 2.20: Line-of-sight integral for a continuous injection scenario integrated over an opening angle of 0.5 degrees and resulting synchrotron spectrum. The object is 25000 years old, $\delta = 0.5$, $\alpha = 2$, $E_g = 10^{48}$ erg, $\tau^* = 250$ a, $r = 1$ kpc, $B = 5$ μG.

Panel a shows the electron column density, panel b the resulting synchrotron spectrum. Its shape shows much similarity to the inverse Compton gamma-ray spectra. There again is a step in the spectrum caused by a step in the electron spectrum. Beyond that step it rises and eventually declines due to the exponential cut-off in the electron spectrum.
Because the functional energy dependence of synchrotron-radiation relates to the initial electron distribution in the same way the inverse Compton radiation does, the spectrum at energies below the step is a power law with a spectral index of 0.25. This is analogue to the inverse Compton case and has already been explained. The synchrotron flux above the step is, like in the case of inverse Compton scattering, caused by electrons ejected after the pulsar's creation.
Like the synchrotron spectrum also the angular distribution shows a great similarity to the corresponding distribution of the IC-gamma flux. This is presented

in figure 2.21.

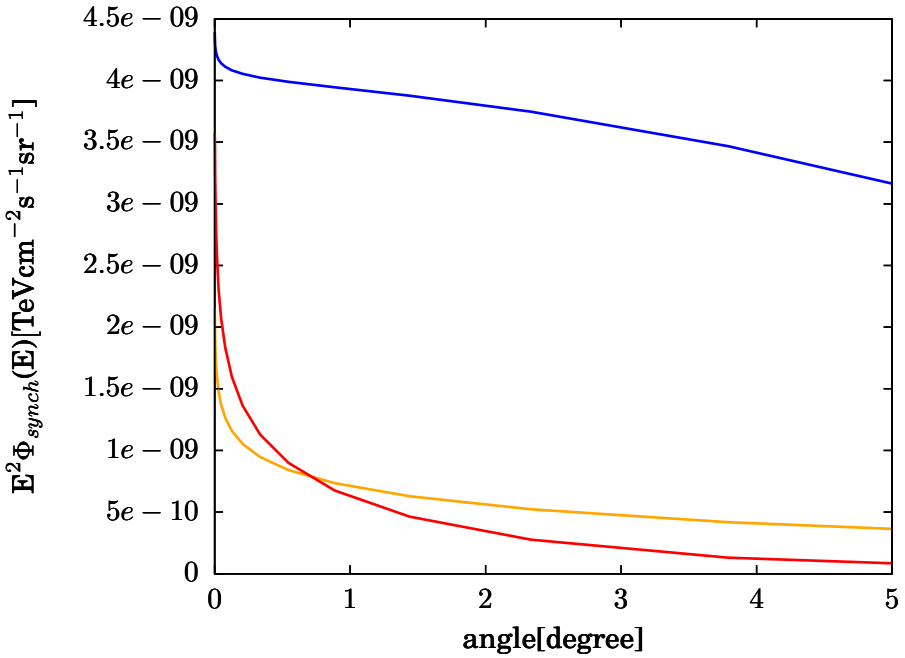

Figure 2.21: Synchrotron flux as function of angle. Blue: $E_{Synch} = 1$ eV, yellow: $E_{Synch} = 10^2$ eV, red: $E_{Synch} = 10^4$ eV. The object is 25000 years old, $\delta = 0.5$, $\alpha = 2$, $E_g = 10^{48}$ erg, $\tau^* = 250$ a, $r = 1$ kpc.

Again, the angular distribution of photons with energies smaller than that of the steps position shows a Gaussoid behaviour with a superimposed peak. The peak is caused by integration over electron column densities at energies $E \gtrsim E_{max}$,which themselves show a angular distribution that is peaked at the source position. The Gaussoid contribution is due to integration over electron column densities below the step, which show a broad, Gauss-like angular behaviour, as explained earlier.

2.3 Application: Geminga

In this section the presented model will be applied to an actual astrophysical object: The nearby Geminga PWN.
Although Geminga is the first pulsar to be observed in gamma-ray light, it is still an object of interest. Until the discovery of 20 TeV gamma radiation from a region about 3° around the pulsar's assumed position by Milagro there was no evidence of the existence of a pulsar wind nebula. If there indeed is one, its close proximity of several hundred parsecs would provide a unique opportunity to understand this class of VHE astrophysical objects. Additionally, its high age of $t_{age} \gtrsim 300000$ years would possibly offer a insight in the temporal evolution of pulsar wind nebulae.
In the framework of this simple diffusion model a spectrum can be provided as well as an estimation of the objects spatial extension.
Table 2.1 lists the parameters given to the program.

Table 2.1: Model Parameters

PARAMETER	VALUE	DESCRIPTION
E_g	$2(5,5) \times 10^{48}$ ergs	total spin-down energy in electrons
κ	2	magnetic braking index
τ^*	250(250,1000) a	characteristic spin-down time
t_{age}	3×10^5 a	pulsar's age
d	$2(3,2) \times 10^2$ pc	distance to the pulsar
α	2	spectral index of injected electrons
E_{cut}	500 TeV	exp. cut-off energy in injection spectrum
D_0	$4.149 \times 10^{27}\mathrm{cm}^2\mathrm{s}^{-1}$	normalization of the diffusion coefficient
E^*	3×10^{-3} TeV	energy scale of the diffusion coefficient
δ	0.6	energy dependence of diffusion
B_{ISM}	5 μG	interstellar magnetic field strength
W_{CMB}	0.25 eVcm^{-3}	energy density of the CMB
W_{IR}	0.4 eVcm^{-3}	energy density of the ambient IR field
W_{OPT}	0.3 eVcm^{-3}	energy density of the ambient opt. field
T_{CMB}	2.725 K	temperature of the CMB
T_{IR}	20 K	temperature of the ambient IR field
T_{OPT}	5000 K	temperature of the ambient optical field

Three scenarios for the Geminga pulsar are assumed, varying in the total spin-down energy, the characteristic spin-down time and the distance to the pulsar (values are given in brackets). They shall be called scenarios (a), (b) and (c).

In figure 2.22 the energy spectra for the three different scenarios are shown.

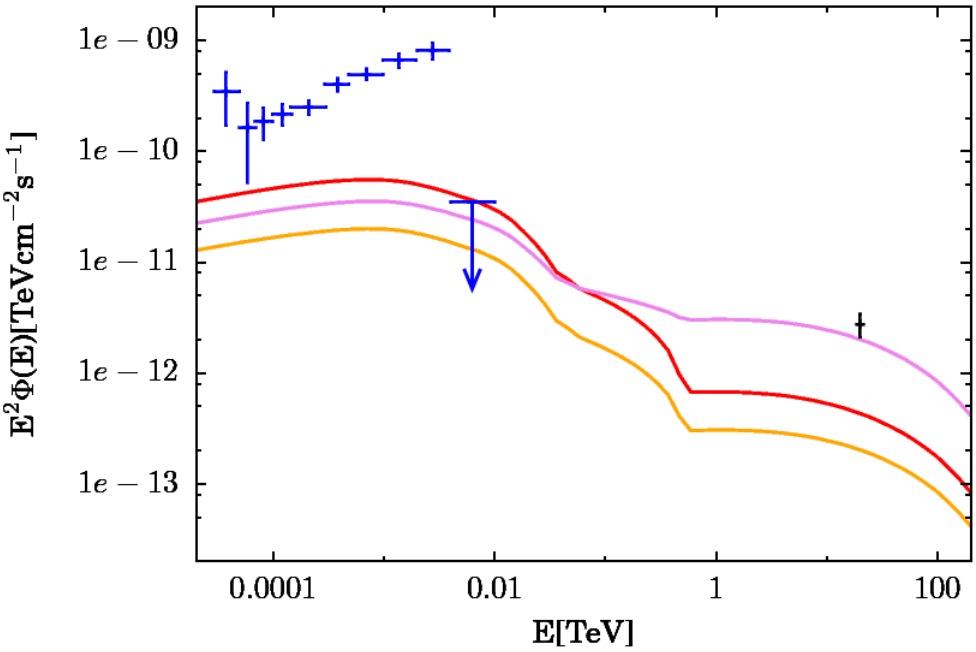

Figure 2.22: Geminga's gamma-ray spectra for the three different scenarios integrated over an opening angle of 5°. Orange line: scenario (a), red line: scenario (b), violet line: scenario (c). EGRET measurements are denoted by blue points, the black point is the flux at ∼20 TeV as measured by Milagro.

Comparing the spectrum corresponding to scenario (b) with the one corresponding to (a), one can see that increasing the total energy output in electrons (E_g) results in a general rise of the flux intensity. On the other hand, as one can observe by comparing the spectra belonging to scenarios (b) and (c), increasing the characteristic timescale of the pulsar's spin-down (τ^*) causes a decline in the flux at low energies and a rise at high ones, leading to a flatter spectrum. Milagro measured a flux at 20 TeV of $E^2\Phi = 2.76 \pm 0.68 \times 10^{-12}$ TeVcm^{-2}s^{-1} (black cross in figure 2.22), under the assumption that the gamma-ray spectrum above 20 TeV follows a power law with an spectral of $\alpha = 2.3$ [1]. Thus, since the presented model does not produce a power law as gamma-ray spectrum, a comparison with this measurement has to be taken with a pinch of salt. However, this flux value can be reproduced by this model using physically meaningful parameters (for example scenario (c)). As a matter of fact the assumption of continuous injection is needed to obtain a flux at energies this high because due to the high age of the object, in the case of burst-like injection the energy cut-off caused by radiative cooling of the electrons would be well below 1 TeV so that there would be no electrons with sufficient energy to produce gamma-rays at 20

TeV.
Furthermore, measurements taken with the EGRET instrument are featured in figure 2.22 [19]. Below ∼4 GeV the measured flux is higher than the model's results. This, however, is expected since in this energy range the pulsar itself emits gamma radiation (see section 1.1) and is much brighter than the PWN. The pulsar's emission is cut off at higher energies, and the upper limit at 6.3 GeV seems to fit the model's results well.

Looking at the angular distribution of VHE-gamma radiation at 20 TeV shows that the object is very extended (see figure 2.23). The angular distance where the flux has dropped to 1/e of the value at the source position is about 3 degrees, thus the modeled source extension is comparable to what the Milagro observation suggests [1].
Figure 2.23 shows the angular distribution of 20 TeV gamma-rays in the three different scenarios.

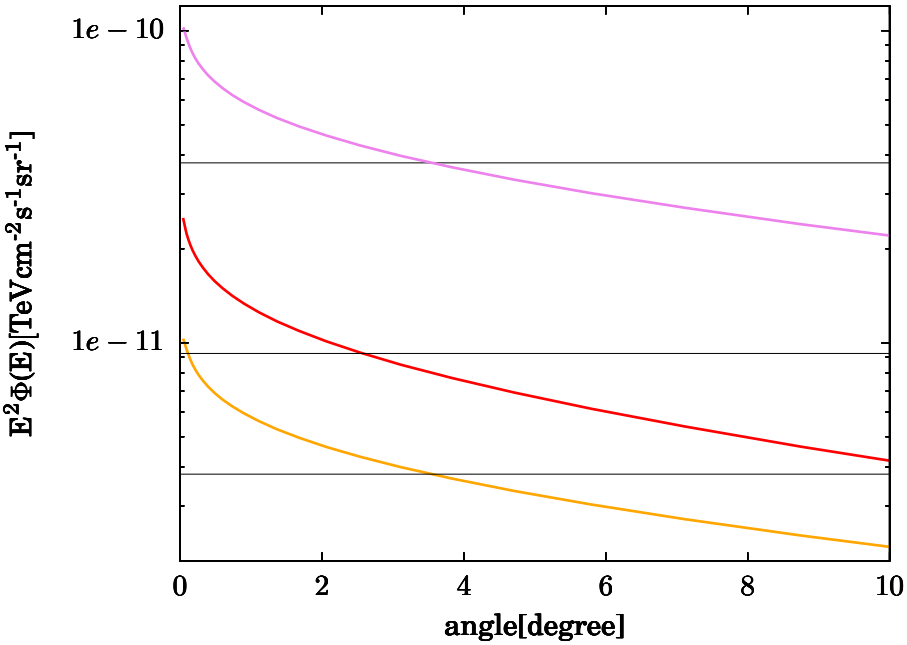

Figure 2.23: Modelled 20 TeV gamma radiation from the Geminga PWN plotted against the observational angle for the three scenarios: (a)-orange line, (b)-red line and (c)-violet line. The black lines indicate 1/e of the value at the center.

Increasing the characteristic spin-down timescale τ^* by a factor of 4 and the pulsar's energy output by a factor of 2.5, results in a rise in intensity of roughly one order of magnitude, as can be seen comparing scenarios (a) and (c). The

angular width, however, is not affected. In both scenario (a) and (c) the flux intensity drops to 1/e of its value at the source position at an angle of 3.55 degrees. In scenario (b) the distance to the object has been increased to from 200pc to 300 pc and as a result, compared to scenarios (a) and (c), the intensity drops with a factor of about 0.25 and the angular width decreases; the flux drops down to 1/e of the center value at an angle of 2.57 degrees.

As already mentioned, the H.E.S.S. experiment has a limited angular resolution that depends on the gamma-ray energy and the observational direction. In order to simulate the angular photon flux distribution as it would be observed with the H.E.S.S. instrument, the modelled angular flux distribution has to be blurred with that resolution.
Mathematically, this is done by folding the gamma-ray flux with a Gaussian of width $\sigma = \delta_\vartheta$:

$$\Phi(E,\vartheta)_{folded} = \int d\vartheta' \frac{1}{\sqrt{2\pi}\,\delta_\vartheta} \exp\left[-\frac{(\vartheta-\vartheta')^2}{2\,\delta_\vartheta^2}\right]\Phi(E,\vartheta'). \tag{2.33}$$

The result of this operation is shown in figure 2.24.

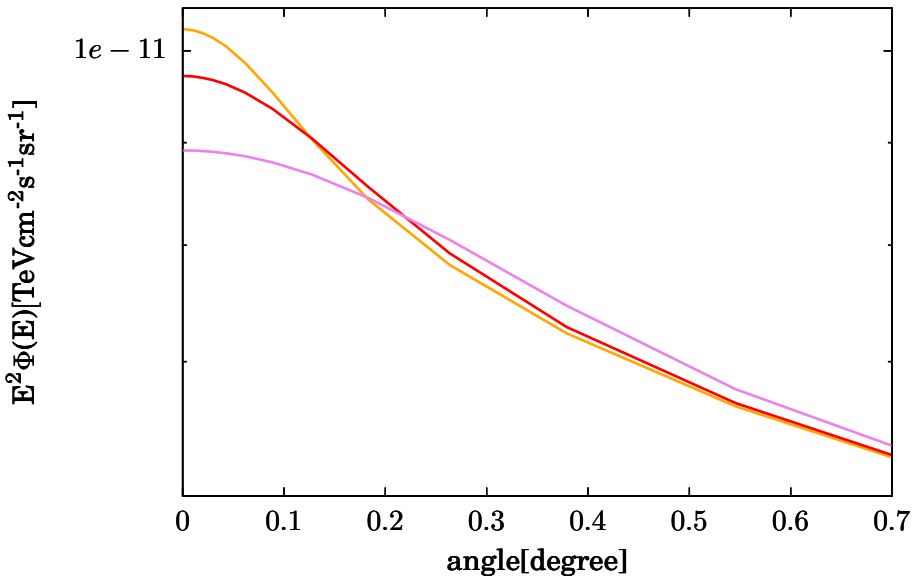

Figure 2.24: Modelled 20 TeV gamma radiation from the Geminga PWN plotted against the observational angle for scenario (a) after blurring with different angular resolutions δ_ϑ. Orange: $\delta_\vartheta = 0.05$ degrees, red: $\delta_\vartheta = 0.1$ degrees, violet: $\delta_\vartheta = 0.2$ degrees.

The blurring operation flattens and broadens the peak of the initial angular gamma-ray flux distribution, transforming it to a gauss-like feature near the source direction. At larger observational angles, the blurring shows little effect.

3 A Monte-Carlo Simulation Of Inverse Compton Scattering

In this chapter I present a simple Monte-Carlo simulation of the inverse Compton radiation processes occurring during the interaction of ultra-relativistic electrons with the cosmic microwave background.
The aim is to confirm analytical results for that physical process.

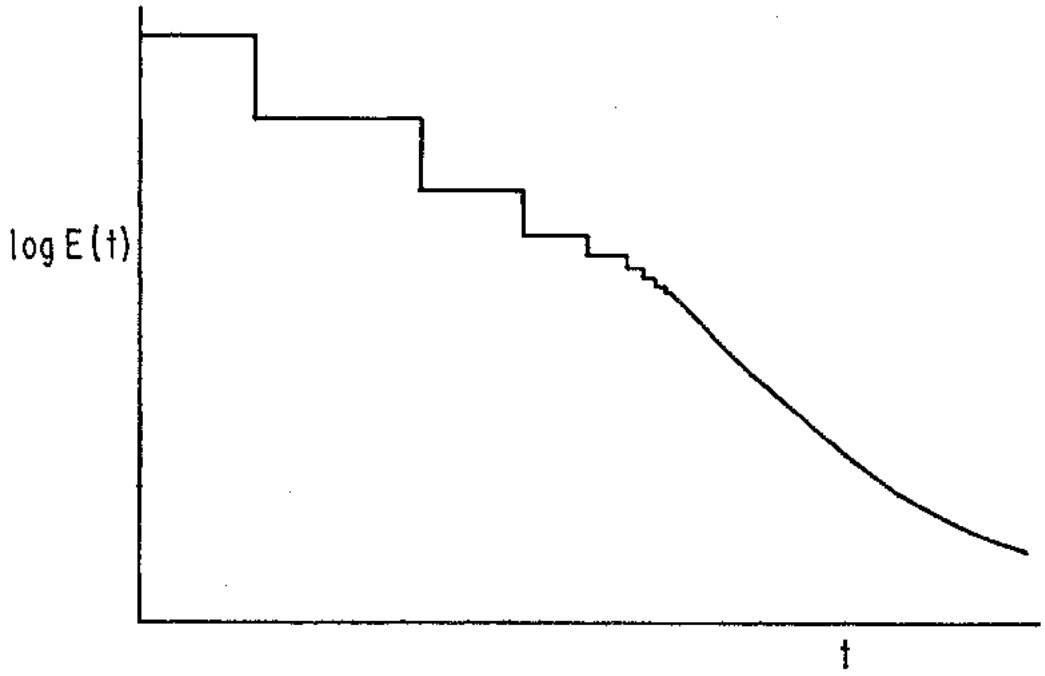

Figure 3.1: Sketch of a typical time evolution of an electron's energy due to losses by inverse Compton scattering (from Blumenthal and Gould [6])

Figure 3.1 outlines the temporal evolution of an electron's energy while undergoing inverse Compton scattering. This sketch assumes a sufficiently high injection energy of the electron so that the first few interactions may take place in the K-N regime. Radiating under these conditions, the electron loses discrete, sizable amounts of its original energy, resulting in the steps featured in figure 3.1. After several of these events it has lost so much of its initial energy,

that the scattering process continues in the Thomson limit, where only small fractions of the electron's energy get radiated away and the energy loss can be regarded as a continuous process. As a result, the curve smooths with increasing time.
With this work, analytical results obtained for this radiation process shall be verified, especially in the K-N regime, where the discontinuities in the temporal characteristics of the electrons' energies have to be accounted for that complicate the analytical procedure.
This chapter consists of four parts:

- In section 3.1 the analytical results will be presented as they were derived by Blumenthal and Gould, Kardashev and Modersi et al.
- Section 3.2 presents an overview over the sampling methods used in this simulation.
- The structure and idea of the program will be outlined in section 3.3.
- Finally, in section 3.4 the results obtained by the simulation will be presented and discussed.

3.1 The Analytical Results

Inverse Compton scattering shows very different properties, depending on the scattering regime. As a reminder, the criteria for the different regimes are given once more:

- The scattering occurs in the Thomson regime, if $\epsilon' \ll mc^2$, i.e. if in the electron's rest frame the target photon's energy is much smaller than the electron's rest energy. Alternatively one can use the criterion $\Gamma \equiv 4\epsilon E_e/(mc^2)^2 \ll 1$.
- The scattering occurs in the Klein-Nishina regime if $\epsilon' \gg mc^2$, i.e. if in the electron's rest frame the target photon's energy is much larger than the electron's rest energy. Alternatively this is the case if $\Gamma \gg 1$.

The transition between the two regimes is at $\Gamma \approx 1$ which corresponds to an energy $E_{KN} \approx (mc^2)^2/4\epsilon E_e$. For the CMB, this is at $E_{KN} \approx 100$ TeV.

In the following, the analytical results for electron and photon spectra in the different inverse Compton scattering regimes will be presented.

3.1.1 The Electron Spectrum

Results In The Thomson Regime

If electrons lose their energy due to inverse Compton scattering only in small fractions per collision, or to be more precise, if the fractional loss of energy in a time interval is much less than the number of scattering events during that time [6]

$$-\dot{E}/E \ll Nc\sigma, \tag{3.1}$$

the radiation process takes place in the Thomson regime and it is possible to describe the temporal evolution of the electrons' energy with the continuity equation in energy space [6]

$$\frac{\partial N}{\partial t} + \frac{\partial}{\partial E}(\dot{E}N) = Q(E, \mathbf{r}, t). \tag{3.2}$$

As was shown in chapter 2, in the Thomson limit the energy loss rate is $\dot{E} = -bE^2$, where b is a constant determined by the energy density of the target photon field. If a temporally constant power-law injection spectrum is assumed $Q(E, \mathbf{r}, t) = KE^{-\Gamma}$, equation (3.2) takes the form

$$\frac{\partial N}{\partial t} = b\frac{\partial}{\partial E}(E^2 N) + KE^{-\Gamma}. \tag{3.3}$$

Kardashev [16] derived a solution to that differential equation, using an initial value for the electron density $N(E, 0) = qE^{-(\Gamma+1)}$:

$$N(E,t) = qE^{-\Gamma}(1-btE)^{\Gamma-2} + \frac{KE^{\Gamma+1}}{b(\Gamma-1)}\left[1-(1-btE)^{\Gamma-1}\right]. \tag{3.4}$$

In his derivation, Kardashev assumes that there are no electrons present before the injection or in other words, he assumes the initial electron density to be zero $N(E,0) = 0 \Rightarrow q = 0$ and equation (3.4) becomes

$$\begin{aligned} N(E,t) &= \frac{KE^{\Gamma+1}}{b(\Gamma-1)}\left[1-(1-btE)^{\Gamma-1}\right] \\ &\approx \begin{cases} KtE^{-\Gamma} & \text{if } E \ll \frac{1}{bt} \\ \frac{KE^{-(\Gamma+1)}}{b(\Gamma-1)} & \text{if } E \gg \frac{1}{bt}. \end{cases} \end{aligned} \tag{3.5}$$

Thus, in the Thomson scattering regime it is expected that the cooled electron spectrum follows a broken power-law. Below an energy given by

$$E_{break} = \frac{1}{bt} \tag{3.6}$$

the original spectral index is expected and the spectral index of the cooled electrons is $\alpha = \Gamma$, above E_{break} the spectral index increases by unity, so that $\alpha = \Gamma + 1$.

In the case of burst-like injection there is no electron injection at times $t > 0$ and as a result, the source term in equation (3.3) is zero for that times. From a mathematical point of view, the differential equation

$$\frac{\partial N}{\partial t} = b\frac{\partial}{\partial E}(E^2 N) \tag{3.7}$$

has to be solved with the initial condition $N(E,0) = KE^{-\Gamma}$. Following Kardashev [16], the result is given by

$$N(E,t) = \begin{cases} KE^{-\Gamma}(1-btE)^{\Gamma-2} & \text{if } E < \frac{1}{bt} \\ 0 & \text{if } E > \frac{1}{bt}. \end{cases} \tag{3.8}$$

Therefore, the spectrum experiences a cut-off above the energy $E_{cut} = 1/(bt)$. At smaller energies, the behaviour differs strongly for different values of the spectral index Γ. In the special case $\Gamma = 2$, the bracket in equation (3.8) is unity and it follows that in this case at energies below the cut-off the initial spectral form is expected. For different values of the spectral index, the situation is quite different, which is shown in figure 3.26.

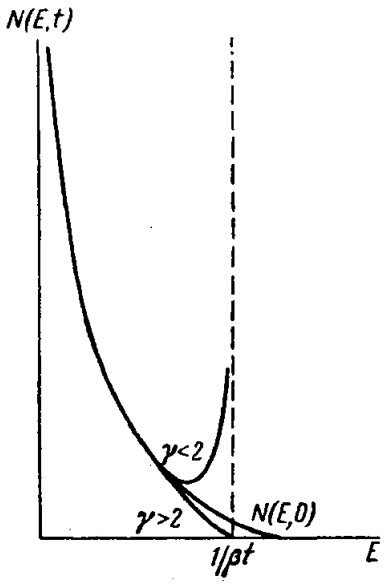

Figure 3.2: Electron spectrum after cooling by inverse Compton scattering in the Thomson limit. The quantity β corresponds to the constant b used in this work and γ corresponds to Γ in equation (3.8). This picture is taken from Kardashev [16].

For spectral indices $\Gamma > 2$ a drop in the spectrum below the cut-off energy E_{cut} is observed, whereas spectral indices of $\Gamma < 2$ lead to a pile-up at that energy.

Results In The Klein-Nishina Regime

The following derivation was conducted by Blumenthal and Gould [6].
In the deep K-N regime, characterized by the relation $\frac{4\epsilon_0 E}{m^2c^4} \gg 1$, condition (3.1) is not fulfilled and discontinuities have to be accounted for. In their approach, Blumenthal and Gold added integral terms to equation (4.2) that describe inverse Compton scattering in and out of an energy interval $[E, E + dE]$ due to discrete, large energy losses of the electrons:

$$\frac{\partial N(E,t)}{\partial t} + \frac{\partial}{\partial E}[\dot{E}N(E,t)] + N(E,t) \int_{mc^2}^{E} dE' P(E,E') - \int_{E}^{\infty} dE' N(E',t) P(E',E) = Q(E,\mathbf{r},t). \tag{3.9}$$

In the integrals the terms $P(E, E-\epsilon_1)$ are used. They are the probabilities that discrete, sizable energy losses leave an electron of initial energy E with an energy of $E - \epsilon_1$ after a time interval dt, where ϵ_1 is the energy of the upscattered photon. The first integral describes electrons leaving the considered energy interval by losing energy, while the second integral is the amount of electrons arriving in $[E, E + dE]$ from higher energies after losing energy during collisions.
Looking at the inverse Compton scattering in the Klein-Nishina limit, equation (3.9) has to be used. The authors assume steady-state conditions, which eliminates the first term on the left hand side in equation (3.9), and regard continuous energy losses as negligible compared to the large, discrete losses in the Klein Nishina regime so that the second term on the left hand side in equation (3.9) can be neglected. Together with an source term that is temporally constant and a power law in energy, these assumptions lead to the following integral equation:

$$N(E,t) \int_{mc^2}^{E} dE' P(E,E') - \int_{E}^{\infty} dE' N(E',t) P(E',E) = K E^{-\Gamma}. \tag{3.10}$$

The probability $P(E, E-\epsilon_1)$ is related to the inverse Compton photon spectrum per electron (1.17) by the integral

$$P(E, E-\epsilon_1) = \int_{U}^{\infty} d\epsilon \frac{dN_{\mathrm{IC}}}{dt\, d\epsilon\, d\epsilon_1}, \tag{3.11}$$

where ϵ is the target photon energy and U is the lowest target photon energy at which photons with energy ϵ_1 may be obtained. This value follows directly from

the kinematic boundaries (1.18).
If $dN_{\mathrm{IC}}/dtd\epsilon d\epsilon_1$ is interpreted as the probability that an electron of energy E scatters an CMB-photon of energy ϵ up to an energy ϵ' within an time interval dt, then the integral over all target photon energies (3.11) is the total probability of an electron with energy E to scatter a target photon of any energy up to the energy ϵ' within the time interval dt.
Two cases of target photon fields were investigated, a delta-distributed spectrum and a blackbody distribution.

In the first case, for a target photon spectrum $\rho(\epsilon) = \rho_0\delta(\epsilon-\epsilon_0)$, where ϵ_0 is the assumed photon energy, the result for the probability $P(E, E-\epsilon_1) \equiv P(E, E')$ is [6]

$$P(E,E') = \frac{3m^2c^5\rho_0\,\sigma_T}{8\epsilon_0}\times\left(\frac{E^2+E'^2}{E^3E'}+\frac{m^2c^4(E-E')}{4\epsilon_0E^4E'^2}\times(4EE'-E^2-E'^2)\right), \quad (3.12)$$

where m is the electron mass, c is the speed of light and σ_T is the Thomson cross section. With this expression and under the assumption that the result $N(E)$ is nearly a power law, the integral equation (3.10) can be solved and the result is

$$N(E) = \frac{8K\epsilon_0E^{-\Gamma+1}}{3m^2c^5\rho_0\,\sigma_T}\left(\ln\frac{4\epsilon_0E}{m^2c^4}-\frac{1}{2}-\frac{2\Gamma}{\Gamma^2-1}\right)^{-1}. \quad (3.13)$$

In the Klein-Nishina limit ($\frac{4\epsilon_0E}{m^2c^4} \gg 1$), the logarithmic term can assumed to be constant compared to the power-law dependency of the solution and the spectrum shows an energy dependence like $N(E) \propto E^{-\Gamma+1}$. This means, that the spectral index of the cooled electrons decreases by 1 compared to the injection spectrum, $\alpha = \Gamma - 1$.
Thus, the spectrum hardens again at energies corresponding to the Klein-Nishina regime. This can be understood as a consequence of a decreased inverse Compton cooling efficiency:
In the deep Klein-Nishina regime the inverse Compton cross section becomes smaller with increasing electron energy (see, for example [21]). As a result, the scattering rate and therefore the electron energy loss rate decreases for electrons at higher energies (this is the opposite case as in the Thomson regime, where the loss rate increases with the square of the electron energy). Hence, in the Klein-Nishina regime electrons at lower energies slide down the spectrum at a faster pace than their higher energetic counterparts, leaving them behind. This results in a rise in the spectrum.

The second case investigated by Blumenthal and Gould assumes a blackbody photon field $\rho(\epsilon) = [\pi^2(\hbar c)^3]^{-1}[\epsilon^2/(e^{\epsilon/\mathrm{k}T}-1)]$ for the target photons. To derive the electron spectrum, the double integrals over E' and ϵ in (3.10) have to be performed. The final result is

$$N(E) = \frac{16\hbar^2KE^{-\Gamma+1}}{m^2c^2(\mathrm{k}T)^2\,\sigma_T}\left(\ln\frac{4\mathrm{k}TE}{m^2c^4}+\frac{1}{2}-\frac{2\Gamma}{\Gamma^2-1}-C_E-C_l\right)^{-1}, \quad (3.14)$$

where the constants $C_E = 0.5772$ and$C_l = 0.5700$ are used.
Like in the previous case, since the mean target photon energy $\bar{\epsilon} \propto kT$, the logarithmic term can be regarded to be constant against the power-law part of the solution in the deep Klein-Nishina regime leading again to a spectral behaviour of $N(E) \propto E^{-\Gamma+1}$. Hence, also for a target photon field assumed to be blackbody-distributed, the initial electron spectrum's spectral index decreases by 1 due to inverse Compton scattering in the Klein-Nishina regime, so that the spectral index of the cooled electrons is $\alpha = \Gamma - 1$.

In a more recent work, Moderski et al. [20] among other things investigated the impact of inverse Compton scattering in the Klein-Nishima limit on the steady state electron energy distribution.
They included synchrotron losses in their considerations and defined a parameter $q \equiv w/U_B$, where w is the energy density of the target photon field and U_B is the energy density of an assumed magnetic field. Furthermore they formulated the total electron energy loss rate as $|\dot{E}| = [4c\sigma_T U_B/(3m^2c^4)]E^2(1 + qF_{\mathrm{KN}})$, where c is again the speed of light, σ_T the Thomson cross section and m is the electron rest mass. The quantity F_{KN} corresponds to the inverse Compton energy loss rate and has been approximated by the authors for different spectral ranges and target photon distributions.
Contrary to the derivations made by Blumenthal and Gould, Moderski et al. derived solutions for the electron spectrum in the Klein-Nishina regime using the continuity equation (3.2) rather than the exact integro-differential equation (3.10), arguing that the results obtained by the different equations are qualitatively very similar and that significant differences occur only if both the electron and the target photon distributions are mono-energetic.
For this work, the following conditions are important:

- $w \gg U_B = 0$, since no magnetic field has been assumed. This corresponds to the limit q $\gg 1$,
- a sharply distributed target photon field (this holds for both the blackbody and delta-distribution) and
- a power-law distributed electron injection spectrum.

Under these assumptions the authors found that at energies corresponding to the deep Klein-Nishina regime $E \gg E_{KN} = (mc^2)^2/4\epsilon E_e$ the spectral index α of the cooled electrons is given by

$$\alpha \simeq \Gamma - 0.5, \tag{3.15}$$

where Γ is the injected electrons' spectral index. Also this result corresponds to a hardening in the electron spectrum at the highest energies, although less pronounciated than in the solution proposed by Blumenthal and Gould (compare to equation (3.14)).

3.1.2 The Photon Spectrum

Blumenthal and Gould also derived analytical results for the photon spectrum emitted due to IC-scattering. Their considerations will now be shortly presented.

The total inverse Compton spectrum is obtained by the following integration:

$$\frac{dN_\Phi}{dtd\epsilon_1} = \iint d\epsilon dE N(E) \frac{dN_{\mathrm{IC}}}{dtd\epsilon d\epsilon_1}, \tag{3.16}$$

where again the inverse Compton photon spectrum per electron (1.17) is used. Assuming the electron spectrum to be a power-law $N(E) = LE^{-\alpha}$ within an energy interval $[E_{min}, E_{max}]$ and the target photons to be blackbody distributed, the integration can be performed analytically.
The two scattering domains, the Thomson and the Klein-Nishina domain, yield different result. In the Klein-Nishina domain the integration results in

$$\frac{dN_\gamma}{dtd\epsilon_1} = \frac{\sigma_T}{6\hbar^3 c^2} L (mc^2)^{\alpha+1} (kT)^2 \epsilon_1^{-(\alpha+1)} \times \left(\ln \frac{\epsilon_1 kT}{m^2 c^4} + 1 + C(\alpha) - C_E - C_l \right). \tag{3.17}$$

The parameters C_E and C_l from (3.14) are used. The quantity $C(\alpha)$ is a dimensionless parameter functionally depending on the spectral index α of the electron spectrum.
This expression holds only if the electrons' energy producing the gamma-rays is not near the endpoints E_{min} and E_{max} of the electron spectrum.
Equation (3.17) states, that in the Klein-Nishina regime electrons spectrally distributed like a power law with spectral index α produce a steeper photon spectrum distributed like a power-law with spectral index $\alpha + 1$.
In the Thomson limit, equation (3.16) yields

$$\frac{dN_\gamma}{dtd\epsilon_1} = \frac{3\sigma_T L}{8\hbar^3 c^2 \pi^2} (kT)^{(\alpha+5)/2} F(\alpha) \epsilon_1^{-(\alpha+1)/2}. \tag{3.18}$$

The target photon field is assumed to be black-body distributed and $F(\alpha)$ is a dimensionless parameter that is a function of the electrons' spectral index α.
This result states that inverse Compton scattering in the Thomson regime results in a photon spectrum that is a power law with the spectral index $\gamma = (\alpha + 1)/2$, where α is the electrons' spectral index. In this regime, the resulting photon spectrum is harder than the electron spectrum (provided $\alpha > 1$).

3.2 Obtaining The Right Random Numbers

Since a Monte-Carlo simulation is a stochastic simulation, random numbers are required. These random numbers have to follow the desired number distribution, for example a probability distribution describing a physical process. Random number generators normally produce uniformly distributed numbers in an interval $(0, 1]$. Thus, transformation methods have to be used in order to obtain random numbers distributed in the required way from sets of uniform random numbers. In this simulation, two standard methods, described for example in [8], have been used: The inversion method and the acceptance-rejection method.

3.2.1 The Inversion Method

The inversion method makes use of the following theorem:

Let $f(x)$ be the continuous probability density with which the random numbers are desired to be distributed and $F(x)$ be the according distribution function. The inverse of the distribution function F^{-1} shall be defined by

$$F^{-1}(u) = \inf\{x : F(x) = u, 0 < u < 1\}. \tag{3.19}$$

If U is a uniform random variable in [0,1], then $F^{-1}(U)$ is distributed like F.

This method is very efficient; Every uniform random number gets transformed into a random number following the desired distribution.
In practice, the inverse distribution function is calculated and then evaluated for uniform random numbers U. The obtained results are then distributed in the required way. This method is especially feasible if the inverse of the desired distribution is analytically accessible. However, this is often not the case so that it might be better to choose other methods, for instance the acceptance-rejection method.

3.2.2 The Acceptance-Rejection Method

If the inverse of the required distribution is not obtainable in a convenient way, another possibility to transform uniform distributions is the acceptance-rejection method.
This method allows the transformation of a distribution of random numbers that follows a probability distribution G with the according density $g(x)$ into one that follows the desired probability distribution F with density $f(x)$. With a positive constant $k \in \mathbb{R}$, the density $g(x)$ must meet the following requirement:

$$k \cdot g(x) \geq f(x) \qquad , \forall x \in \mathbb{R}. \tag{3.20}$$

If this is true, a sets of random vectors (u, x) is generated. The number u has to be of a uniform distribution in $[0, 1]$, the other random number x of distribution G. To transform the ensemble of numbers x into one following the desired distribution F, one has to remove the right elements from the initial ensemble so that the set of numbers left over constitutes an ensemble following distribution F. While the injection method realizes distribution F by transforming every initial random number in an appropriate way, the rejection method reaches that goal by eliminating all numbers that do not fit into distribution F.
Comparing the number u with the quotient $f(x)/(k \cdot g(x))$ gives the criterion if a number is to be removed or to be kept.
In practice, two random numbers u and x are generated. If

$$u > \frac{f(x)}{k \cdot g(x)}, \tag{3.21}$$

the random number x is rejected. One repeats that procedure until

$$u < \frac{f(x)}{k \cdot g(x)}. \tag{3.22}$$

In that case, the number x is accepted. The obtained number is now of the desired distribution.
The idea of the Acceptance-Rejection method is illustrated in figure 3.3.

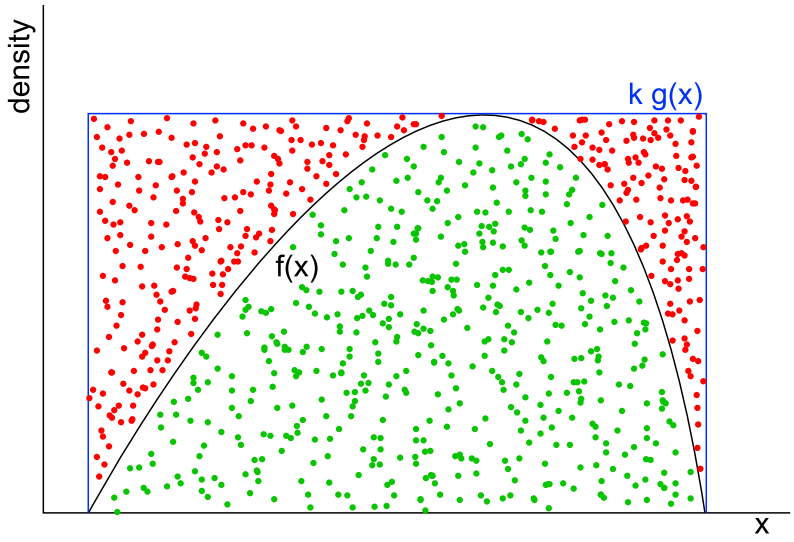

Figure 3.3: Visualisation of the Acceptance-Rejection method: random numbers according to probability density $k \cdot g(x)$ are diced (green and red dots). All but the numbers following distribution F get rejected (red dots). The remaining numbers (green dots) are then F-distributed.

3.3 Structure And Idea Of The Simulation

This simulation tracks the energy loss of single electrons over time. The variables determining the radiation process are obtained by random sampling, each following its own probability distribution.
Inverse Compton scattering in this work gets simulated as follows: An electron of energy E scatters with an CMB-photon of energy ϵ and loses energy to it in the process. This leaves the photon with a higher energy ϵ' and the electron with a lower energy E'. A time interval Δt is determined simulating the temporal evolution of that process.
Essentially, four quantities need to be determined, namely the

- electron's initial energy E, following a power-law distribution,
- energy of the target photon ϵ,
- the time between two scattering events Δt as well as the
- energy of the upscattered photon ϵ_1.

The first quantity, the electron's initial energy after its injection, can be obtained using the inversion method. Since the injection spectrum is assumed to be a power-law, the inverse of the according distribution function is easily derived:

$$F^{-1}(q) = E_{\text{min}} \times \left\{ 1 - q\big[1 - (E_{\text{min}}/E_{\text{max}})^{\alpha-1}\big] \right\}^{-\frac{1}{\alpha-1}}, \tag{3.23}$$

where q is the uniform random number provided by the random number generator and $\alpha > 1$ is the spectral index. The energetic boundaries of the injected electrons are denoted as E_{min} and E_{max}.

Point two on the list is the energy of the target photon ϵ.
Two scenarios for the target photon field have been assumed: A Planck-spectrum and a delta-distributed target photon spectrum.
In the first case the probability to get a photon energy ϵ should be black-body distributed. To obtain random photon energies following that distribution, the acceptance-rejection method has been used.
In the second case no random numbers are needed since the target photons' energy is a fixed parameter.

The time between two scattering events is obtained as follows:
Let $P(E, E')$ be the probability (3.11) of a radiation process leaving an electron of initial energy E with an energy E' after the collision. Then the double integral $P_{\text{tot}}(E, \epsilon) \equiv \int_{E_l}^{E_u} dE'\, P(E, E')$ corresponds to the total probability for the electron to end up in the energy interval $[E_l, E_u]$. Setting the energies E_l and E_u as the kinematic boundaries of the electron energy after the radiation process,

determined by its initial energy E and the target photon energy ϵ (compare to equation (1.18)), $P_{\text{tot}}(E, \epsilon)$ is the total probability for the electron to undergo inverse Compton scattering at all.
Using $P_{\text{tot}}(E, \epsilon)$, the problem is formally similar to the radioactive decay of a nucleus. The time between two radiation processes is thus given by the familiar differential equation

$$\frac{dN}{dt} = -P_{\text{tot}}(E, \epsilon)\, N \tag{3.24}$$

with the solution

$$t = -\frac{1}{P_{\text{tot}}} \ln \frac{N}{N_0} \equiv -\frac{1}{P_{\text{tot}}} \ln u. \tag{3.25}$$

The appropriate times get sampled by introducing uniform random numbers u out of an interval [0,1] into this expression.

The last quantity to be determined is the energy of the resulting photon. The probability distribution is given by equation (3.11). The associated random energies are generated using the acceptance-rejection method.

A sketch of the program is given with figure 3.4.

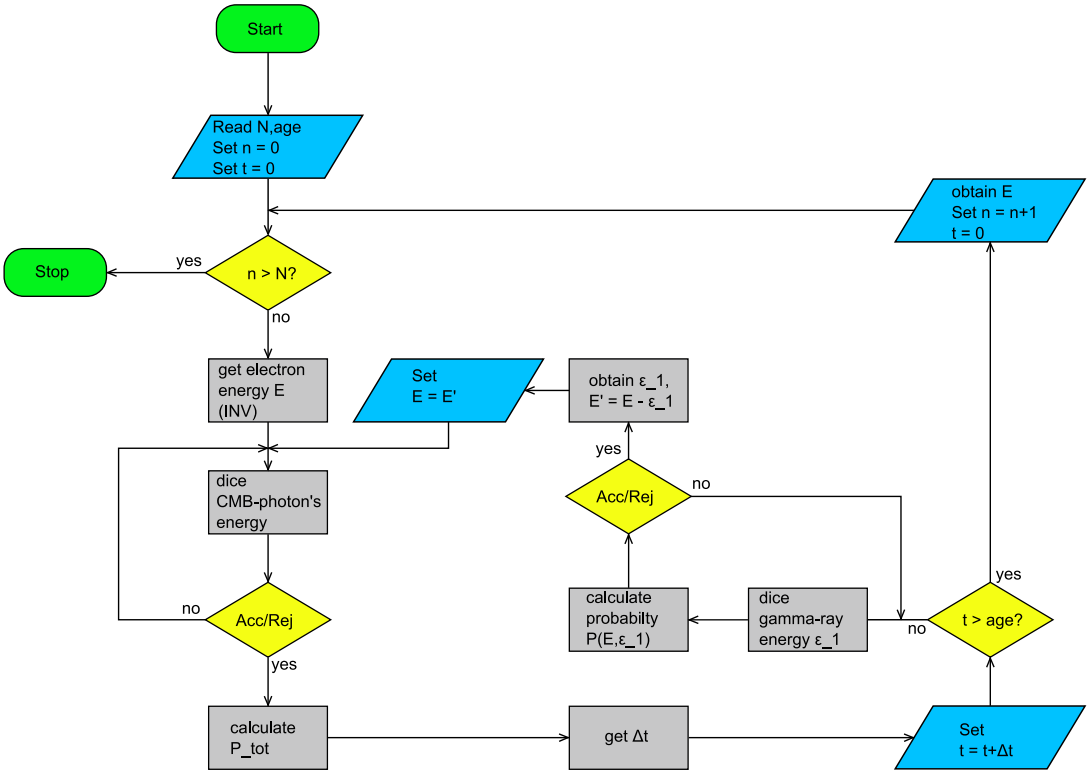

Figure 3.4: flowchart of the simulation

The program starts with reading a parameter file containing the total number of simulated electrons (N) and the object's age (age). An electron counter gets set to zero, as well as the time.
After that, two nested loops follow. The outer one increases the electron counter by one if an electron has finished the simulation. Upon reaching the total number of the electrons, the program is finished.
If this is not the case, an initial electron energy is diced and the program enters the inner loop, where at first a CMB-photon energy is determined.
The inner loop increases the passed time in the simulation by the time calculated from equation (3.24). If the resulting time is smaller than the age of the object, the radiation process is allowed to occur and a IC-photon energy is generated. The electron's energy gets set to $E = E - \epsilon_1$ and the program continues in this loop.
If the resulting time is larger than the object's age, the electron may not radiate and its simulation is over. The final electron energy gets saved as its energy after cooling, the time is reset and the program enters the outer loop.

If the target photon field is assumed to be delta-distributed $\rho(\epsilon) = \rho_0\delta(\epsilon - \epsilon_0)$, no integration is needed to obtain the probability of the resulting photon possessing an energy ϵ_1 because the integration over the target field yields (compare to equations (1.17) and (3.11))

$$\begin{aligned} P(E, E-\epsilon_1) &= \int_U^\infty d\epsilon \frac{dN_{\mathrm{IC}}}{dt d\epsilon d\epsilon_1} \\ &= \int_U^\infty d\epsilon \frac{2\pi r_0^2 c}{\gamma^2} \frac{\rho_0\delta(\epsilon-\epsilon_0)}{\epsilon} \left[2q\ln q + (1+2q)(1-q) + \frac{1}{2}\frac{(\Gamma q)^2}{1+\Gamma q}(1-q)\right] \\ &= \begin{cases} \frac{2\pi r_0^2 c}{\gamma^2}\frac{\rho_0}{\epsilon_0}\left[2q\ln q + (1+2q)(1-q) + \frac{1}{2}\frac{(\Gamma q)^2}{1+\Gamma q}(1-q)\right] & \text{if } \epsilon_0 \geq U \\ 0 & \text{else,} \end{cases} \end{aligned}$$

where $\Gamma = 4\epsilon\gamma/m_e c^2$ and $q = E/(\Gamma \times (E_e - \epsilon_1))$. U is the minimum target photon energy from which a photon with energy ϵ_1 may be obtained (see equation (3.11)).

3.4 Results

The simulation was conducted for different model settings. IC-scattering with both delta-distributed and black-body distributed target photons was simulated. Additionally, two different injection scenarios were assumed. Much like in chapter three

- burst-like injection, where all the pulsar's rotational energy gets injected as electrons instantly as well as
- stationary injection, in which case the pulsar injects electrons at a constant rate

were investigated. Stationary injection is quite different compared to continuous injection: In the latter case, the pulsar's luminosity follows equation (2.20), while for stationary injection the luminosity is a constant $L(t) = L_0$. This kind of injection is chosen because it is assumed in the analytical derivations, where the source term is temporally constant.

3.4.1 δ-Distributed CMB

The results presented in this section assume a delta-distributed target photon field $\rho(\epsilon) = \rho_0 \delta(\epsilon - \epsilon_0)$. With the temperature of the CMB $T_{\mathrm{CMB}} = 2.725K$ the photons are set to possess the mean energy of the Planck-distribution, $\epsilon_0 = 2.7kT_{\mathrm{CMB}} = 6.34 \times 10^{-4}$ eV. Using the energy density of an blackbody with a temperature T_{CMB}

$$w_{\mathrm{CMB}} = \int_0^\infty d\epsilon \; \epsilon \cdot [\pi^2(\hbar c)^3]^{-1}[\epsilon^2/(e^{\epsilon/\mathrm{k}T_{\mathrm{CMB}}} - 1] = 0.259\mathrm{eVcm}^{-3}, \tag{3.26}$$

the density ρ_0 can be derived.
For the energy density of the delta-distributed target photon field the following condition holds:

$$w_{\mathrm{CMB}} = 0.259 \ \mathrm{eVcm}^{-3} = \int_0^\infty d\epsilon \; \epsilon \cdot \rho_0 \delta(\epsilon - \epsilon_0) = \rho_0 \cdot \epsilon_0. \tag{3.27}$$

It follows, that the density ρ_0 has the value $\rho_0 = 409\mathrm{cm}^{-3}$.

Burst-Like Injection

Firstly, the results for an assumed burst-like injection are presented.
A number of 1 million electrons with energies between 10^{-1}TeV and 31.6 TeV has been simulated. The corresponding injection spectrum is shown in figure 3.5.

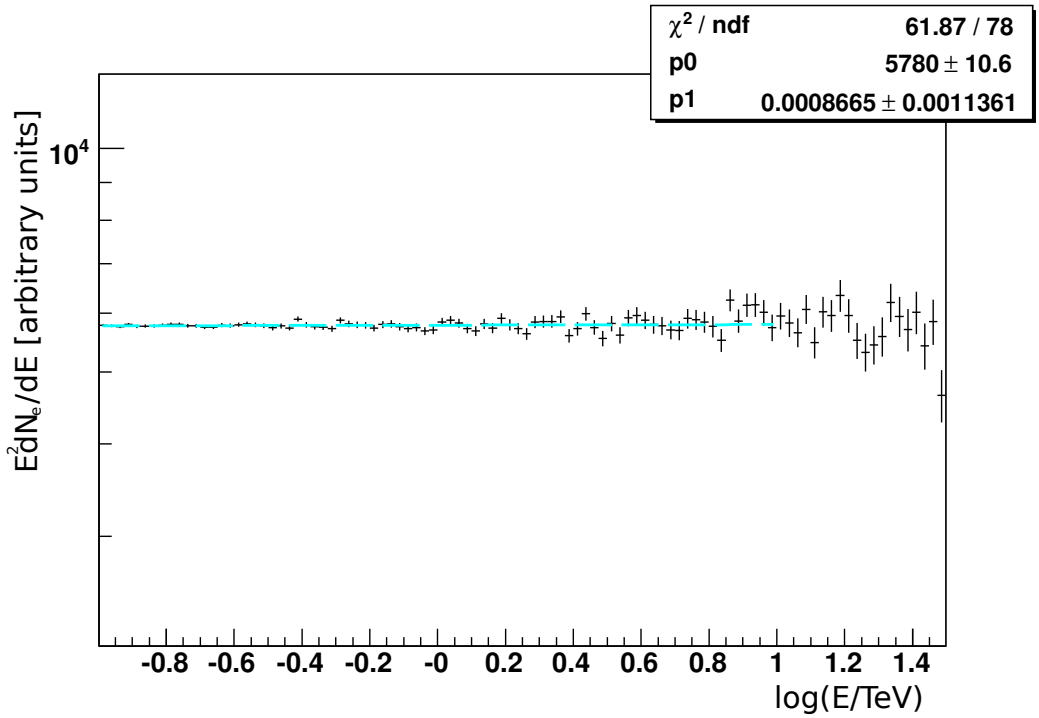

Figure 3.5: Initial electron spectrum before cooling, a power law with a spectral index of 2. This spectrum contains one million electrons.

The injection spectrum follows a power law with spectral index $\Gamma = 2$. At higher energies the statistics are getting worse, leading to larger fluctuations. This fact is a limiting factor of this simulation. In order to cope with low statistics at the upper end of the spectrum, a relatively narrow energy interval of the injected electrons has to be chosen.
One might think that simply increasing the electron number would be an apt way to advance statistics at high energies. But since the injection spectrum is power-law distributed, the number of additional electrons would have to be very large in order to improve the situation.
An example: For an energy interval $[10^{-1}\text{TeV}, 10^{3}\text{TeV}]$ and assuming a spectral index of two, the chance for an electron to posses an energy larger than 500TeV (in figure 3.5 this corresponds to the spectrum above log(E/TeV) $\simeq 2.4$) is about 0,01%. In order to double the amount of electrons above that energy, the total

number of injected electrons would have to be increased by four orders of magnitude.
This, however, would mean an increase of the program's runtime by a factor of 10000. Hence, the choice of a narrow energy interval for injected electrons is the best means to get proper statistics at high energies.

The electron spectrum after a simulated cooling time of one million years is shown in figure 3.6.

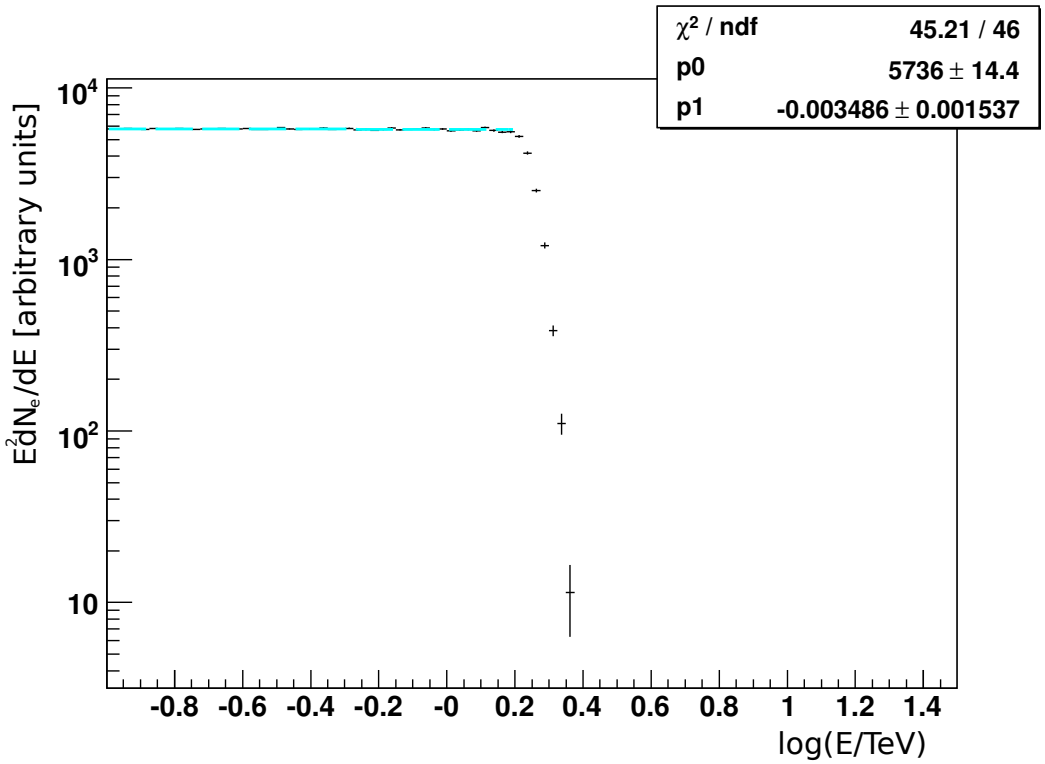

Figure 3.6: Electron spectrum after cooling, assuming a delta-distributed target photon field, burst-like injection and a spectral index of the injected electron spectrum of $\Gamma = 2$. The object is assumed to be 10^6 years old. A total of 1 million electrons has been simulated.

As one can see, the electron spectrum after cooling drops down rapidly above a certain energy E_{cut}. Below this energy, a power law with the same spectral index as the injected spectrum is observed.
All electrons in this simulation have been cooled for the same amount of time, and all electrons have ended up at energies below E_{cut} in a way that again they form power law.
The cut-off energy E_{cut} corresponds to the Thomson regime (see section 3.1), therefore this simulated spectrum's features have to be compared to the analytical results for inverse Compton scattering in the Thomson limit.

The behaviour of the spectrum shown in figure 3.6 agrees with these analytical results. In the case of an initial spectral index of $\Gamma = 2$ and burst like injection the analytical results imply a cut off at $E_{cut} = 1/(bt)$ and a power law with spectral index of $\alpha = 2$ below that energy (see equation (3.8)). The analytically expected value for E_{cut}, assuming an energy density $w_{\mathrm{CMB}} = 0.259$ eVcm^{-3} and a cooling time of one million years, is $E_{cut} = 1.22$ TeV. With a value of about 1.6 TeV, the cut-off energy obtained by the simulation is too high by a factor of about 1.3.

Figure 3.7 shows simulated electron spectra after cooling using the same parameters as in the previous example but for three different spectral indices of the injected electron power-law spectra.

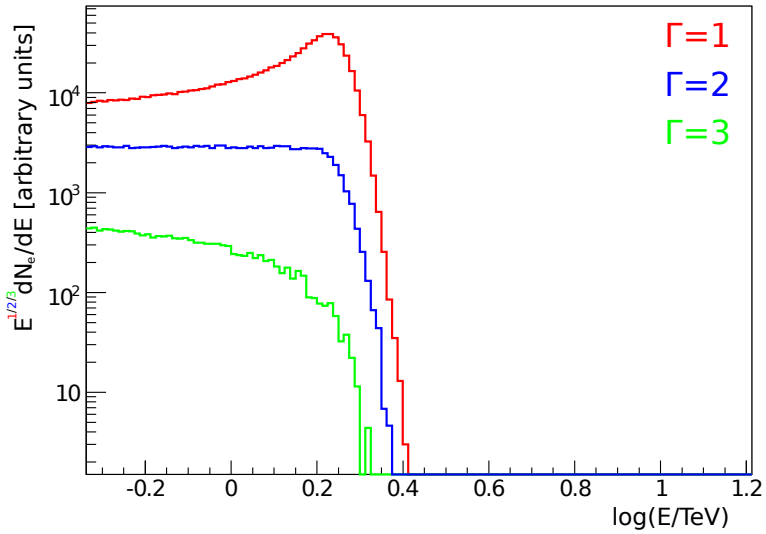

Figure 3.7: Electron spectra after cooling, assuming a delta-distributed target photon field, burst-like injection and different spectral indices Γ of the injection spectra. Red: $\Gamma = 1$, blue: $\Gamma = 2$, green: $\Gamma = 3$. The object is assumed to be 10^6 years old. For each spectrum a total of 1 million electrons has been simulated.

The red line corresponds to an injection spectrum with spectral index $\Gamma = 1$. It shows a pile-up at the cut-off energy E_{cut} followed by rapid spectral drop, as it is analytically expected (compare to equation (3.8) and figure 3.26). If the injection spectrum's spectral index is $\Gamma = 3$, the cooled electron spectrum shows a drop at energies $E \lesssim E_{cut}$ (green line in figure 3.7), which is analytically expected as well (compare to equation (3.8) and figure 3.26). The blue line has already been discussed in figure 3.6.

Contrary to the electron spectra obtained by this simulation, the photon spectra are integrated over time. This is because the photons emitted by the electrons get accumulated over the course of the simulation. However, the timescale on which the spectrum changes increases as time passes, since electrons get cooled down to lower energies and therefore their radiative cooling time increases as $t \propto 1/E$ in the case of inverse Compton scattering in the Thomson limit (see equation (2.13)). By accumulating only photons of sufficiently recent origin, i.e. over past times that are much smaller than the radiative cooling time of the highest energetic electrons populating the spectrum, one can assume that the spectrum does not change significantly during that time interval and it is possible to approximate an actual photon spectrum. Figure 3.8 shows a photon spectrum accumulated over the past 100 years. This is a small time interval compared to the cooling time of 1.6 TeV electrons which is about one million years.

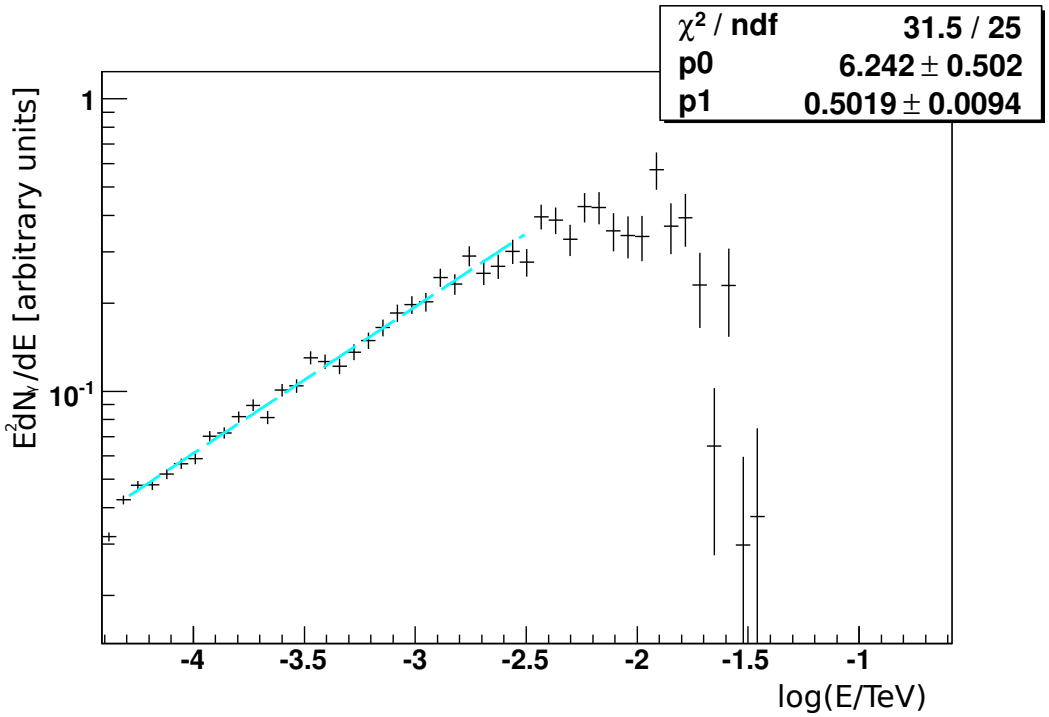

Figure 3.8: Photons emitted during the last 100 years of the simulation corresponding to the spectrum shown in 3.6.

The spectrum follows a power law with a spectral index of 1.5 below a characteristic energy above which it drops down rapidly.
Analytically, the following behaviour is expected: If the spectral index of the photon producing electron distribution is α, then the photon spectrum should possess a spectral index of $(\alpha + 1)/2$. In the analytical approach the electron

spectrum from which the photon spectrum is derived is the electron spectrum after cooling, in this case the spectrum shown in figure 3.6. Because this spectrum is a power-law with spectral index 2 and a cut-off at energy E_{cut}, the resulting photon spectrum should follow a power law with a spectral index of 1.5 and experience a cut-off at an energy that mirrors E_{cut}. By inverse Compton scattering in the Thomson limit, target photons gain energy in the order of γ^2, where γ is the Lorentz factor of the scattering electrons (compare to relation (1.5)). The maximum energy the photon can obtain is $\epsilon_1^{max} \approx 4\gamma\epsilon$, where ϵ is the photon energy before scattering (see Blumenthal and Gould [6]). Assuming a maximum electron energy of $E_{max} \approx 1.6$ TeV, this energy should be mirrored in the photon spectrum by a cut-off at $E_{cut}^{phot} \approx 20$ GeV, which is in good accordance to the cut-off energy observed in the simulated photon spectrum.
Thus, the photon spectrum apparently fulfils the analytical expectations.

Figure 3.9 features the electron and gamma-ray spectrum resulting from cooling one million electrons out of an energy interval [1 TeV, 10^4 TeV] and of an age of 100000 years due to inverse Compton scattering.

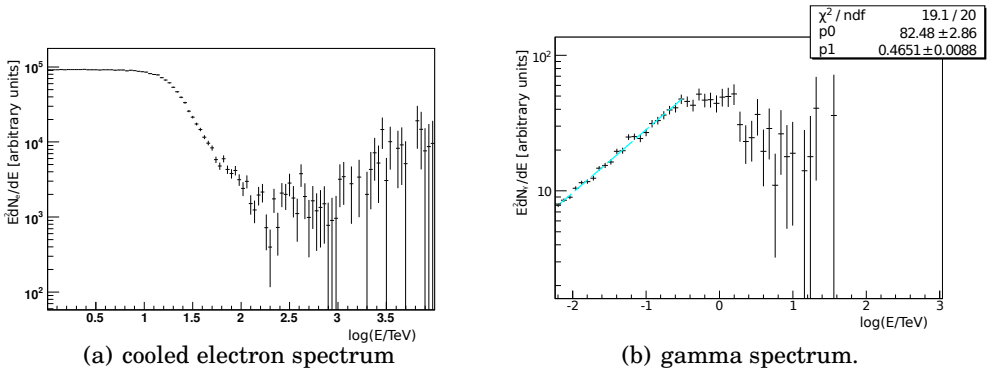

(a) cooled electron spectrum (b) gamma spectrum.

Figure 3.9: Electron spectrum after cooling and the corresponding gamma-ray spectrum integrated over the past 100 years. A delta-distributed target photon field, burst-like injection and a spectral index of the injected electron spectrum of $\Gamma = 2$ are assumed. The object is set to be 10^5 years old. A total of 1 million electrons has been simulated.

The electron spectrum in this case shows a power-law with a spectral index of 2 below an energy $E \approx 10$ TeV. Above that energy the spectrum drops rapidly until at energies $E \gtrsim 100$ TeV the spectrum gets increasingly harder.
The photon spectrum follows a power law with a spectral index of 1.54 below an energy of 0.4 TeV. At higher energies the spectrum decreases at a relative slow rate.
Analytically, due to inverse Compton scattering in the Thomson limit a power law with the injection spectrum's spectral index $\Gamma = 2$ is expected for the cooled

electron spectrum, followed by a sharp cut-off at $E_{cut} = 12.2$ TeV. The spectrum shown in figure 3.9 fulfils the analytical expectations at energies below 10 TeV but deviates at higher energies. A similar behaviour is observed in the gamma-ray spectrum: below an energy that mirrors the 10 TeV in the electron spectrum (following the discussion of figure 3.8, this energy is $E_{ph} \approx 4\gamma^2_{10\ \mathrm{TeV}}\epsilon \approx$ 0.5 TeV) the spectrum follows the analytical expectations of a power law with a spectral index of 1.5 (see equation (3.18)) rather well. At higher energies, where in the case of inverse Compton scattering in the Thomson limit a sharp spectral drop (mirroring the cut-off in the electron spectrum) is expected, the simulated photon spectrum decreases only relatively slowly.
These deviations might be caused by Klein-Nishina effects due to a decreased cooling efficiency at high energies, leading to an abundance of electrons with energies larger than E_{cut} in the spectrum. The spectral cut-off in the electron spectrum is at energies adjacent to a spectral range that marks the transition from the Thomson to the Klein-Nishina scattering regime ($0.1 \lesssim 4\epsilon_0 E/(m^2c^4) \lesssim 10$, see section 3.1). In this energy range neither the analytical results for inverse Compton scattering in the Thomson limit nor in the Klein-Nishina limit hold and thus spectra in that energy interval are expected to show deviant characteristics.

Stationary Injection

Assuming stationary injection, the model yields a cooled electron spectrum as it is shown in figure 3.10. A number of one million electrons following a power-law distribution with spectral index $\Gamma = 2$, energies between 10^{-1}TeV and 31.6 TeV and an age of one million years has been simulated.

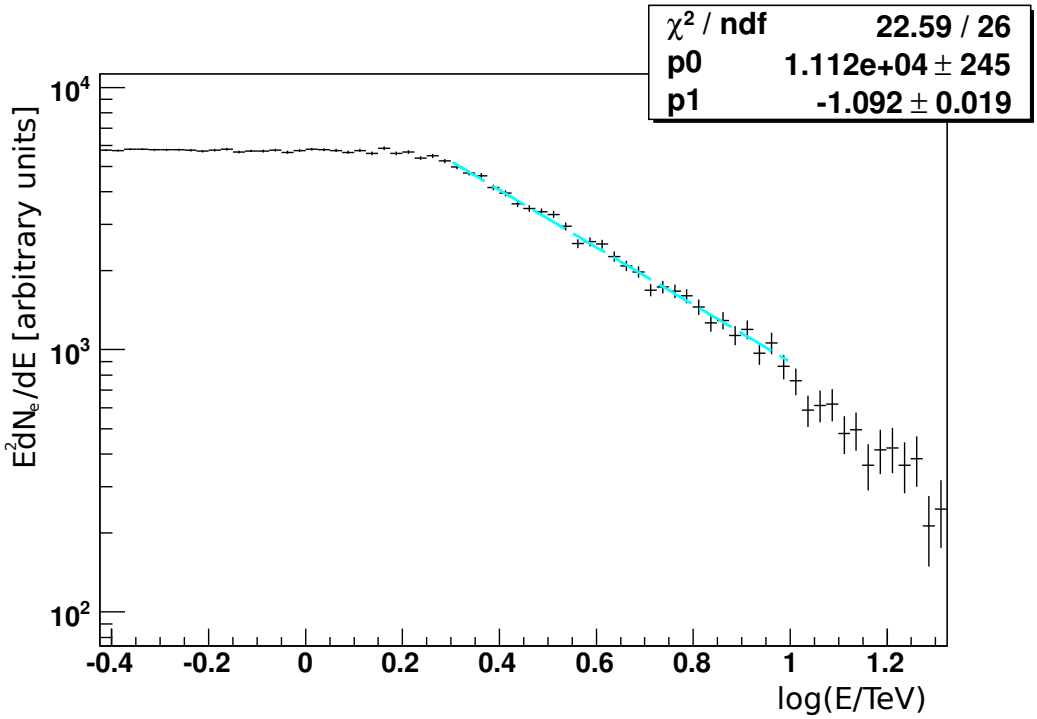

Figure 3.10: Electron spectrum after cooling, assuming a delta-distributed target photon field and a spectral index of the injected electron spectrum of $\Gamma = 2$. The object is assumed to be 10^6 years old and to inject stationarily. A total of 1 million electrons has been simulated.

Under these assumptions, the spectrum is no longer a power law with a cut-off but a broken power law. Below an energy $E_{break} \approx 1$ TeV, the spectrum has the shape of a power law with a spectral index of $\alpha = 2$. Above that energy, the spectrum softens as the spectral index increases by one to $\alpha \approx 3$.
The spectrum qualitatively follows the analytical expectations. Exactly the same broken power-law for stationary injection was derived by Kardashev (equation 3.26). The analytically expected breaking energy is given by $E_{break} = 1/(bt) = 1.22$ TeV with the assumed parameters and roughly coincides with the simulated breaking energy.

Figure 3.11 shows the spectrum of photons that have been upscattered by the electrons corresponding to the spectrum shown in figure 3.10 during the last 100 years of the simulation.

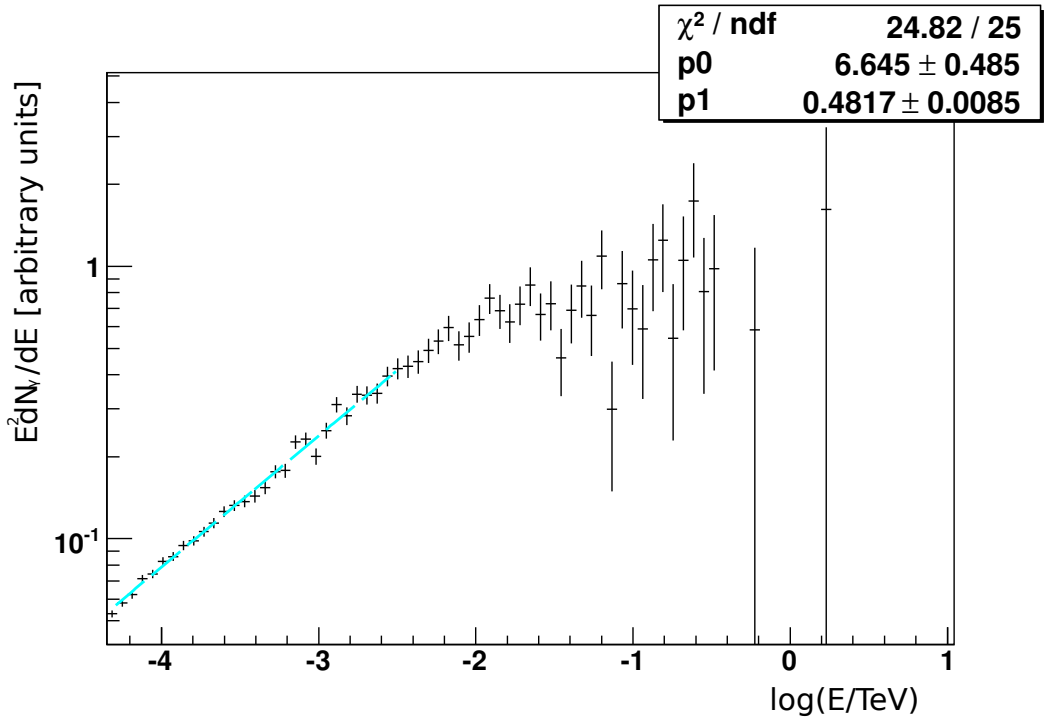

Figure 3.11: Photons emitted during the last 100 years of the simulation corresponding to the spectrum shown in 3.10.

The spectrum follows a power law with spectral index of about 1.52 up to a photon energy of about 10 GeV above which the spectrum's slope decreases.
This behaviour might agree with the analytical expectations for inverse Compton scattering in the Thomson limit and an assumed stationary electron injection: Since under these assumptions the spectral index of the photon spectrum should be $(\alpha + 1)/2$, where α is the cooled electrons' spectral index (see equation (3.18)), a broken power law is expected with a breaking energy E_{break}^{phot} that mirrors the breaking energy E_{break} in the electron spectrum. As already discussed, in the Thomson limit electrons scatter target photons up to energies $\epsilon_1^{max} \approx 4\gamma\epsilon$, where γ is the Lorentz factor of the scattering electron. By introducing the Lorentz factors of electrons with energy E_{break} into that equation, the corresponding breaking energy in the photon spectrum E_{break}^{phot} is obtained. Thus a breaking energy in the electron spectrum of about 1 TeV is mirrored in the gamma-ray spectrum at an energy of about 10 GeV which fits the breaking energy in the simulated photon spectrum.
Photons below E_{break}^{phot} correspond to electrons below E_{break}. These electrons follow a power-law with spectral index $\alpha = 2$ (see figure 3.10) and thus a spectral

index of 1.5 is expected for photons at energies smaller than E_{break}^{phot} and can be observed in the simulated photon spectrum. Analogously photons at energies above E_{break}^{phot} correspond to electrons above E_{break}, which follow a power law with spectral index $\alpha = 3$. Therefore a spectral index of 2 is expected for photon energies larger than E_{break}^{phot}. Possibly the decrease in the spectrum's slope corresponds to that expectation.

Looking at electron energies $E > 10^4$ TeV which correspond to the deep Klein Nishina regime shows a very different behaviour of the cooled electrons. In this energy range the spectrum follows a power law with a spectral index of $\alpha \approx 1.4$, as can be seen in figure 3.12, where one million power-law distributed ($\Gamma = 2$) electrons out of a higher energy interval [10^4 TeV, 10^5 TeV], corresponding to the deep Klein-Nishina regime, have been cooled for one million years in the simulation.

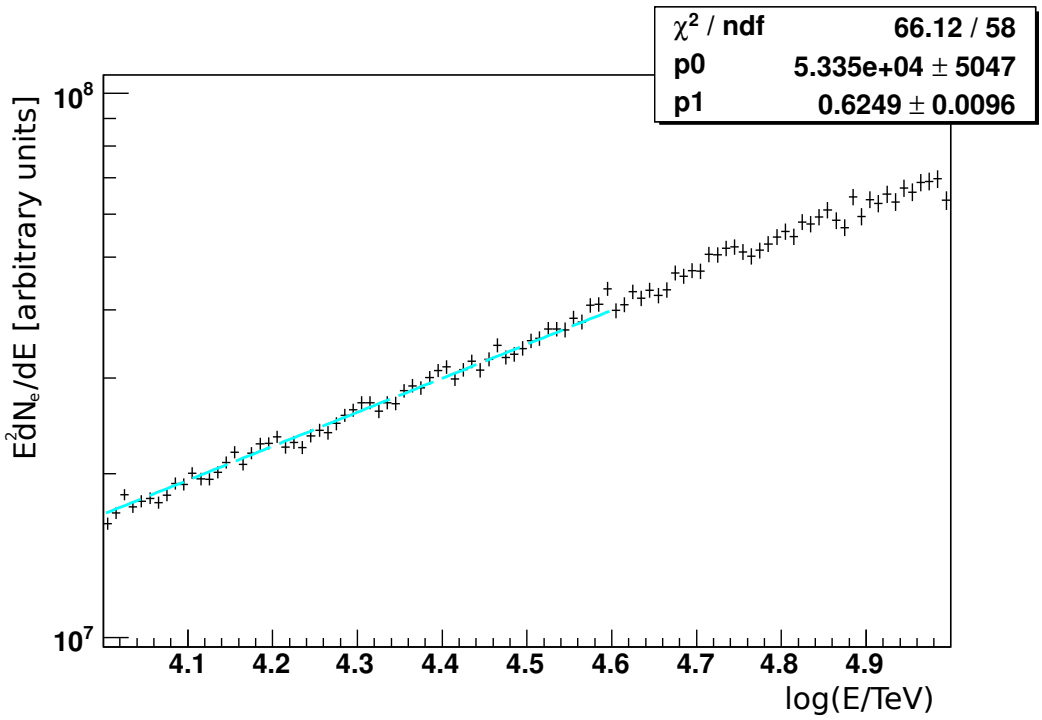

Figure 3.12: Electron spectrum after cooling, assuming a delta-distributed target photon field. The object is assumed to be 10^6 years old and to inject stationarily. A total of one million electrons out of an energy interval [10^4 TeV, 10^5 TeV] has been simulated.

This behaviour possibly agrees with the findings of Moderski et al. [20] since the spectral index of $\alpha \approx 1.4$ may coincide with their result (3.15) if the injected electrons' spectral index is $\Gamma = 2$, as it is the case in this simulation.

The corresponding gamma-ray spectrum shows very poor statistics. No interpretations or deductions may be made for that spectrum.
This behaviour is possibly caused by the decreased Klein-Nishina cross section at that energies which reduces the scattering rate. As a result, only few photons are emitted during the last 100 years of the simulation leading to low statistics.

3.4.2 Blackbody-Distributed CMB

In this section the results of the simulation under the more realistic assumption of a blackbody-distributed target photon field with a temperature of $T_{CMB} = 2.725$ K will be presented.
The number of simulated electrons is smaller than in the simulations assuming delta-distributed target photons because the simulation's runtime is significantly higher assuming a blackbody target photon field.
This is mainly because a nested integration is necessary to compute the total scattering probability for each scattering (compare to section 3.3), whereas in the case of a delta distributed target photon field only a single integration is required. However, the results are very similar to the ones obtained assuming a delta-distributed target photon field. Therefore in the following only the most important results will be shown.

Burst-Like Injection

Figure 3.13 shows the electron spectrum after cooling assuming a burst-like injection of 200000 electrons out of an energy interval [0.1 TeV, 31.6 TeV] and

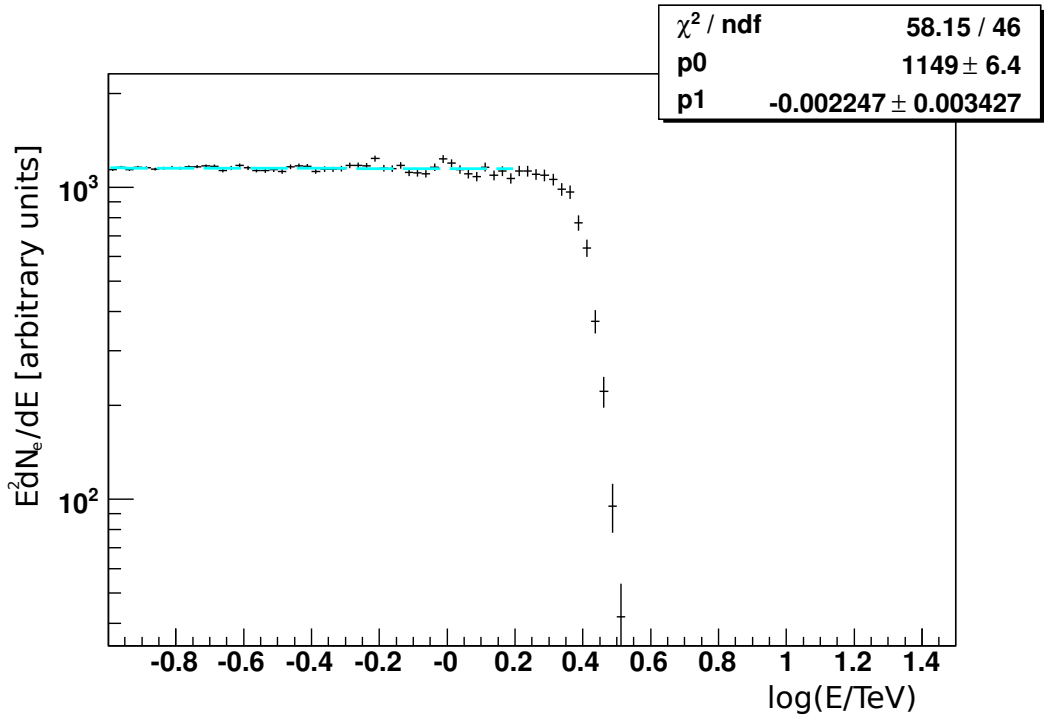

Figure 3.13: Electron spectrum after cooling, assuming a blackbody-distributed target photon field. The object is assumed to be 10^6 years old and to inject in a burst-like manner. A total of 200000 electrons has been simulated.

a simulated time of one million years. The injected electron spectrum follows a power law with spectral index $\Gamma = 2$. Like in the case of a delta-distributed radiation field and burst like injection, see figure 3.6, also this spectrum follows a power-law with the spectral index of the injected electron spectrum $\alpha = \Gamma = 2$, followed by a sharp decline above a characteristic energy $E_{cut} \approx 2$ TeV.
This similarity is to be expected, since in the Thomson regime, where E_{break} is located, the analytical solution does not depend on the spectral shape of the target photon field.
Because of that, the spectrum can be discussed in the same manner as in the case of burst-like injection and a delta-distributed ambient photon field, see the discussion of figure 3.6.
Compared to the analytically expected value for the cut-off energy of 1.22 TeV the simulated value of about 2 TeV is too high by a factor of about 1.67.

Figure 3.14 features the corresponding photon spectrum accumulated over the last 100 years of the simulation.

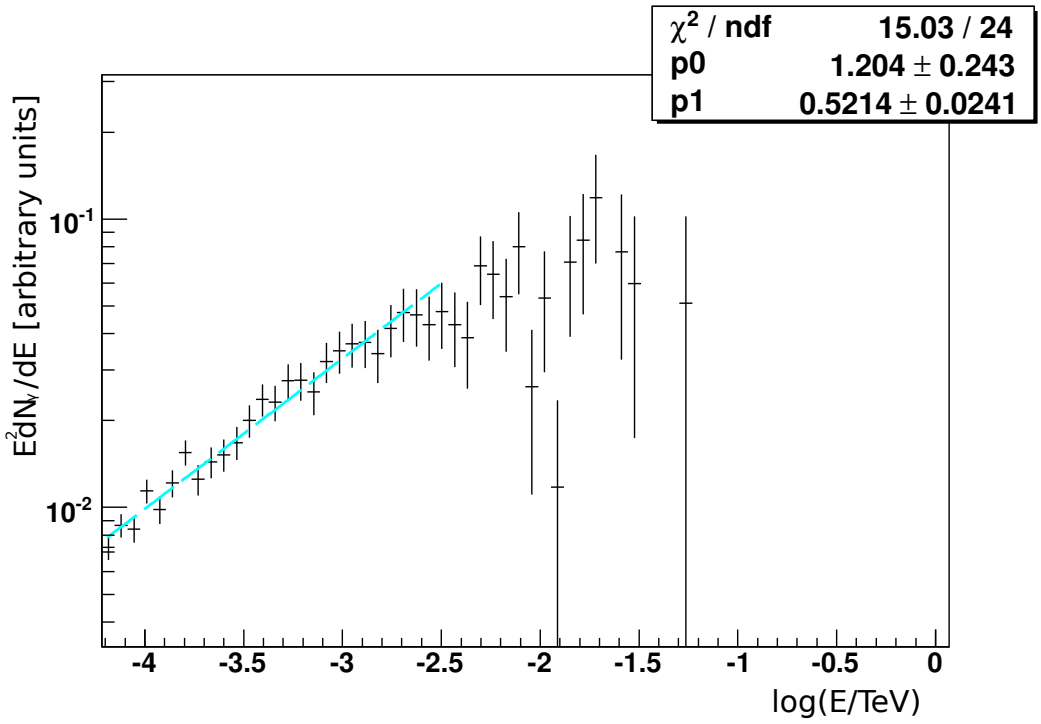

Figure 3.14: Photons emitted during the last 100 years of the simulation corresponding to the spectrum shown in 3.13.

Despite its low statistics, this spectrum shows a similarity to the spectrum obtained by upscattering delta-distributed target photons (see figure 3.8): also in this case a power law with a spectral index of 1.5 is observed, followed by

a rapid drop above a energy of about 20 GeV. Since in the Thomson limit the analytical result for the gamma-ray spectrum does not depend on the spectral shape of the target photon distribution, the spectrum shown in figure 3.14 can be discussed analogously to the gamma-ray spectrum in figure 3.8.

Stationary Injection

In figure 3.15 the spectrum of the electrons after being cooled for one million years assuming a blackbody-distributed target photon field and stationary injection of 200000 electrons out of an interval [0.1 TeV, 31.6TeV] following a power law with spectral index $\Gamma = 2$ is shown.

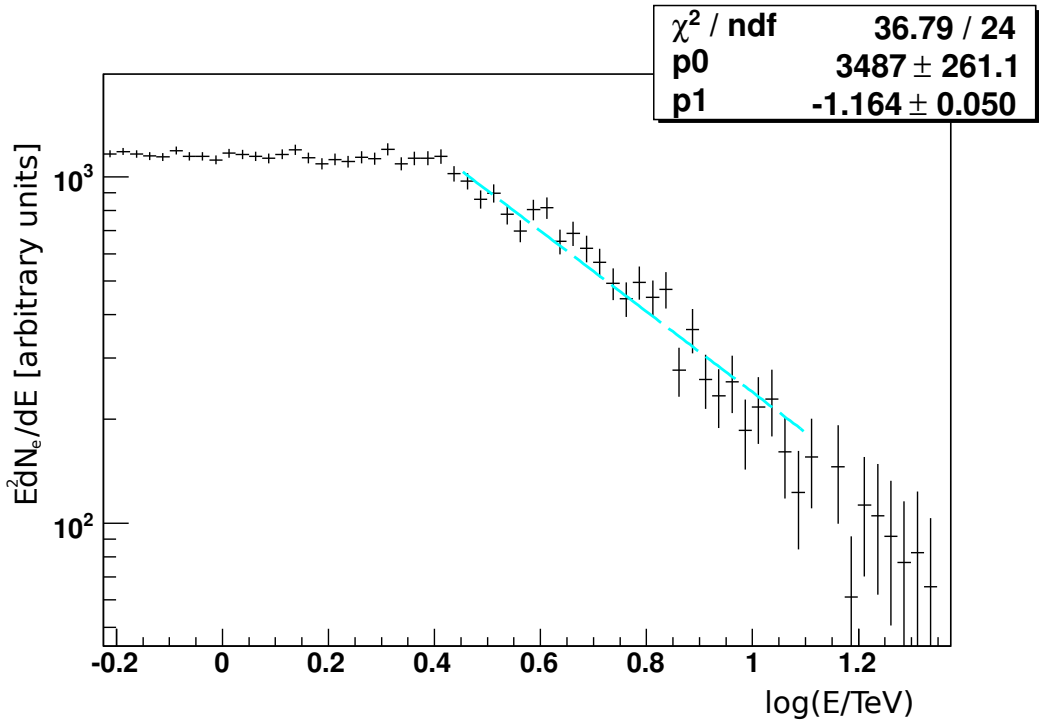

Figure 3.15: Electron spectrum after cooling, assuming a blackbody-distributed target photon field. The object is assumed to be 10^6 years old and to inject stationarily. A total of 200000 electrons has been simulated.

There is a great similarity to figure 3.10. The spectrum also follows a broken power law with a spectral index of $\alpha = 2$ below and $\alpha \approx 3.1$ above the breaking energy. This behaviour is analytically expected and was explained in the discussion of the spectrum presented in figure 3.10. With about 2.5 TeV the breaking energy is larger than the analytically expected value of 1.22 TeV by a factor of about 2.

The spectrum consisting of photons emitted during the last 100 years of the simulation leading to the electron spectrum in figure 3.15 is shown in figure 3.16.

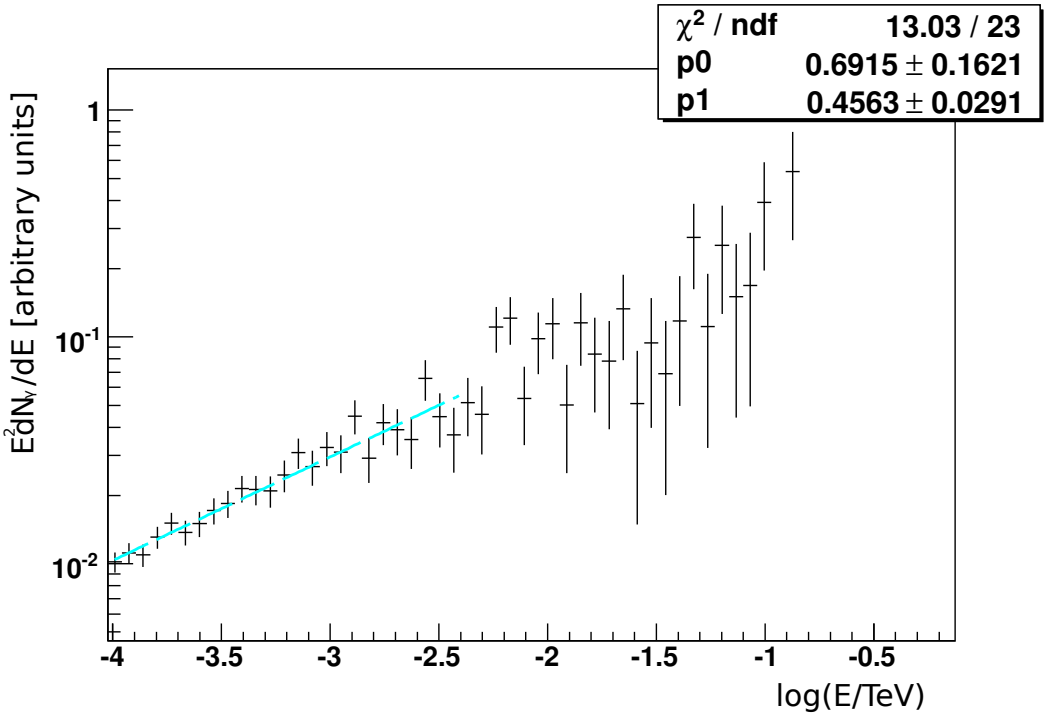

Figure 3.16: Photons emitted during the last 100 years of the simulation corresponding to the spectrum shown in 3.15.

The statistics are very poor but at energies lower than about 10 GeV a power law with a spectral index of 1.5 can be observed. As already mentioned in the discussion of the corresponding photon spectrum obtained by scattering with delta-distributed target photons in figure 3.11, this is analytically expected. Above that energy the spectrum seems to deviate from the expected analytical behaviour of a power law with spectral index 2.

Figure 3.17 shows the spectrum of 200000 electrons out of an energy interval [10^4 TeV, 10^5 TeV] (which corresponds to the deep Klein-Nishina regime) following a power law with a spectral index of $\Gamma = 2$ after being cooled for a simulated time of one million years.

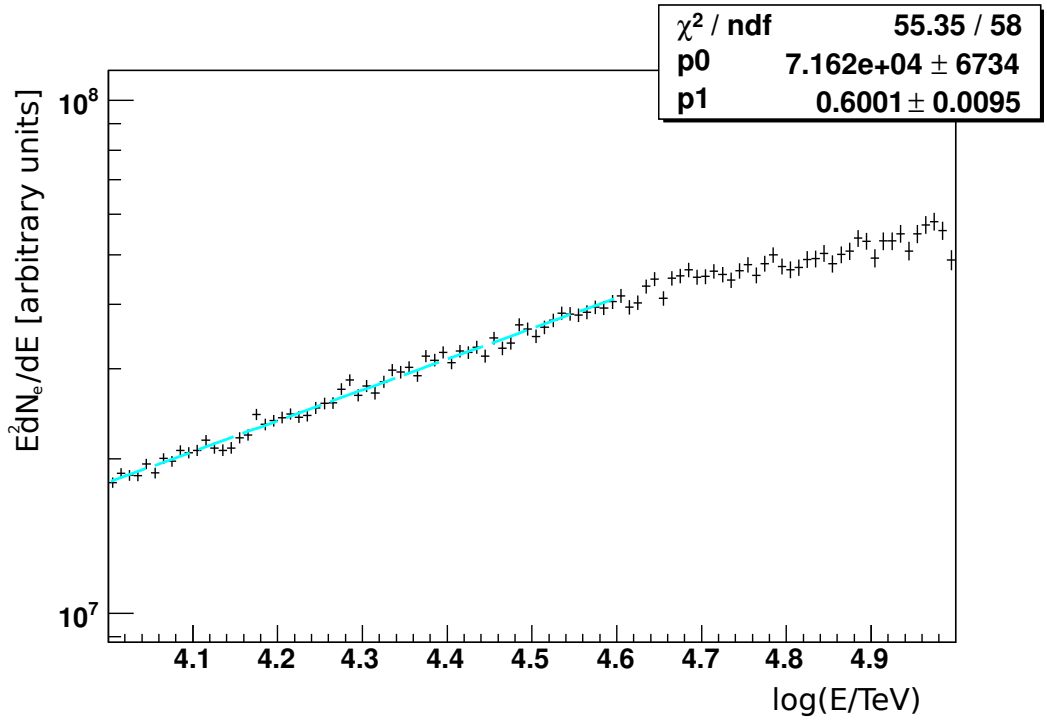

Figure 3.17: Electron spectrum after cooling, assuming a blackbody-distributed target photon field. The object is assumed to be 10^6 years old and to inject stationarily. A total of 200000 electrons out of an energy interval [10^4 TeV, 10^5 TeV] has been simulated.

In this energy range, the spectrum follows a power-law with a spectral index of $\alpha \approx 1.4$ which is a similar behaviour as in the case of a delta-distributed target photon field (compare to figure 3.12).
Also this result may be in agreement with Moderski et al.
The corresponding gamma-ray spectrum suffers from the same problems like the one obtained for a delta-distributed target photon field (see section 3.4.1). In fact, the situation is even worse since less electrons have been simulated.

If the results obtained from this simulation are correct, then the analytical expectations for electron spectra after being subjected to radiative cooling by inverse Compton scattering have been qualitatively reproduced in the Thomson limit, where the obtained spectra follow the expected power-law behaviour (compare to equation 3.26). In the Klein-Nishina regime, the results seem to favour the analytical solution obtained by Moderski et al [20].

Unfortunately, the obtained values of the cut-off and breaking energies E_{cut} and E_{break} in the cooled electron spectra have not been exactly reproduced. In the case of a blackbody-distributed target photon field the obtained values are off by factors up to 2. This situation improves under the assumption of a delta-distributed target photon field, where the obtained values are off by factors up to 1.6. This discrepancy in energy needs further investigation.

4 Conclusion And Outlook

This work was split in to parts:

- the VHE gamma-ray emission model for PWNe and
- the Monte-Carlo simulation of inverse Compton scattering.

Firstly, the VHE gamma-ray emission model and the Monte-Carlo simulation will be summed up. Afterwards the parts will be compared. Finally, an outlook will be given.

4.1 Conclusion

4.1.1 The Gamma-Ray Emission Model For PWNe

In the first part of this work, the gamma-ray emission from PWNe was modelled assuming

- a power law electron injection spectrum with exponential cut-off,
- a burst-like injection as well as a continuous injection scenario,
- electron radiation losses due to synchrotron radiation and inverse Compton scattering in the Thomson limit,
- propagation by isotropic, energy dependent diffusion and
- gamma ray emission by synchrotron radiation with an isotropic pitch angle distribution and by inverse Compton scattering using the exact Klein-Nishina cross section and gray-body distributed target photon fields (the CMB as well as the ambient infrared and optical photon fields).

In particular the assumption of the inverse Compton energy losses to behave like in the Thomson scattering regime is only decent at an electron energy corresponding to that regime. Depending on the energy of the target photon this electron energy varies. For inverse Compton scattering with the optical photon field the transition from the Thomson to the Klein-Nishina regime already takes place at about 100 GeV. Thus, at higher energies, the utilized form of the electron energy loss rate is an increasingly bad assumption, since the scattering approaches the deep Klein-Nishina regime where it shows a different character.

Another problem of the model is the uncertainty of the diffusion coefficient's normalization and energy dependence in the VHE range. Since for a given life time of the particles the diffusion coefficient determines the distance they traverse due to diffusion, its behaviour is of great importance to the model. Uncertainties at this point thus greatly limit the reliability of the model's results.

However, the application on the Geminga PWN shows that the gamma-ray flux at 20 TeV as seen by the Milagro experiment can be reproduced by this model by using reasonable physical parameters. Moreover, the model seems to be in agreement with the flux upper limit at 6.2 GeV as it was measured by the EGRET telescope.

Also the emission's angular extension of $\vartheta \sim 3$ degrees at 20 TeV seems to agree with the observations of Milagro, where a similar extension is obtained.

4.1.2 The Monte-Carlo Simulation Of Inverse Compton Scattering

In the second part of this work, the inverse Compton scattering process was investigated over a large energy interval with a stochastic simulation under the following assumptions:

- The electron injection spectrum follows a power law.
- The electron-target photon interaction is described with the exact Klein-Nishina cross section.
- Only the CMB as delta respectively black-body distributed target photon field is accounted for.

Up to now, only the CMB was taken into account as target photon field. Since in the vicinity of stars additional target photon fields with energy densities comparable to that of the CMB are present (i.e. the ambient infrared and optical photon fields), this assumption is not very realistic for the most locations in our vicinity.

Another problem of the simulation is the fact that it can not produce actual gamma-ray spectra but only integrated gamma-ray spectra over time. This, however, is not true for the electrons, where proper spectra may be obtained.

Assuming that the simulation is programmed properly, the simulation should produce accurate electron spectra in the VHE range, since the exact Klein-Nishina cross section is used in all steps.

The analytical expectations for inverse Compton scattering in the Thomson limit seem to be reproduced by the simulation, assuming both delta and

blackbody-distributed target photon fields:
in the scenario of a burst-like injection, the spectral cut-off in the electron spectrum and the according cut-off in the gamma-ray spectrum can be simulated. However, the corresponding energies are off by factors up to 2. The same holds for the break in the electron spectrum assuming stationary injection. In both injection scenarios the simulated spectral indices of the electron and gamma-ray spectra meet the analytical expectations, except for photons emitted by stationarily injected electrons above the spectral break, where the determination of the spectral index was difficult due to low statistics. Furthermore, analytically expected pile-ups and decreases in the electron spectra near the spectral cut-off assuming spectral indices of 1 respectively 3 for burst-like injected electrons are reproduced.

At higher energies corresponding to the deep Klein-Nishina regime, the obtained results may be in agreement with the analytical expectations formulated by Moderski et al. but seem to differ from the results obtained by Blumenthal and Gould.

4.1.3 Comparison Of The Two Parts

By comparing the results obtained by the different projects with one another, the following deductions can be made:

- A comparison of the electron density spectrum in the burst-like injection scenario as obtained by the PWN-emission model for energy independent diffusion (see the red line in figure 2.1) with the electron spectrum yielded by the Monte-Carlo simulation for the same injection scenario (see figure 3.13) shows a great similarity.
  In both cases the spectrum experiences a cut off at a certain energy below which the spectral shape of the injection spectrum can be observed.
  The spectrum from the Monte-Carlo simulation is similar to the electron density from the PWN model only if the diffusion is energy independent. This is because in the Monte-Carlo simulation no propagation mechanism whatsoever is implemented. Thus, the spectral deformation caused by energy dependent diffusion cannot be simulated. Energy independent diffusion, however, does not distort the electron density's spectral shape and thus is the proper object of comparison.

- Klein-Nishina effects have a large impact on the electron spectrum at energies $E_e > 100$ TeV (see, for example 3.9). Neglecting them in the PWN emission model causes a large error at these energies. This holds for inverse Compton scattering with the CMB. For scattering with the other ambient photon fields similar effects are to be expected at lower energies.

4.2 Outlook

Future work on the PWN emission model as well as on the Monte-Carlo simulation could include the following ideas:

- An inverse Compton electron loss rate that is valid in all scattering domains could be implemented in the PWN emission model. This is possible, since the expressions for the radiative cooling time (see equation (2.5)) and mean squared diffusion length(see equation (2.6)) put no constraints on the functional properties of the total electron energy loss rate. However, since this generalization allows for large electron energy losses, particle leakage might have to be accounted for.
  This modification would increase the validity of the model at photon energies larger than several tens of GeVs.

- Energy dependent diffusion might be implemented by providing a random travelling distance and direction to an electron between scattering events. Of course these random quantities would have to follow the appropriate probability distributions.
  By doing this, the spatial distribution of the electrons at a given time and energy could be simulated.

- Additional injection scenarios could be implemented in the MC-simulation, for example continuous injection. Together with an implementation of energy dependent diffusion, this might allow for a simulation of the line-of-sight integral over the electron densities as produced by pulsars (compare to section 2.2.2). From this, a photon spectrum could be numerically derived, leading to a self consistent result with respect to energy losses and gamma ray emission. However, the runtime of the simulation would have to be greatly reduced in order to realize that kind of application.

Bibliography

[1] A. A. Abdo, B. Allen, D. Berley, S. Casanova, C. Chen, D. G. Coyne, B. L. Dingus, R. W. Ellsworth, L. Fleysher, R. Fleysher, M. M. Gonzalez, J. A. Goodman, E. Hays, C. M. Hoffman, B. Hopper, P. H. Hüntemeyer, B. E. Kolterman, C. P. Lansdell, J. T. Linnemann, J. E. McEnery, A. I. Mincer, P. Nemethy, D. Noyes, J. M. Ryan, P. M. Saz Parkinson, A. Shoup, G. Sinnis, A. J. Smith, G. W. Sullivan, V. Vasileiou, G. P. Walker, D. A. Williams, X. W. Xu, and G. B. Yodh. TeV Gamma-Ray Sources from a Survey of the Galactic Plane with Milagro. *apjl*, 664:L91–L94, August 2007.

[2] A. A. Abdo and for the Fermi LAT collaboration. The First Fermi Large Area Telescope Catalog of Gamma-ray Pulsars. *ArXiv e-prints*, October 2009.

[3] F. Aharonian, A. G. Akhperjanian, A. R. Bazer-Bachi, M. Beilicke, W. Benbow, D. Berge, K. Bernlöhr, C. Boisson, O. Bolz, V. Borrel, I. Braun, F. Breitling, A. M. Brown, R. Bühler, I. Büsching, S. Carrigan, P. M. Chadwick, L.-M. Chounet, R. Cornils, L. Costamante, B. Degrange, H. J. Dickinson, A. Djannati-Ataï, L. O'C. Drury, G. Dubus, K. Egberts, D. Emmanoulopoulos, P. Espigat, F. Feinstein, E. Ferrero, A. Fiasson, G. Fontaine, S. Funk, S. Funk, Y. A. Gallant, B. Giebels, J. F. Glicenstein, P. Goret, C. Hadjichristidis, D. Hauser, M. Hauser, G. Heinzelmann, G. Henri, G. Hermann, J. A. Hinton, W. Hofmann, M. Holleran, D. Horns, A. Jacholkowska, O. C. de Jager, B. Khélifi, N. Komin, A. Konopelko, K. Kosack, I. J. Latham, R. Le Gallou, A. Lemière, M. Lemoine-Goumard, T. Lohse, J. M. Martin, O. Martineau-Huynh, A. Marcowith, C. Masterson, T. J. L. McComb, M. de Naurois, D. Nedbal, S. J. Nolan, A. Noutsos, K. J. Orford, J. L. Osborne, M. Ouchrif, M. Panter, G. Pelletier, S. Pita, G. Pühlhofer, M. Punch, B. C. Raubenheimer, M. Raue, S. M. Rayner, A. Reimer, O. Reimer, J. Ripken, L. Rob, L. Rolland, G. Rowell, V. Sahakian, L. Saugé, S. Schlenker, R. Schlickeiser, U. Schwanke, H. Sol, D. Spangler, F. Spanier, R. Steenkamp, C. Stegmann, G. Superina, J.-P. Tavernet, R. Terrier, C. G. Théoret, M. Tluczykont, C. van Eldik, G. Vasileiadis, C. Venter, P. Vincent, H. J. Völk, S. J. Wagner, and M. Ward. Observations of the Crab nebula with HESS. 457:899–915, October 2006.

[4] F. A. Aharonian and S. V. Bogovalov. Exploring physics of rotation powered pulsars with sub-10 GeV imaging atmospheric Cherenkov telescopes. *New Astronomy*, 8:85–103, February 2003.

[5] A. M. Atoyan, F. A. Aharonian, and H. J. Völk. Electrons and positrons in the galactic cosmic rays. *prd*, 52:3265–3275, September 1995.

[6] G. R. Blumenthal and R. J. Gould. Bremsstrahlung, Synchrotron Radiation, and Compton Scattering of High-Energy Electrons Traversing Dilute Gases. *Reviews of Modern Physics*, 42:237–271, 1970.

[7] R. A. Chevalier. Was SN 1054 A Type II Supernova? In D. N. Schramm, editor, *Supernovae*, volume 66 of *Astrophysics and Space Science Library*, pages 53–+, 1977.

[8] Luc Devroye. *Non-uniform random variate generation*. 1986.

[9] J. J. Engelmann, P. Ferrando, A. Soutoul, P. Goret, and E. Juliusson. Charge composition and energy spectra of cosmic-ray nuclei for elements from Be to NI - Results from HEAO-3-C2. *aap*, 233:96–111, July 1990.

[10] Furukawa, M. et al., 2003, Proc. 28. Int. Cosmic-Ray Conf. (Tsukuba),4,1877.

[11] B. M. Gaensler and P. O. Slane. The Evolution and Structure of Pulsar Wind Nebulae. *araa*, 44:17–47, September 2006.

[12] G. Ghisellini, P. W. Guilbert, and R. Svensson. The synchrotron boiler. *apjl*, 334:L5–L8, November 1988.

[13] V. L. Ginzburg and S. I. Syrovatskii. *The Origin of Cosmic Rays*. 1964.

[14] P. Goldreich and W. H. Julian. Pulsar Electrodynamics. *apj*, 157:869–+, August 1969.

[15] J. D. Jackson. *Classical electrodynamics*. 1975.

[16] N. S. Kardashev. Nonstationarity of Spectra of Young Sources of Nonthermal Radio Emission. *Soviet Astronomy*, 6:317–+, December 1962.

[17] T. Kobayashi, Y. Komori, K. Yoshida, and J. Nishimura. The most likely sources of high energy cosmic-ray electrons in supernova remnants, 2004.

[18] A. Lukasiak, P. Ferrando, F. B. McDonald, and W. R. Webber. The isotopic composition of cosmic-ray beryllium and its implication for the cosmic ray's age. *apj*, 423:426–431, March 1994.

[19] H. A. Mayer-Hasselwander, D. L. Bertsch, K. T. S. Brazier, J. Chiang, C. E. Fichtel, J. M. Fierro, R. C. Hartman, S. D. Hunter, G. Kanbach, P. W. Kwok, D. A. Kniffen, Y. C. Lin, J. R. Mattox, P. F. Michelson, P. L. Nolan, K. Pinkau, H. Rothermel, E. J. Schneid, M. Sommer, P. Sreekumar, D. J. Thompson, and C. von Montigny. High-energy gamma radiation from Geminga observed by EGRET. *apj*, 421:276–283, January 1994.

[20] R. Moderski, M. Sikora, P. S. Coppi, and F. Aharonian. Klein-Nishina effects in the spectra of non-thermal sources immersed in external radiation fields. *mnras*, 363:954–966, November 2005.

[21] G. B. Rybicki and A. P. Lightman. *Radiative processes in astrophysics*. 1979.

[22] Patrick Slane. Particle acceleration in supernova remnants and pulsar wind nebulae, 2002.

[23] S. I. Syrovatskii. *Soviet Astronomy*, 3:22, 1959.

Danksagung

An dieser Stelle möchte ich mich bei den vielen Menschen bedanken, die auf unterschiedliche Weise zur Entstehung dieser Diplomarbeit beigetragen haben. Mein besonderer Dank gilt:

Professor Werner Hofmann dafür, dass ich in seiner Arbeitsgruppe meine ersten wissenschaftlichen Erfahrungen an einem großartigen Thema sammeln durfte, für die lehrreichen Gespräche und die gute Betreuung.

Professor Karl-Tasso Knöpfle dafür, dass er die Zweitkorrektur übernommen hat.

Kathrin Egberts für die tolle Betreuung (der selbst eine räumliche Distanz von mehreren hundert Kilometern nichts anhaben kann), das sicherlich haarsträubende Korrekturlesen dieser Arbeit und die Fähigkeit, irgendwie immer gut gelaunt, freundlich und hilfsbereit zu sein.

Stefan Hoppe dafür, dass er mich in freundschaftlicher Atmosphäre super betreut, etwas militärischen Drill in mein Leben und meinen Schreibtisch des Öfteren aufgeräumt und gereinigt hat.

Wilfried (Klein-Nishina scattering) Domain(ko) für das Korrekturlesen, seine astrophysikalischen Weisheiten (und solche anderer Art) und die Tatsache, ihn darüber immer ausquetschen zu können, ohne dass er es mir übel nahm.

Daniil Nekrassov für die ständige Diskriminierung und das von ihm geschürte Gefühl, einfach überhaupt nichts zu können. (Liebe/r Antidiskriminierungsbeauftragte/r, das ist ein Scherz!)

Christoph Deil, Henning Gast und Andreas Hillert dafür, dass sie mir in den letzten Zügen dieser Arbeit kräftig geholfen haben.

Sabrina Casanova, Christopher van Eldik und Stefan Ohm für die hilfreichen Gespräche, Tipps und Anregungen.

Ruth Crespo dafür, dass man sich in organisatorischen Fragen immer auf sie verlassen kann.

Robert Gast, Anne Bochow, Chia-Chun Lu, Petter Hofverberg, Dirk Lennarz, Andre-Claude Clapson, Raquel de los Reyes, Ryan Chavez, Douglas Hagues

und all den anderen Mitgliedern der Heidelberger H.E.S.S. Gruppe für eine schöne Zeit und eine angenehme Arbeitsatmosphäre.

Am meisten jedoch danke ich meiner wunderbaren Familie und den Menschen die mir so nahe sind, dass ich sie schon dazu zähle (auch wenn einer von ihnen eigentlich weit entfernt auf einem anderen Kontinent ist), ohne die ich es ganz gewiss nicht bis hierher geschafft hätte, allen voran meinem Vater Reinhardt Hahn dafür, dass er immer an mich glaubt und mich auch in schweren Entscheidungen nach Kräften unterstützt und meiner Mutter Maria Feid, der ich für ihre Liebe, Herzlichkeit und Rat unendlich dankbar bin.

Erklärung:

Ich versichere, daß ich diese Arbeit selbständig verfasst und keine anderen als die angegebenen Quellen und Hilfsmittel benutzt habe.

Heidelberg, den ....
(*Unterschrift*)